

CHARACTERIZATION OF PORE STRUCTURE AND AIRFLOW DISTRIBUTION IN
BULK GRAINS

BY

CHARLES CHIOMA NWAIZU

A Thesis submitted to the Faculty of Graduate Studies of the University of Manitoba in

partial fulfillment of the requirement for the degree of

DOCTOR OF PHILOSOPHY

Department of Biosystems Engineering

University of Manitoba

Winnipeg, Manitoba

© December, 2018

Abstract

Airflow behavior in stored bulk grains is a function of the geometry and topology of pore structure within the grain bed. An image analysis technique was used to reconstruct the complex 3D pore structure within bulk grain from 2D thin section images in this study. The 3D model was developed by aligning successive 2D thin section images obtained from colored-wax solidified soybean grain beds. The model was then used for the reconstruction and visualization of airflow paths within the bulk grain. Porosity and tortuosity values were estimated from the reconstructed airflow paths and empirical models were developed for predicting porosity and tortuosity as a function of compaction pressure exerted by the grain weight and by vibration. Results indicated that the rate of decrease in porosity was higher at the lower compaction pressure and then gradually approached a minimum value as the grain depth increased. Without compaction pressure, the initial porosity of the tested soybean bed was determined to be 0.42 and later reduced to 0.34 at a compaction pressure of 14.2 *kPa* (equivalent to a grain depth of 2.2 *m*). Tortuosity increased with the compaction pressure from 1.15 at no compaction to 1.58 at a compaction pressure of 14.2 *kPa* (equivalent to 2.2 *m* of grain depth), or by 37.4%. Vibration noticeably affected the pore structure of the soybean bed. At lower vibration intensity ($< 1g$), porosity and tortuosity changed little. At higher vibration intensity of about ($2g$), porosity reduced to a minimum value of 0.34 and tortuosity increased to a maximum value of 1.39, which represented a 21% reduction in porosity and 15% increase in tortuosity, respectively. As the vibration intensity increase further ($> 2g$), excessive dynamic energy over-excited grain kernels in the grain bed, resulting in a less dense grain bed (i.e., higher porosity).

To further investigate the significance of grain compaction in designing grain aeration and drying systems, its overall effect on airflow distribution and pressure drop within stored bulk grains was simulated with CFD (computational fluid dynamics) models by the integration of the porosity and tortuosity models to account for variations in pore structure within the grain bed. The relative differences in pressure drop between simulation based on variable pore structure and experimental values reported to be below 10%, whereas the differences were around 40% when constant pore structure was used in the CFD simulations. The variable pore structure CFD model was used in case studies to predict airflow velocities and static pressure distributions in grain bins of various floor configurations, aspect ratios, directions of airflow, and duct designs.

To investigate the anisotropic characteristics of pore structures in grain beds, geometrical models were developed to simulate airflow paths in the vertical and horizontal directions and to predict pressure drops in the two directions in bulk grains. Cylindrical tubes of variable diameters were used in the models to represent flow channels in the grain bulk. These tubes were stacked progressively from small sizes to the large sizes along the grain depth to mimic the effect of compaction in the grain mass. The predicted pressure drops in the horizontal direction were 90.1%, 68.3% and 60.3% of that of the vertical direction for 1 *m*, 5 *m*, and 10 *m* grain depths, respectively. This result indicated, for the first time, that compaction might be the major factor responsible for the anisotropic resistance to airflow in bulk grains.

Acknowledgements

First of all, I would like to thank my supervisor, Dr. Qiang (Chong) Zhang for his continued guidance over the years, from start to finish of this project. I would also like to thank members of my advisory committee; Dr. Ramanathan Sri Ranjan and Dr. Oluwole Akinremi for their contribution and valuable suggestions all through the course of my study.

I wish to appreciate the Natural Science and Engineering Research Council of Canada (NSERC) and University of Manitoba for their financial support and scholarship awards all through my PhD program. Also, I sincerely thank the technical, administrative, academic staffs, and specially my Research Group Members: Daisy, Amy, Desmond, and Emily in the department of Biosystems Engineering for all their assistance and support during the course of this work.

I would like to use this medium to specially thank my father for making me to believe that I can do all things if only I believe in myself and God. And it is my mother that made me to understand that there is always a gain in being diligent at your work. I am indebted to my family, they are all my beginning and they still stick to me to this very moment – I love you guys! Thank you for your support, patience, prayer, and love.

Lastly, my utmost gratitude goes to the cause that has no cause, the unmovable mover, the King of kings – the Almighty God, without whom there wouldn't have been any progress or any life accomplishment.

Dedication

This thesis is dedicated to my mother: Mrs. Mercy Nwaizu (Obidiya) for her unflinching love for education and the roles she played in my life as a young boy nurturing me in the way of God.

Table of Contents

Abstract.....	i
Acknowledgements	iii
Dedication	iv
Table of Contents.....	v
List of Tables.....	viii
List of Figures.....	ix
1 Introduction.....	1
1.1 Background.....	1
1.2 Objectives	4
1.3 Significance.....	5
1.3.1 Improved airflow system designs for grain storage.....	5
1.3.2 A new understanding of horizontal airflow design for grain storage.....	6
2 Literature Review	8
2.1 Characterizing pore structure	8
2.1.1 Modeling pore structure	9
2.1.2 Indirect techniques for characterizing pore structures	12
2.1.3 Direct imaging techniques for characterizing pore structure	14
2.2 Critical parameters used in characterizing pore structure	17
2.2.1 Porosity.....	18
2.2.2 Pore connectivity	19
2.2.3 Tortuosity.....	19
2.3 Airflow through bulk grain in storage systems	21
2.4 Resistance to airflow through bulk grains in storage systems	23
2.4.1 Factors affecting resistance to airflow through bulk grains	25
2.4.2 Predicting resistance to airflow through bulk grains.....	29
3 Materials and Methods	37
3.1 Materials	37

3.2	Experiments	38
3.2.1	Compaction test.....	39
3.2.2	Stabilizing pore structure of test samples	44
3.3	Image analysis	45
3.3.1	Image acquisition.....	45
3.3.2	Image processing methods.....	45
3.3.3	Quantification of pore structures from 3D volume images	53
3.4	Statistical analysis.....	57
3.5	CFD simulations.....	57
3.5.1	Overview of the CFD Fluent simulations.....	57
3.5.2	CFD Fluent formulation for compaction effect due to grain pressure.....	60
3.5.3	Geometry.....	63
3.5.4	Mesh generation.....	65
3.5.5	Simulation parameters and boundary conditions.....	66
3.6	Pore-scale geometrical models based on compaction for predicting resistance to airflow	67
3.6.1	Geometrical model for predicting resistance to airflow in the horizontal direction	67
3.6.2	Geometrical model for predicting resistance to airflow in vertical direction	71
4	Results and Discussion	74
4.1	Location effect.....	74
4.2	The effect of compaction on pore structure.....	75
4.2.1	Porosity variation with compaction pressure (grain depth)	75
4.2.2	Tortuosity variation with compaction pressure (grain depth).....	80
4.3	The effect of vibration on pore structure.....	81
4.3.1	Porosity variation due to vibration.....	81
4.3.2	Tortuosity variation due to vibration.....	84
4.4	The effect of vibration on pore structure.....	86
4.4.1	Validation of the CFD simulation models	86
4.4.2	Simulating the effect of compaction on airflow.....	89
4.4.3	Simulating different grain aeration systems.....	94

4.5	Predictions of anisotropic airflow by pore scale geometrical models.....	110
5	Conclusions and Recommendations	115
5.1	Conclusions.....	115
5.1.1	Effect of compaction on pore structure in bulk grains	115
5.1.2	Effect of pore structure variation on simulating airflow through bulk grains.....	115
5.1.3	Directional dependency of resistance to airflow in bulk grains.....	116
5.2	Recommendations	117
5.2.1	Further characterization of pore structure in bulk grains.....	117
5.2.2	Analyzing entrance and wall effects	117
5.2.3	Incorporating vibration effect into flow through bulk grains	118
	Reference.....	120
	Appendix A: 3D visualization and skeletonization	134
	Appendix B: Statistics Analysis Output and Codes	147
	Appendix C: UDF Programming codes	182

List of Tables

Table 2.1 Some equations reported in the literature showing relationship between tortuosity and porosity.....	21
Table 3.1 Physical properties of Soybean grain sample.	37
Table 3.2 Physical Properties of air used in the simulations.	67
Table 4.1 Comparison between the predicted porosity with experimental and other model.	78
Table 4.2 Comparison between the predicted porosity with experimental and other model.	84
Table 4.3 Relative errors between experimental value and values predicted by the variable and constant pore structure simulations.	88
Table 4.4 Relative errors between ASABE standard and values predicted by the variable and constant pore structure simulations.	89

List of Figures

Figure 2.1	Schematic diagram showing different drying front (Nwaizu, 2013).....	23
Figure 3.1	Experiment set-up for the compaction test.	39
Figure 3.2	Experiment set-up for the vibration test.	42
Figure 3.3	Transparent cut-section windows on the wall for visualization.	42
Figure 3.4	Example of (a) extracted sample and (b) three subsamples cut from the top, middle, and bottom of the sample.....	44
Figure 3.5	Example of the (a) RGB 2D section image re-sized to (b) ROI of size 362 x22 pixels.	46
Figure 3.6	Example of RGB image with noise at the grain kernel boundaries (b) close-up view showing the blurred grain kernel boundaries (c) close-up image after noise reduction filter has been applied.	47
Figure 3.7	Example of RGB image after erosion and dilation operation.	47
Figure 3.8	Image representation of the (a) presence and (b) elimination of irregular features.	48
Figure 3.9	RGB image of the red wax-filled pores of soybean grain: (a) conjoined grain kernels after the previous image processing operations; (b) result of imageJ watershed algorithm to separate the conjoined grain (c) and (d) show close-up view of (a) and (b), respectively.....	49
Figure 3.10	RGB image of the red wax filled pores of soybean sample. (a) result of ImageJ watershed algorithm to separate pores; and (b) close-up image of a local area.....	50
Figure 3.11	Segmented image of a 2D section showing the image after binarization into pores (black) and grain (white) with the thresholded histogram based on manual setting.	51
Figure 3.12	Graphic illustration of 3D image construction. (a) 2D slice section images of 0.2 cm thickness (b) 2D slice section image with colour separated pores of 0.2 cm thickness stacked and aligned; (c) constructed 3D volume.....	53
Figure 3.13	Airflow paths (each color shades represent an individual inter-connected paths) within a 3D volume	54

Figure 3.14	Extracted 3D reconstructed of the inter-connected paths with the highest degree of connectivity.	56
Figure 3.15	Result of direct skeletonization process from (a) binary image of the inter connected flow paths with highest degree of connectivity and applied Skeleton3D to obtain (b) thin skeletonized image, which was then analyzed by analyzedSkeleton3D to formed (c) pruned thin skeletonized image from which different possible paths/branches from the thin skeleton were estimated.....	56
Figure 3.16	CFD Fluent-simulation process.	58
Figure 3.17	Three-dimensional model geometry for the flat-bottom grain storage bins with (a) cross partial perforated floor configuration (b) cross partial perforated floor configuration (c) rectangular partial perforated floor configuration.....	64
Figure 3.18	Three-dimensional model geometry for the flat-bottom grain storage bins with different aspect ratios (a) H:D = 0.75 (b) H:D = 1.00 (c) H:D = 1.50.	64
Figure 3.19	Three-dimensional model geometry for the flat-bottom grain storage bins with horizontal airflow (a) cylindrical-shaped tube inlet (b) cone-shaped tube inlet.....	65
Figure 3.20	Schematic diagram of the porous media model for airflow in the horizontal direction in a grain bed.....	68
Figure 3.21	Schematic diagram of the porous media flow path model in vertical direction.	71
Figure 4.1	Measured porosity (a) and tortuosity (b) at different grain pressures (depths) at different sample locations (Top, Middle, and Bottom).	74
Figure 4.2	Variation in porosity with grain depth.....	76
Figure 4.3	Comparison between the porosity predicted by porosity variation model based on compaction (grain depth) and experimental results.	77
Figure 4.4	Effect of compaction on pore volume.	79
Figure 4.5	Effect of compaction on pore shape (sphericity).....	79
Figure 4.6	Variation in tortuosity with grain depth.....	80

Figure 4.7	Comparison between the tortuosity predicted by the proposed model based on compaction and experimental data.	81
Figure 4.8	Variation in porosity with vibration intensity.	82
Figure 4.9	Comparison between the porosity predicted by porosity variation model based on vibration and experimental results.	83
Figure 4.10	Variation in porosity with vibration intensity.	85
Figure 4.11	Comparison between the tortuosity predicted by tortuosity variability model based on vibration and experimental results.	86
Figure 4.12	Comparison of CFD model simulations with ASABE Standard and experimental data reported in the literature.	87
Figure 4.13	Simulated pressure drop distribution within the soybean bed at air inlet velocity of 0.01 ms^{-1} (a) without compaction, (b) with compaction.	92
Figure 4.14	Simulated airflow velocity distribution for the soybeans bed at air inlet superficial velocity of 0.01 ms^{-1} (a) without compaction, (b) with compaction.	94
Figure 4.15	Simulated pressure distribution for soybean bed at air inlet superficial velocity of 0.025 ms^{-1} for circular, cross and rectangular partial perforated floor configurations.	96
Figure 4.16	Simulated airflow velocity distribution for the soybeans bed at air inlet superficial velocity of 0.025 ms^{-1} for circular, cross and rectangular partial perforated floor configurations.	97
Figure 4.17	Simulated pressure drop distribution for the soybeans bed at air inlet superficial velocity of 0.005 ms^{-1} (based on design flow rate of $0.0017 \text{ m}^3 \text{ s}^{-1} \text{ t}^{-1}$) for cylindrical bin with H:D =0.75.	99
Figure 4.18	Simulated pressure drop distribution for the soybeans bed at air inlet superficial velocity of 0.007 ms^{-1} (based on design flow rate of $0.0017 \text{ m}^3 \text{ s}^{-1} \text{ t}^{-1}$ for cylindrical bin with H:D =1.00.	99
Figure 4.19	Simulated pressure drop distribution for the soybeans bed at air inlet superficial velocity of 0.01 ms^{-1} (based on design flow rate of $0.0017 \text{ m}^3 \text{ s}^{-1} \text{ t}^{-1}$) for cylindrical bin with H:D =1.50.	100
Figure 4.20	Simulated airflow velocity distribution for the soybeans bed at air inlet superficial velocity of 0.05 ms^{-1} (based on design flow rate of $0.0017 \text{ m}^3 \text{ s}^{-1} \text{ t}^{-1}$) for cylindrical bin with H:D =0.75.	102

Figure 4.21	Simulated airflow velocity distribution for the soybeans bed at air inlet superficial velocity of 0.07 m s^{-1} (based on design flow rate of $0.0017 \text{ m}^3 \text{ s}^{-1} \text{ t}^{-1}$) for cylindrical bin with H:D =1.00.	102
Figure 4.22	Simulated airflow velocity distribution for the soybeans bed at air inlet superficial velocity of 0.01 m s^{-1} (based on design flow rate of $0.0017 \text{ m}^3 \text{ s}^{-1} \text{ t}^{-1}$) for cylindrical bin with H:D =1.50.	103
Figure 4.23	Simulated pressure pattern for variable pore structure grain bed for the horizontal airflow system.	104
Figure 4.24	Simulated air velocity pattern for variable pore structure grain bed for the horizontal airflow system.	105
Figure 4.25	Simulated results of (a) airflow velocity distribution using four inlet tubes and (b) pressure distribution using four inlet tubes (c) airflow distribution using eight inlet tubes (d) pressure distribution using eight inlet tubes.	107
Figure 4.26	Results of airflow velocity distribution of variable pore structure simulation for the horizontal airflow using cone-shaped inlet tubes.	109
Figure 4.27	Results of airflow velocity distribution of variable pore structure simulation for the horizontal airflow using cone-shaped inlet tubes.	109
Figure 4.28	Predicted pore radius (a), and predicted intrinsic permeability (b) for 10m deep bed.	110
Figure 4.29	Comparison between vertical and horizontal pressure drop for a 10 m deep grain bed.	112
Figure 4.30	Comparison between vertical and horizontal pressure drop for a 5m deep grain bed.	112
Figure 4.31	Comparison between vertical and horizontal pressure drop for a 1 m deep grain bed.	113

1 Introduction

1.1 Background

Maintaining the quality of harvested grains in storage structures requires good management. Temperature and moisture content are the most important factors that dictate the storability of grains (Navarro and Noyes, 2002). Grain deterioration is mainly due to the attack of insects, mites and fungi on stored grain (Jian et al., 2005). The accumulations of moisture in localized regions within bulk grains promote the growth and development of these organisms. Although, bulk grains may have been placed in storage at recommended safe moisture contents and temperatures, variation in ambient or internal conditions can cause temperature gradients and movement of moisture in bulk grains (Nguyen et al., 1987; Smith and Sokhansanj, 1990; Khankari et al., 1995; Montross et al., 2002; Lawrence et al., 2013). Over time, continuous movement of moisture in stored grains will lead to build up of excessive moisture, and consequently increase in temperature at localized regions known as hot spots, where deterioration occurs due to the growth and reproduction of insect, mites and fungi, making the grain quality deteriorates in storage (Khankari et al., 1995; Jian et al., 2005; Lawrence et al., 2013). To eliminate or minimize temperature and moisture variations in stored bulk grains, a common practice is to force air to flow through grain beds to dry or cool the grain by removing excess moisture (drying) or reducing the temperature (aeration) in the grain bulk. The success of this operation highly depends on the uniformity of the air flowing through the bulk grain. Uneven air flowing through a grain bed could result in non-uniformly dried products, where there may be an over dried grain in the high air flowing regions and under-dried grain in the low air flowing regions.

The locations of no air flow (stagnant) or low air flow are often the starting point for deterioration (Sinha et al. 1981). Therefore, it is imperative to understand the prevailing nature of airflow in stored grain. The common method to study airflow and airflow resistance (static pressure drop) in stored bulk grains during aeration or drying is by conducting physical experiments to measure airflow within the grain mass (Alagusundram and Jayas, 1990). The experimental method is usually time consuming, expensive and in some cases, technically difficult or impossible. Researchers have developed empirical models to approximate relationships between pressure drop and airflow based on experimental results (Shed, 1951; Shedd, 1953; Hukill and Ives, 1955; Ergun, 1952). However, results from these studies have limitations because further studies have shown that many factors, beyond what have been considered in the experiments, such as airflow rate, airflow direction, airflow conditions, grain types, grain size, bulk density, porosity, pore structure, filling methods, foreign materials, fines, bin shapes, bin size, bin floor configurations, duct configurations, all may have considerable effect on airflow velocities and resistance to airflow in bulk grains (Gayathri and Jayas, 2007; Moses et al., 2013). Mathematical modeling based on physical principles of fluid flow through porous media has the potential to incorporate the effects of these factors on airflow velocity and resistance to airflow distribution in bulk grains. However, most existing mathematical models are solved using simplified assumptions (Jayas et al., 1990; Rodriguez et al., 2011). Jayas et al. (1990) developed a model for predicting pressure drop patterns through bulk grain with an assumption that the bulk grain was homogenous. This is far from true. In large grain storage structures, the grain bulk is non-homogenous and the characteristics of the grain pore

structure vary as a function of the grain depth (Khatchaturian et al., 2016). The interstitial pore structure inside bulk grains is a complex heterogeneous space, interconnected and highly tortuous in nature. Knowledge of this complex variability of pore structure is essential for truly understanding and accurately predicting airflow in bulk grains. Assuming a simple homogeneous pore structure for bulk grains can significantly alter physical parameters involved in aeration or drying processes, such as airflow velocity and static pressure distributions (Khatchaturian and Savicki, 2004). Lai (1980) stated in his study that assuming a constant grain bed (pores) would create serious errors in predicting airflow characteristics in the packed bed.

Realistic mathematical modeling of flow through bulk grains can only be achieved when transport equations are developed to account for the structural and geometrical complexities of the pore structure. Hihinashvili and Blumenfeld (2010) concluded that establishing this pore structure-transport relationship, which they referred as one of the “holy grails” in this field of study, is the key in accurately predicting flow and macroscopic properties. Pores tend to be irregular in shape and inter-connected to form complex networks (some pores are not even connected with others) (Lukaszuk et al., 2009). Furthermore, the pore structure of a porous material changes when the material is subjected to external disturbances, such as vibration. This inherent heterogeneity and the changing in pore structures create extreme challenges in quantifying pore structure inside bulk grains (Neethirajan et al., 2008). A few studies have tried to integrate variation in pore structure characteristics into mathematical models for predicting airflow and pressure drop in bulk grains. Lai (1980) used Ergun’s equation to study three-dimensional axisymmetric airflow through grain beds and

represented variable porosity in his simulation by using two different porosities, 0.4 at the center and 0.6 at the periphery. A similar procedure was used by Garg (2005) for modeling non-uniform airflow through bulk grain, where variable porosity was represented with two different values, one for the center core volume of the grain mass and the other for the peripheral volume. One of the limitations of simulating variable porosity by using multiple constant porosities was the inability to model the continuous variation that exists in the grain mass. Lawrence and Maier (2011) and Olatunde et al. (2016) used two different porosities, one at the center and the other at the wall, and assumed that the porosity varied linearly from the center to the wall. Given that the pore structure in a grain bulk is affected by many factors, such as filling methods, grain pressure, etc., assuming linear variation of porosity may be overly simplified. Furthermore, other key pore structure characteristics, such as tortuosity, should also be considered variable in the grain bulk. But there is lack of research that quantifies these variations of pore structure in bulk grains. In general, there are two notable gaps in modeling flow through bulk grains. First, there is no direct technique or method for determining variation of pore structure parameters such as porosity and tortuosity in bulk grains. Secondly, there is lack of studies that incorporates this variation of pore structure parameters in solving flow and transport problems through bulk grains.

1.2 Objectives

The objectives of this research are:

- i. to develop pore structure models based on 3D image reconstruction of bulk grain (soybeans) to predict variation in porosity and tortuosity due to compaction caused by grain pressure and vibration

- ii. to incorporate the developed pore structure models in numerical (CFD) simulations to study airflow in grain storage bins
- iii. to develop pore-scale models to predict the anisotropic behavior of airflow resistance (pressure drop) in bulk grains.

To achieve these objectives, four segments of research were conducted. First, experiments were conducted to study the effect of compaction due to grain depth (self-weight) and vibration on pore structure characteristics (porosity, tortuosity, and connectivity). In the second segment, the data from the experiments were analyzed, based on which models were developed to predict pore structure variation in bulk grains. In the third segment, CFD simulation models were developed to integrate pore structure variation into fluid mechanics models. Lastly, geometrical models were developed to predict the direction dependency of airflow resistance in bulk grains.

1.3 Significance

1.3.1 Improved airflow system designs for grain storage

In designing forced airflow systems (aeration and drying) for grain storage, determination of airflow rate, flow uniformity, and pressure drop (resistance to airflow) are the three major design considerations. Most theories for designing forced airflow systems in grain storage, such as ASABE Standard (ASABE D272.3, 2011), have been developed with the assumption of homogeneity of bulk grains to simplify design processes. However, in reality, bulk grains are not homogeneous. This study provided a base on which the heterogeneity (non-homogeneous) of bulk grains can be incorporated into mathematical models in predicting airflow. Specifically, non-homogeneous within a grain bed as a result of compaction due to grain pressure and

vibration was experimentally studied, based on which predictive models were developed. An innovative computer imaging method was developed for studying 3D images of pore structure and inter-connected airflow paths within bulk grains.

1.3.2 A new understanding of horizontal airflow design for grain storage

Several studies have established the fact that airflow resistance through a grain bulk is lower in horizontal direction than in the vertical direction (Kumar and Muir, 1986; Jayas et al., 1987; Alagusundram et al., 1992; Hood and Thorpe, 1992; Pagano et al., 2000; Lukaszuk et al., 2008). Kumar and Muir (1986) in their experiments with wheat and barley concluded that for the airflow velocity of 0.077ms^{-1} , resistance to airflow in the vertical direction was 60% higher than the resistance in horizontal direction. Hood and Thorpe (1992) based on their experimental study of ten different types of seeds concluded that resistance to airflow in vertical direction was approximately two times higher than airflow resistance in horizontal direction for all the bulk seeds tested. Similarly, Jayas et al. (1987) reported that airflow resistance was up to 50% higher in the vertical direction than in the horizontal direction. Lukaszuk et al. (2008) stated that airflow resistance in the vertical direction in a cylindrical column filled with wheat was 1.3 to 1.95 times higher than the airflow resistance in the horizontal direction. For design purposes, ASABE Standard (ASAE D272.3, 2011) recommends that resistance in horizontal direction should be estimated as 60% to 70% of the resistance in vertical direction. This difference in resistance to airflow (pressure drop) between the horizontal and vertical directions through bulk grains has been attributed to grain kernel orientations dictated by non-spherical grain particles with their major (long) axes in the horizontal direction. However, recent studies have shown that differences in resistance

to airflow in vertical and horizontal directions also occur in spherical kernel grains (Neyo, 2006; Khatchatourian et al., 2009). This indicates that the earlier explanation based on kernels orientation cannot sufficiently explain the anisotropic behavior of resistance to airflow through grain bulks. In this study, for the first time, a new approach attributing anisotropic behavior of resistance to airflow in bulk grains to compaction effect was developed using pore-scale geometrical models.

2 Literature Review

This chapter presents literature review on three topics: Section 2.1 and Section 2.2 reviewed the methods for pore structure characterization and quantification in porous media with a particular focus on bulk grains. Section 2.3 reviewed fluid flow behaviour through porous media with particular focus on bulk grains. And lastly Section 2.4 reviewed the different approaches that have been used to model porous beds and outlined the progress that have been achieved over the past two decades in incorporating the effects of pore structure characteristics in modeling flow through bulk grains.

2.1 Characterizing pore structure

Characterization of spatial variations of pore structure is of great importance for modeling flow through porous media. It links essential geometrical and topological attributes of porous media to macroscopic transport parameters. Smith and Jayas (2004) stated that information about the interconnectivity of flow paths is needed in design of forced ventilation and in modeling heat transfer within bulk grains. Also, information about the pore space network in bulk grains will enhance predictive model for insect movement in the grain bulks (Jain et al., 2005) and aid in understanding sound transmission through bulk grains which would facilitate design of acoustic systems for detecting insect infestation in the stored grain (Hickling,1997).

Experimental and theoretical studies of airflow in grain storage systems often treat bulk grains in effect as homogeneous system and concentrate on the bulk properties of the flow. Such an approach neglects the complexities of the flow within the void of bulk grains. Although details of variable pore structure may be the most important factor

influencing the behavior of any flow process occurring within porous system. The quantity of direct interest in flow through porous media is not the properties of the matrix or the particle arrangement but rather the properties of the pores (Navarro and Noyes, 2002). To understand air flow through a porous medium such as bulk grain, we need to obtain a detailed description of the pores within the medium. There have been many significant studies about the characterization of pore structure in geological porous media, soil, and packed beds (Mueller, 1997; Boccardo et al., 2014), whereas, characterizing pore structures within the grain beds has been limited.

2.1.1 Modeling pore structure

Researchers have used different techniques to model the pore structures in porous media. Pore models that idealize the complex pore structure geometry by representing the pore structure with simple geometric shapes have been used in many studies. A simple model known as the straight tube geometry model, in which bundles of cylindrical tubes of different diameters and equal lengths are used to approximate pore structure, has become acceptable in this field of study because of its simplicity (Koponen et al. 1996; Lao et al., 2004; Du Pless and Wouldberg, 2008; Jiang, 2015). Du Pless and Wouldberg (2008) proposed a concept of representative unit cell (RUC) to simplify the pore structure within porous media. Lao et al. (2004) developed a 2D random model represented by cylindrical pipes with random generated sizes, orientation and connectivity to study non-Darcy flow in a packed bed. Yun et al. (2010) presented a three-dimensional geometry model for predicting tortuosity of streamlines in porous media with randomly placed cylindrical particles. Koponen et al. (1996) applied the Lattice Gas (LG) Cellular Automaton method to solve numerically for creeping flow of

Newtonian incompressible fluid in a two-dimensional porous substance constructed by randomly stacked squares. Jiang (2015) developed a model that assumed that bulk rock is composed of an impermeable matrix with embedded pore conduits composed of cylindrical tube elements to form a 3D network. The model was used to examine the role of connectivity in porous rock during adsorption or desorption processes. However, these simple models did not adequately describe the heterogeneity of porous media and the interconnectivity among the pores. Other models, like the pore-network model have been developed using symmetric regular two or three-dimensional network to represent the pore structure (Kammath et al., 1998; Lao et al., 2004; Jian et al., 2005; Sobieski et al., 2012; Yue and Zhang, 2017). Kammath et al. (1998) used pore network model to explain the pore structure of rocks. Jian et al. (2005) applied pore network model to grain bulk to predict the distribution of temperature, moisture and pressure during grain drying. Yue and Zhang (2017) used the pore-network model to simplify structures of bulk grain, based on which the resistance to airflow was predicted from quantified airflow paths. Although, large domain of pore space can be achieved with the use of pore network models, however, pore bodies and throats are usually represented by simplified shapes such as spheres or tubes which would not give detailed account of the real pore structure. Using physical representation of the pore space in constructing pore network by mapping the true pore space of the medium onto the network could retain the true pore morphology and the inherent spatial connectivity of the pores. This method involves direct imaging of the pore space based on which a pore network can be constructed using tessellation (An arrangement a repeated pattern without gaps or overlapping using lines or shapes).

Separating pore structure using different number of schemes such as Dirichlet (Nolan et al. 1995), Octahedral (Chan and Ng, 1988), tetrahedral (Baldwin et al., 1996), quadrons (Hihinashvili and Blumenfeld, 2010), Delaunay (Karsten, 2002) or voronoi (Du and Gunzburger, 2002) has been carried out to develop pore network models. However, tessellation of pore structure will give some statistical description of pores and intergranular paths, but will not permit a complete analysis based on geometry of the individual pores. In some cases, tessellations can lead to incorrect identification of pore locations (Baldwin et al. 1996; Liang et al. 2000; Sederman et al. 2001). Recently, the discrete element method (DEM) has been used in predicting pore structure of porous media based on which different pore structure parameters can be quantified (Gonzalez-Montellano et al., 2011; Sobieski et al., 2012; Sobieski et al. 2016; Yue and Zhang, 2017). Gonzalez-Montellano et al. (2011) used 3D discrete element models to simulate the pore structure of glass beads and maize. In their research, the glass beads were simulated as spheres in a size distribution determined by a given mean diameter and standard deviation, and the maize kernels were simulated as comprising of six spheres representing the irregular shape of the real grains. Sobieski et al. (2012) used DEM to simulate the pore structure of porous beds and developed a numerical algorithm to construct flow paths within the simulated porous media. Sobieski et al. (2016) developed a new approach for obtaining the geometric properties such as tortuosity for a granular porous bed based on DEM simulations. To a large extent the success of using DEM depends on the numbers of particles generated to represent the porous bed. Typical porous beds contain billions of particles, and DEM simulations will require long

processing time and will be computationally demanding to be able to simulate such large number of particles.

2.1.2 Indirect techniques for characterizing pore structures

Mercury intrusion porosimetry is an indirect experimental technique to characterize pore structures. Mercury intrusion porosimetry is based on the principle that mercury as a non-wetting liquid enters pore spaces when its pressure is greater than the capillary pressure. Most of the porous media comprise of different sized pores, causing the flow of mercury from the larger pores into the smaller pores. And all the pore sizes occupied by mercury are related to the applied pressure and can be quantified by the equation 2.1 (Anotvitz and Cole, 2015):

$$P = \frac{2\sigma \cos\theta}{r} \quad (2.1)$$

where P = pressure(MPa), σ = interfacial tension, r = pore radius (mm), θ = contact angle.

The pore volume is related to the amount of the mercury that invades the pore space. The higher the invading mercury, the larger is the volume of the pores. Pore surface area can be determined from the relationship between the work done on the pore surface and the work done on the mercury by the applied pressure. The average pore radius used in determining pore size distribution can be estimated by the ratio of the determined pore volume and specific surface area. However, in extracting the pore size distribution during mercury intrusion, all pores within the porous medium are represented by bundle of cylindrical tubes, so it is assumed that pores are equally accessible to the exterior mercury reservoir. This is not the case in reality because pores are generally of different sizes, shapes and complex connectivity (Hu and Piet,

2003; Xiong et al., 2016). Mercury intrusion porosimetry is a fast and versatile method. It can be used with almost any type of porous media with pores in the range of 500 μm down to 3 nm (Dullian, 1991; Xiong et al. 2016).

The sorption isotherm can be used in quantifying smaller pores by increasing the pressure absorption of nitrogen or carbon dioxide flowing through the porous media sample at constant temperature and measuring the corresponding desorption amount from the pores (Florence et al., 2008). Pore size can be quantified by using the following equation:

$$\ln \frac{P}{P_0} = \frac{-2V_m \sigma \cos \theta}{rRT} \quad (2.2)$$

where: P_0 =saturated vapour pressure(MPa), P =vapour pressure of the liquid(MPa), σ =interfacial tension, V_m =molar volume, θ =contact angle, T =absolute temp (K), R = gas constant(J/mol.K), r =pore radius(mm).

It should be noted that water is rarely used as the adsorbate liquid for measuring pore characteristics in bulk grains. The results from using water is likely to be invalid, because during water desorption, particles re-arrangement may take place and the calculated pore size distribution may not represent the actual pore size distribution at all moisture contents (Florence et al., 2008). Sorption isotherm is a well-established technique for measuring pore size characteristics such as pore radius, pore surface area, pore volume and so on (Bear, 2007). However, sorption isotherm can only be used in quantifying pores at a narrow range and it is not as popular or fast as the mercury instruction porosimetry.

The pore size obtained from mercury intrusion porosimetry and sorption isotherm methods are not accurate due to geometric and other assumption that porous media

contain pores whose shapes are cylindrical (Bear, 1972). In order to improve the accuracy of mercury intrusion porosimetry or sorption isotherm, Dullian (1991) explained how these methods could be combined with the optical method in measuring pore size distribution in clay soil. To adequately characterize pore structure, knowledge of the shape, connectivity and orientation of the pores is equally important as the size measurements. It is impossible to obtain this information from mercury intrusion porosimetry or sorption isotherm. However, recent development in direct imaging techniques provides a new way that allows visualization of the pores as well as direct measurement of the pore characteristics within the porous bed.

2.1.3 Direct imaging techniques for characterizing pore structure

Imaging techniques can produce 3D images of the internal structure of porous media. It can be used to characterize pore structure by quantifying the porosity, as well as other parameters of the pores, such as shape, size, connectivity and orientation. Also, it has the advantage that measurement and characterization of the pore structure can be combined with visual appreciation of the pores (Pagliai et al., 2012; Nwaizu and Zhang, 2015). Nwaizu and Zhang (2015) developed a smoke visualization coupled with image processing technique to provide a useful tool in characterizing airflow path tortuosity in bulk grains at a microscopic (pore) level. The use of image analysis allows getting accurate structural pore parameters, statistics, and distributions from the image (Montillet and Coq, 2001). There are several imaging techniques that have been used to characterize pore structure in diverse porous media. Some are non-intrusive techniques such as focus-ion beams and scanning electron microscopy (SEM) (Fredrich et al., 2006; Doktor et al., 2010), nuclear magnetic resonance (Sederman et al., 2001), X-ray

micro CT techniques (Neethirajan et al., 2008; Peng et al., 2012; Yang et al., 2013). The SEM method involves scanning porous media with a beam of electrons that interact with the atoms in the porous sample, producing various signals that can be detected and contain information about the sample surface topology. It is a useful technique for obtaining 2D images of the pore space but does not provide 3D spatial images, which is important to observe the pore volume and quantify interconnected regions. In recent years, the advancement in SEM technology has led to the development of focused-ion beam electron microscopy (FIB-SEM) with higher magnification and transmission which makes it possible to observe and characterize small pores (Yan et al., 2015; Aslannejad et al. 2017). Aslannejad et al. (2017) developed a visualization method of extracting the 3D structure of the porous structure of a coating layer by using FIB-SEM imaging based on which they predicted the hydraulic properties using a pore-scale computational method. Although, SEM has a lot of potential for imaging porous media, it exposes only small area for observation and cannot provide sufficient sampling area to characterize large heterogeneous extent in porous media. Nuclear magnetic resonance imaging (NMRI) is another non-intrusive technique for investigating and quantifying pore structure. Its principle is based on the nuclei of porous media placed in a magnetic field absorbing and re-emitting electromagnetic radiation. So when a porous medium is scanned with MRI, the spatial distribution of pores can be obtained (Blumich et al. 2009; Teng et al., 2017; Klemens et al., 2018). Teng et al. (2017) conducted a visualization experiment with MRI to observe the density-driven convection process and the fingers growing of CO₂ injection in porous aquifers. Klemens et al. (2018) applied MRI for accurate characterization of fluid flow and identification of the flow domain. MRI is a

very expensive and time consuming method compared to computed tomography (CT). The computed tomography imaging technique is one of the non-intrusive imaging techniques which have the capability to generate 3D image of porous media. That is, CT can be used to characterize both the open and the closed pores inside the porous media. Schoeman (2017) carried out a detailed review that demonstrated the ability of CT as a non-destructive and non-invasive technique for investigating the 3D microstructure of different range of food products and grains. Neethirajan et al. (2008) used CT to reconstruct the 3D internal structure of bulk grains and applied image analysis techniques to quantify the pore throat, pore volume, specific surface area and tortuosity of the pores. The CT technique has some obvious limitations. Poor resolution is one of its main limitations. High spatial resolution will limit the sampling area and will not produce a good representative of large-scale changes in heterogeneity of the pore structure. Conversely, low spatial resolution X-ray CT imaging will increase the sampling area but might over-estimate the pore sizes inside the bulk grains (Peng et al., 2012). It is important to note that the CT imaging technique may obscure significant features of the pores or misinterpret attenuation values resulting in complicated quantitative image analysis (Xiong et al., 2016). In addition, there may be errors and distortions in the result obtained during 3D reconstruction of the porous media (Xiong et al., 2016). Enhancement in CT imaging with either Conventional or Synchrotron Radiation, Dual Energy Scans, Focus Ion Nano tomography, have been used to improve the accuracy of CT imaging in recent years. However, these techniques are rarely applied in standard scanning procedures (Xiong et al., 2016).

The thin section imaging technique (TSI) is a notable example of an intrusive imaging technique and has been mostly used to study soil and rock porous structures (Nimmo et al., 2004; Liang et al., 1998; Bodla et al., 2014). This method involves impregnating porous media with a resin mixed with ethyl alcohol or wax to solidify the structure of the porous media and then cut into 2D sections before obtaining digital images which can then be reconstructed into 3D images. Lukaszuk et al. (2008) used epoxy resin to solidify the pore structure characteristics of rye grains in vertical and horizontal directions to be able to differentiate between the pore size and shape along the two different directions. Several imaging techniques have been developed for 3D reconstruction based on 2D cut sections (Bodla et al., 2014; Izadi et al., 2017). Bodla et al. (2014) developed 3D microstructure reconstruction procedure from 2D thin cut sections of porous media using stochastic techniques. Izadi et al. (2017) proposed a fast and reliable method to reconstruct 3D porous media based on 2D cut sections. The reconstruction of 3D was carried out using approximated full set of two-point correlation functions of 2D cut sections and a modified phase recovery algorithm. One of the major disadvantages of thin section imaging is the preparation of the thin sections, which can be elaborate and time consuming to obtain.

2.2 Critical parameters used in characterizing pore structure

Pore shape, pore-throat size, pore surface area, pore volume, pore coordination number, air-path thickness, tortuosity, connectivity of pores, porosity are some of the parameters or attributes used in characterizing pore structure (Bear, 1972). Paglial et al. (1998) stated that porosity, pore connectivity and their distributions within a porous bed are the most important parameters that dictate flow processes in porous media. Yang et

al. (2014) stated that porosity; pore distributions (size, shape and tortuosity) and pore connectivity are three of the most important characteristics used in developing mathematical models to achieve basic relationships between pore structure and transport processes.

2.2.1 Porosity

Porosity is one of the most important characteristics of pore structure that dictate fluid transport in bulk grains. It is defined as the ratio of void space to solid volume within porous media and can be quantified using equation (2.3) to be as low as 0 or asymptotically approach 1 depending on the bulk density and the nature of particles that make up the porous bed.

$$\varepsilon_t = 100 \left(1 - \frac{\rho_b}{\rho_{pt}} \right) \quad (2.3)$$

where ε_t = total porosity (%), ρ_b = bulk density ($kg\ m^{-3}$), ρ_{pt} = particle density ($kg\ m^{-3}$)

Porosity had great effect on the properties of bulk grains, and any variation in porosity will definitely lead to variations in flow through bulk grains (Rezanezhad et al., 2009). Therefore, characterizing porosity is important for studying flow through bulk grains (Lukaszuk et al., 2008). An increase in porosity increases flow hydraulic conductivity through porous media, while reduction in porosity will reduce flow hydraulic conductivity (Richard et al., 2001). Compaction due to grain self-weight (with grain depth) or vibration can change the grain kernel orientation and consequently reduction in porosity (Hao et al., 1994; Ge et al., 2000; Nwaizu and Zhang, 2015). Studies have also shown that moisture content of grain had a significant effect on porosity. Nimkar and Chattopadhyay (2002) concluded that the porosity of bulk grains increased with

increase in moisture content. Specifically, they reported that when the moisture content changed from 8.36% to 16.65%, the porosity increased from 42.15% to 43.64%. Similar result was obtained by Karababa (2006). Molenda et al. (2005) in their experimental study using white winter wheat, red winter wheat, corn and soybeans at three different moisture levels concluded that porosity was higher at higher moisture content for white wheat, red wheat, and corn but lower at higher moisture content for soybeans.

2.2.2 Pore connectivity

Connectivity of pore space is another important topological property of the pore structure that governs flow through porous media (Vogel and Kretzschmar, 1996). Pore connectivity is defined as the measurement of the total interconnected pores within a porous medium. Only the interconnected pores form the flow paths for fluid to flow through porous media (Koponen et al. 1996). In a 3D image characterization of pore structure, connectivity can be quantified by Euler number (Vogel and Kretzschmar, 1996; Neethirajan et al., 1998), fragmentation index (Neethirajan et al. 1998; Nwaizu and Zhang, 2015), and in some cases by coordination number (Xiong et al., 2016; Yue and Zhang, 2017). Another parameter is the connectivity degree which is defined as the volume fraction of the pores that are connected to both top and bottom surface to the total pore volume (Yang et al., 2014).

2.2.3 Tortuosity

Tortuosity describes the crookedness of connected pathways for fluid flow in porous media. It is often defined as the ratio of the actual microscopic (tortuous) path length (effective path length) to the nominal length of flow path (the depth of porous medium) (Hilmi, 2000; Arthur et al., 2011; Maciej and Zbigniew, 2012; Nwaizu and Zhang, 2015):

$$\tau = \frac{L_e}{L} > 1 \quad (2.4)$$

where τ = tortuosity, L_e = effective path length (m), L = nominal length parallel to the direction of bulk flow (m).

Another definition of tortuosity is the ratio of the nominal path length to the effective path length in which tortuosity is always $\tau < 1$.

$$\tau = \frac{L}{L_e} < 1 \quad (2.5)$$

While the length parallel to the bulk flow can be easily measured and unambiguously specified, the actual (effective) path length is not. Because in real porous media, actual flow paths are extremely complicated due to continuous changes in cross-section, shape and orientation of flow channels, making it difficult to identify a single path length of flow in the porous media (Maciej and Zbigniew, 2012). Several empirical and theoretical approaches have been used for the determination of tortuosity (Comiti and Renaud, 1989; Koponen et al., 1996; Yu et al. 2006). Comiti and Renaud (1989) developed an empirical equation for tortuosity through an experiment based on parallelepiped particles. Yu et al. (2006) developed a geometric model based on square particles arranged in triangles without overlapping and the other with unrestrictedly overlapped to predict tortuosity value. Yue and Zhang (2016) and Sobieski (2016) determined geometric tortuosity for idealized porous beds simulated with the discrete element models. Researchers have attempted to link tortuosity to porosity (Yu et al., 2006; Sobieski et al., 2017). Table 2.1 shows some relationships between porosity and tortuosity that have been developed over time. There is a general agreement that higher porosity will result in lower tortuosity value.

Table 2.1 Some equations reported in the literature showing relationship between tortuosity and porosity.

Model	Ajustable parameters	References
$\tau = 1 + P \ln\left(\frac{1}{\varepsilon}\right)$	P=0.63	Comiti and Renaud (1989)
$\tau^2 = \varepsilon + B(1 - \varepsilon)$	B=0.9	Iversen and Jorgense (1993)
$\tau^2 = 1 - C \ln \varepsilon$	C =2	Boudreau (1996)
$\tau = 1 + a \frac{(1 - \varepsilon)}{(\varepsilon - \varepsilon_c)^m}$	a=0.65 and m=0.15	Koponen et al. (1996)

2.3 Airflow through bulk grain in storage systems

Moisture migration or localized increase in moisture in stored grain occurs due to natural convection or uneven drying within the grain mass (Navarro et al., 2012). Moisture migration is one of the main causes of grain deterioration (Montross et al., 2002). Even with uniform moisture distribution in a bin, moisture migration can be greatly elevated by temperature differences in stored bulk grains (Navarro and Noyes, 2002). Forcing air through stored bulk grains can be used to reduce or eliminate moisture movement and temperature gradients in stored gain bulks.

Forcing air through grain bulks can be described using different terms based on the condition of operations and the intended application of the processes, including aeration, chilled aeration, natural air drying, low temperature air drying, high temperature air drying, and dryeration (Navarro and Noyes, 2002; Jayas, 2015). Aeration and drying are two commonly used operations. Aeration is often used as effective non-chemical process for the preservation of stored grains. Aeration involves moving air at a relatively low flow rate (1 to $2 \text{ m}^3 \text{ s}^{-1} \text{ m}^{-2}$) through the bulk grain to cool

the grain to slow down the rate of deterioration or to bring the grain mass to a uniform temperature to prevent moisture migration within the grain bed. Aeration has also been used for removing fumigant residue and odour in stored bulk grains (Navarro and Noyes, 2002). Typically, aeration process involves the use of a fan to move air through perforations or ducts at the bottom of the grain storage system into the stored grain to change the grain condition (Jayas, 2015).

Drying involves the use of relatively high airflow rate (10 to $25 \text{ m}^3\text{s}^{-1}\text{m}^{-2}$) to remove moisture from the grain bed thereby bringing down the grain moisture to a safe storage level (Navarro and Noyes, 2002; Gayathri and Jayas, 2007). Grain drying involves moving the ambient air or heated air through a perforated or ducted floor into the grain bed (Jayas and White, 2003). Near-ambient air and hot air drying processes are most commonly used for drying grains because of their simplicity and low energy consumption (Jayas and White, 2003). Airflow through bulk grains during drying causes the formation of three zones, with different moisture contents and temperatures. These zones are separated by a temperature front and a moisture front (fig. 2.1) (Navarro and Noyes, 2002). Zones A and B are separated by a moisture front, while the temperature front separates Zones B and C. These fronts or zones move through the bed of grains in the same direction as airflow. From figure 2.1 the grain in zone B is at the dwell state, the state that will eventually prevail throughout grain bed. Zone A exists at the bottom of the bin where the temperature and moisture content are in equilibrium with temperature and relative humidity of the air coming into the bin, while grain in zone C is yet to be affected. As the drying proceeds, zone C reduces in size and will eventually disappear when the temperature and moisture fronts have passed through the grain bed.

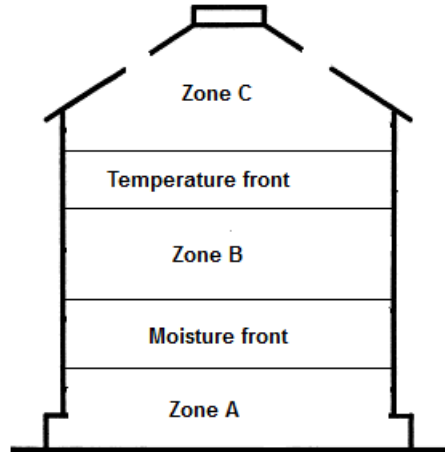


Figure 2.1 Schematic diagram showing different drying front (Nwaizu, 2013).

The design airflow rate is the volume of air required to maintain uniform airflow distribution in stored grain system during aeration or drying (Neyos and Navarro, 2002). Typically, airflow rate ranges from 0.03 to $2 \text{ m}^3\text{s}^{-1}\text{m}^{-2}$ for use in grain storage depending on the goal to be achieved (drying or aeration). Although, higher airflow rates above $2 \text{ m}^3\text{s}^{-1}\text{m}^{-2}$ will greatly increase grain cooling, but it can create other problems such as dust blowing within the storage systems which consequently can block air ducts and can be economically expensive to implement. On the other hand, low airflow rates usually result in minimum energy consumption but may not be sufficiently high to dry the grain before spoilage occurs (Fraser and Muir, 1980). Selecting appropriate airflow rate is important in designing an efficient and effective system for grain storage.

2.4 Resistance to airflow through bulk grains in storage systems

Besides the flow rate, another key factor that should be considered in designing grain aeration or drying systems is pressure drop through the grain bulk. Based on the determined air flow rate and pressure drop, an adequate fan(s) can be selected to deliver air through the grain bulk. Oversized fans lead to unnecessary energy

consumption and consequently increase in operation cost. On the other hand, under-sized fans lead to grain spoilage (Jayas, 2012). For typical fans, the airflow rate decreases as the static pressure increases. Thus, a fan sized for shorter depth may not dry or cool grain within the expected time if grain depth is increased. Similarly, a fan sized to provide a certain airflow rate, say for wheat, may not provide the same airflow rate for canola because pressure drop per unit length of canola is 2 to 2.5 times more than that for wheat (ASABE R2011.D272.3, 1996). Therefore, a good knowledge of static pressure (drop) is the key to properly size the fans (Alagusundram and Jayas, 1990; Moses et al., 2013). Pressure drop in grain aeration or drying systems is the measure of the total frictional resistance against the flow of air through duct, perforated floor and bulk grain (Navarro et al., 2012). However, studies have shown that larger part of resistance to the airflow (pressure drop) occur within the grain mass (Khatchatourian and Savicki, 2004). Movement of air through bulk grains causes energy losses due to friction and turbulence, and these energy losses are expressed as the resistance to airflow, or pressure drop (Rajabipour et al., 2001; Jekayinfa, 2006; Lukaszuk et al., 2008; Shahbazi, 2011; Kenghe et al., 2012). Due to the heterogeneous characteristics of bulk grains, airflow resistance is not uniform in a grain bulk (Navarro and Noyes, 2002). Understanding airflow resistance (pressure drop) as well as ensuring uniform distribution of airflow inside the bulk grains is essential in the design of aeration or drying systems (Molenda et al. 2005; Lukaszuk et al. 2008; Neethirajan et al. 2010; Moses et al. 2013). A uniform distribution of airflow inside bulk grains may substantially reduce the cost of operations (Bartosik and Maier, 2006). Furthermore, knowledge of airflow resistance is also important in fumigation processes for insect control (Smith and

Jayas, 2001). Many studies have been carried out to determine airflow resistance of various bulk grains. Alagusundram and Jayas (1990), Gayathri et al. (2007) and Jeyan et al. (2013) have reviewed the findings in detail. Studies have shown that airflow resistance in bulk grains are significantly affected by many factors (some important ones are discussed in Section 2.4.1), including bulk density, porosity, moisture content, filling methods, shape and size of grain, void configuration, presence of foreign materials, airflow direction, bed depth, airflow rate, duct configuration, bin shape, bin size, and bin floor configuration (Rajabipour et al., 2001; Jekayinfa, 2006; Lukaszuk et al., 2008; Shahbazi, 2011; Kenghe et al., 2012). Empirical equations such as Shedd's equation (Shedd, 1953) recommended in the ASABE Standard for determining pressure drop of air through grains at different airflow rates are often used to obtain a conservative estimate of the pressure drop through the stored grain.

2.4.1 Factors affecting resistance to airflow through bulk grains

2.4.1.1 Airflow rate

Researchers have shown that an increase in airflow rate result in higher resistance (Kashaninejad et al., 2010; Kenghe et al., 2012). Kenghe et al. (2013) showed that the airflow resistance increased as the airflow rate increased for soybeans. Rajabipour et al. (2001) observed that an increase in airflow rate from 0.12 to 0.25 m s^{-1} , the airflow resistance increased 3.35 times, and with an increase to 0.51 m s^{-1} in flow rate, the resistance increased 12 times. Shahbazi (2011) reported that the pressure drop per unit length (airflow resistance) of chickpea seeds increased with increasing airflow rate in the range of 0.02 to $0.50\text{ m}^3\text{ s}^{-1}\text{ m}^{-2}$. He explained the increase in the airflow resistance

as a result of increase in kinetic energy dissipation of the air when the velocity increased.

2.4.1.2 Bulk density

The effect of bulk density on airflow resistance can be understood in relation to the bed porosity. Decrease in bulk density leads to increase in porosity of bulk grains (Nimkar and Chattopadhyay, 2002; Kashaninejad et al., 2010; Kenghe et al., 2013). Shahbazi, (2011) stated that decrease in bulk density of chickpea seeds increased its percentage of void, and consequently, resulted in reduction of resistance to airflow. Kenghe et al. (2013) showed in their study that increase in bulk density at any moisture level resulted in an increase in resistance to airflow at all the airflow rates tested. Lukaszuk et al. (2008) observed that consolidation of bulk grain samples by vibration resulted in about 2.2 times increase in airflow resistance compared to the test samples that was not vibrated after filling.

2.4.1.3 Filling methods

Kashaninejad et al. (2010) measured the resistance to airflow through a column of pistachio nuts and showed that for the dense fill, pistachio nuts produced higher resistance to airflow compared with the loose fill. The dense fill increased the bulk density by about 23.3% and the resistance of bulk pistachio nuts to airflow by 26% compared with loose fill. Kumar and Muir (1986) in their study to test the effect of filling methods on resistance to airflow of wheat and barley, observed that at air flow velocity of 0.077 ms^{-1} , the resistance to airflow for layer filling (filling a bin with spreader) was higher than end-filling (filling a bin with stationary spout) by 25% to 35% for vertical

airflow and 50% to 75% for horizontal airflow. They explained that the higher resistance to airflow for the layer filling was due to the higher bulk density. Jayas et al. (1987) explained that the higher resistance to airflow for dense fill when compared to loose fill was because the filling methods have an extreme effect on bulk density as well as the porosity. A dense fill method reduces the porosity, resulting in higher resistance to airflow through the bulk grains.

2.4.1.4 Moisture content

Studies have shown that increase in grain moisture leads to increases in airflow resistance (Pagano et al., 2000; Nimkar and Chattopadhyay, 2002; Shahbazi, 2011; Kenghe et al., 2012; Kenghe et al., 2013). Shedd (1953) tested the effect of moisture content on the airflow resistance for several grains at a given airflow rate and observed that the airflow resistance decreased as the moisture content increased for all the grains tested. Similar conclusions were made by several other researchers (Pagano et al., 2000; Nimkar and Chattopadhyay, 2002; Shahbazi, 2011; Kenghe et al., 2012; Kenghe et al., 2013). However, Kenghe et al. (2013) reported that with increase in moisture content, the resistance to airflow decreased from 2853 to 2721 $Pa.m^{-1}$ for soybeans.

2.4.1.5 Airflow direction

Resistance to airflow in the vertical direction is generally different from that in the horizontal direction (Lai, 1980; Kumar and Muir 1986; Jayas et al., 1987; Neethirajan et al., 2008). Lamond and Smith (1982) observed in their experiment that grain kernels lied with their major (long) axes horizontally, and this would likely lead to differences in interconnectivity between pores in the vertical and horizontal directions. Several other

investigations into this effect of airflow directions on resistance to airflow showed that airflow resistance was higher in the vertical direction than that in the horizontal direction (Kumar and Muir, 1986; Lukaszuk et al., 2008). Pagano et al., (2000) observed that the resistance to airflow for oats with moisture content of 10.1% in the vertical direction was 7% to 14% higher than that in the horizontal direction. Neethirajan et al. (2008) used X – ray CT to scan the internal structure of different bulk grains, and observed higher number of air paths along the horizontal airflow direction than the vertical direction. They concluded that the directional difference in airflow resistance may be as a result of the difference in the number of connected air paths between the horizontal and the vertical directions. Also, ASABE Standard D272.3 (ASABE, 2011) recommends the use of airflow resistance in the horizontal direction to be 60% to 70% of that in the vertical direction for non-spherical shaped seeds for design purposes (wheat, barley, flaxseeds, and so on). The difference in resistance to airflow (pressure drop) in horizontal and vertical directions through bulk grains has been attributed to grain kernel orientations which was developed due to non-spherical grain particles lying horizontally with their major axes and thereby creating airflow with different characteristics on different directions (Kumar and Muir, 1986; Jayas et al., 1987; Jayas and Muir, 1991; Jaya and Mann, 1994; Molenda et al., 2005; Neethirajan et al., 2008; Lukaszuk et al., 2009). However, recent studies have shown that differences in resistance to airflow in vertical and horizontal directions also occur in spherical grains (Neyo, 2006). Neyos (2006) conducted an experiment to compare vertical to horizontal airflow resistances in a grain silo ($8m \times 20 m$) filled with soybean. His results showed that resistance to airflow in the vertical direction was 46% and 67% greater than the resistance to airflow in horizontal

direction for airflow rates of 0.08 and 0.16 $m^3s^{-1}m^{-2}$ respectively. This indicate that the earlier explanation based on kernels orientation cannot sufficiently be used to explain the anisotropic behavior of resistance to airflow through spherical grains. There must be a further explanation or reason why anisotropic behaviour of resistance to airflow occurs in bulk grains.

2.4.2 Predicting resistance to airflow through bulk grains

Modeling fluid flow in porous media is generally based on the continuity equation, the momentum equation and laws governing the dynamics of fluid flow (Oyinkepreye et al., 2012). Characterizing the geometry of pore structure, irregularity of pore walls and the complex interconnected between pores is a major challenge in applying theoretical flow models.

2.4.2.1 Classic models for predicting resistance to airflow through bulk grains

A French scientist, Henry Darcy in 1856 in his work on the investigation of hydrological systems for water supply, performed steady-state unidirectional flow experiments for a uniform sand column. From his experimental observations, he proposed Darcy's law (Darcy, 1857) as follows:

$$\frac{dP}{dL} = \frac{k}{\mu} v \quad (2.6)$$

where: dP = pressure drop (Pa), dL =depth of the porous bed (test column)(m), v = airflow rate per unit area ($m^{-3}s m^{-2}$), k = permeability (m^2) and μ = viscosity (Pa.s)

Although Darcy's law correctly describes flow in porous media; it is however limited to slow, viscous flow. As velocity becomes larger discrepancy occurs between experimental data and result obtained for Darcy Law.

An Austrian scientist Phillip Forchheimer in 1901 further investigated fluid flow through porous media in the high velocity regime. During his study, he observed that as the flow velocity increased, the inertial effects started dominating the flow. In order to account for the inertial effect, he suggested the inclusion of an inertial term representing the kinetic energy of the fluid in the Darcy equation. This is known as the Forchheimer equation (Forchheimer, 1901):

$$\frac{dP}{dL} = \frac{k}{\mu} v + \beta \rho v^2 \quad (2.7)$$

where: dP = pressure drop (Pa), dL = depth of the grain bed in the test column (m), v = airflow rate per unit area ($m^{-3}s m^{-2}$), k = constants, μ = viscosity of the flow fluid(Pa.s), β = Forchheimer coefficient (m^{-1}) and ρ = bulk density of the bed material ($kg^{-1}m^3$).

Ergun and Orning in 1949 investigated fluid flow through packed columns and fluidized beds. Based on their work, Ergun in 1952 proposed an expression for the Forchheimer coefficient as follows:

$$\beta = \frac{C_E}{k} \quad (2.8)$$

where C_E is called Ergun constant and it accounts for inertial (kinetic) effects; k is the Intrinsic permeability,

And he went on further to develop an equation for resistance to airflow (pressure drop) that incorporated the effect of the irregular shaped or non-spherical particles and porosity of the packed bed on fluid flow, known as Ergun's equation (Ergun, 1952):

$$\frac{\Delta P}{L} = A_3 V + B_3 V^2 \quad (2.9)$$

where: ΔP = pressure drop (Pa), L = length of porous bed in the test box (m), V = airflow rate per unit area ($m^{-3}s m^{-2}$), A_3 and B_3 = viscous and the inertial terms of the equation, respectively. The viscous and the inertial terms (A_3 and B_3) are defined as functions of porous bed parameters as follows:

$$A_3 = 150 \frac{(1 - \varepsilon)^2}{\varepsilon^3} \mu \frac{1}{d^2 g} \quad (2.10)$$

$$B_3 = 1.75 \frac{(1 - \varepsilon)^2 \rho}{\varepsilon^3 d g} \quad (2.11)$$

where: ε = fractional porosity, d = equivalent diameter of the bed (m), μ = viscosity of the flow fluid (Pa.s), ρ = bulk density of the bed material ($kg^{-1}m^3$), g = acceleration due to gravity (ms^{-2}).

2.4.2.2 Empirical models for predicting resistance to airflow through bulk grains

Many empirical models have been developed for predicting resistance to airflow for grains (Shedd, 1953; Huskill and Ives 1955, Brooker et al., 1974; Hague et al., 1978; Jayas et al. 1987; Boccoardo et al., 2014). These models are mostly based on experimental observations. Typically, determination of resistance to airflow through bulk grains involves the measurement of pressure drops along the bed of grain at different flow rates, and then fitting the experimental data to an empirical or semi empirical

equations for estimating the airflow resistance (Gayathri and Jayas; 2007; Moses et al. 2013; Gornicki and Kaleta, 2015).

A commonly used equation for resistance to airflow through bulk grains was developed by Shedd in 1953. Shedd (1953) measured the pressure drops in different beds of grain at various airflow rates and proposed the following equation (2.12) for estimating airflow resistance:

$$\frac{\Delta P}{L} = A_1 V^{B_1} \quad (2.12)$$

where: ΔP = pressure drop (Pa), L = depth of the grain bed in the test column (m) ,
 V = airflow rate per unit area ($m^{-3} s m^{-2}$), A_1 and B_1 = constants (dependent on the type of grain).

One of the limitations of the Shedd's model is that it can only be used to predict airflow resistance over a narrow range of airflow rate (0.00056 to $0.203 m^{-3} s m^{-2}$) (Navarro and Noyes, 2002).

Hukill and Ives (1955) proposed another model for a wider range of airflow rate (0.01 to $0.20 m^{-3} s m^{-2}$) based on the same data used by Shedd.

$$\frac{\Delta P}{L} = \frac{A_2 V^2}{\ln(1 + B_2 V)} \quad (2.13)$$

where: ΔP = pressure drop (Pa), L = length of the grain bed in the test column (m) ,
 V = airflow rate per unit area ($m^{-3} s m^{-2}$), A_2 and B_2 = constants (dependent on the type of grain).

Although, the model by Hukills and Ives (1955) have been widely used for predicting the relationship between the pressure drop and airflow rates for bulk grains (Jekayinfa, 2006), it did not include the effect of important bed properties, such as porosity, in the equation, unlike the Ergun's equation (2.8).

2.4.2.3 Numerical models for predicting resistance to airflow through bulk grains

Because of the high complexity of bulk grains containing large number of interconnected pores of variable shapes and sizes, plus different bin floor and duct configurations, exact analytical solutions are generally not a feasible option in modeling resistance to flow in grain storage systems. Numerical methods are frequently used in solving the mathematical models for airflow in bulk grains (Smith and Sokhansanj, 1990; Singh et al., 2001; Montross et al., 2002; Lawrence and Maier 2012; Olatunde et al., 2016; Olatunde et al., 2018). Using numerical methods can assist in precise prediction of airflow distribution, analyzing the airflow processes in 3D, and varying physical properties of the grain bed, including pore structure, bin shape, airflow rate, or duct configuration (Navarro et al., 2002). Finite difference and finite element methods are the two numerical methods that have been mostly used in solving models relating to resistance to airflow prediction in stored grain (Navarro et al., 2002). Brooker (1961) developed a finite difference solution for the partial differential equation for predicting resistance to airflow distribution in rectangular bin containing wheat. Brooker (1969) applied finite difference methods to predict resistance to airflow through maize stored in a rectangular bin. Jindal and Thompson (1972) used the finite difference approach to predict 2-D distribution of resistance to airflow and 3-D airflow distribution in triangular

cross-section- shaped pile of sorghum grains. These two models were later modified by Thompson (1975) to predict resistance to airflow for a conical pile of grains. The same solution approach of using the finite difference technique was employed by Lai (1980) and Hood and Thorpe (1992) for predicting airflow distribution in silos. In recent years, there have been more published finite element models for predicting resistance to airflow through bulks grains because the finite difference method becomes more cumbersome for curved and irregular grain storage structures (Navarro et al., 2012). Jayas et al. (1990) developed an axisymmetric finite element model to predict the distribution of resistance to airflow through bulk canola. Lawrence et al. (2013) used the finite element method to predict airflow distribution through stored grain ecosystems. One of the major advantages of using finite element methods is that it can handle complex geometry and variable material properties.

The computation fluid dynamic (CFD) is another numerical technique that has been used in solving mathematical equations for predicting airflow in bulk grains. The CFD method has been investigated for predicting the effects of different transport processes in bulk grains (Garg and Maier, 2005; Lawrence and Maier, 2011; Moses et al., 2014; Olatunde et al., 2017). Garg and Maier (2005) used a CFD software package Fluent to solve a non-uniform airflow distribution model for bulk grains in storage. He applied the CFD model to investigate airflow distribution patterns in peaked grain mass, grain mass with high fine concentrations, and grain mass aerated from a ring duct around the bottom. His results showed that for all the configurations simulated, non-uniform airflow behavior was observed. In the peaked grain mass, the air velocity decreased from 0.0163 ms^{-1} at the air inlet to less than 0.008 ms^{-1} at 1.0 m below the peak of the

grain mass. For the grain mass with high fine material concentrations, the air velocity decreased from 0.0142 m s^{-1} at the air inlet to 0.008 m s^{-1} , which resulted in a 40 % lower effective airflow rate through the grain core versus the rest of the grain mass. Olatunde et al. (2018) used Fluent CFD to investigate the potential of turbulence generation around the network of sensors used in monitoring air and stored grain condition in the bin. Moses et al. (2014) applied COMSOL solver, a CFD software package, to solve a non-linear three-dimensional airflow model for wheat. Their model was based on Darcy's law and it was applied to study airflow distribution in flat and hopper bottom bins. They observed that the pattern of resistance to airflow were different in different bin configurations. Most commercial CFD codes are built on numerical algorithms that solve fluid flow problems in porous media using transport equations. However, the heterogeneous nature of grain bulk, complex dynamics of air flow in the microscopic pores of the grain bed and other diverse factors affecting flow through bulk grains can be difficult to include in mathematical models. Consequently, many simplifying assumptions were considered (Montross et al., 2002; Lawrence and Maier, 2012). Lawrence and Maier (2012) used CFD Fluent to predict airflow distribution in grain bins. However, their study ignored the anisotropic properties of the bulk grain. Khatchatourian et al. (2009) incorporated anisotropic and non-homogenous conditions (geometry and morphology) of bulk grains in their study, but variations in geometry and morphological characteristics of pore structure along the depth of the grain bed were not considered. To improve the accuracy of modeling flow through bulk grains using CFD models, realistic assumptions that accounts for the effect of the complex flow, pore

structure characteristics, as well as the heterogeneous variations of these pore structure characteristics should be considered (Molenda et al., 2005).

3 Materials and Methods

3.1 Materials

The experiments were performed on soybeans in this study. The measured physical properties of the soybeans used in this study are summarized in Table 3.1. The grain moisture content was determined to be 8.82% (wet-basis) by using the standard oven method as outlined in the ASABE Standard: 105°C for 72 hours (ASAE R2008.S352.2, 2011).

Table 3.1 Physical properties of Soybean grain sample.

Moisture content (%wb)	8.82	Sphericity	0.7
Average length (m)	6.2×10^{-2}	Average mass of kernel (kg)	2.2×10^{-4}
Average volume (m ³)	1.8×10^{-4}	Particle density (kgm ⁻³)	1240
Equiv. diameter (m)	6.9×10^{-2}		

The length, width and thickness of each kernel were measured by using a veneer caliper. Fifty (50) soybean kernels were randomly selected for the size measurement. Surface area was calculated using the equation 3.1 (Nwaizu, 2013)

$$S_w = 0.05\pi W^2 \left(1 + \frac{L^2}{W\sqrt{L^2 - W^2}} \sin^{-1} \frac{\sqrt{L^2 - W^2}}{L} \right) \quad (3.1)$$

Where: L = average largest (major) diameter (m), W = average smallest (minor) diameter(m), S_w = surface area of the grain(m^2)

The average volume of the grain kernel was measured by the water displacement method. The samples were placed in a scaled tube filled with water, and the volume of the grain kernels was obtained from the displacement of water. Once the average

volume of the grain kernel was obtained, the equivalent diameter was calculated from the equation 3.2. (Mohsenin, 1986)

$$D_w = \left(\frac{6V_w}{\pi} \right)^{1/3} \quad (3.2)$$

Where: D_w = equivalent diameter of the grain kernel (m), V_w = volume of the grain kernel(m^3). The sphericity of the grain was obtained using the following equation 3.3 (Rumsey, 1981)

$$\varphi_w = \frac{6V_w}{D_w S_w} \quad (3.3)$$

where: φ_w = the obtained sphericity of the soybean grain kernel

The average mass of fifty (50) soybean kernels was obtained by using a digital scale. The particle density (ρ_p) was calculated from ratio of the average mass to the average volume (V_w). These physical property values presented in table 3.1 were similar to those reported by Kibar and Ozturk (2008) and Kenghe et al. (2012) at moisture contents of 8.0% and 8.7%, respectively.

3.2 Experiments

Two different experiments were carried out. The first experiment was to study the effect of compaction due to pressure exerted by the self-weight of grain on porosity and tortuosity (hereafter referred as the compaction test) and the second experiment was to study the effect of compaction due to vibration on porosity and tortuosity (hereafter referred as the vibration test).

3.2.1 Compaction test

A rigid cylindrical model bin of 0.28 m in height and 0.15 m in diameter, made with sheet steel of 1.5 mm thicknesses, was designed and used in this study (fig. 3.1). The bin was equipped with two riveted metal buckles so that the bin could be opened longitudinally for retrieving the grain sample fixed with wax. For each test, the soybeans sample was poured into the model bin to a height of 0.12 m through a funnel placed 0.1 m above the bin (fig. 3.1). It should be noted that the model bin used in this study was relatively small compared with the actual commercial size bins (e.g., 5 m in height). Therefore, the variations in the physical properties (porosity, density, etc.) along the model bin height (0.12 m) were assumed to be negligible. This assumption was confirmed to be valid by the results in Section 4.1. Furthermore, many researchers (e.g., Zhang et al., 1987) used grain samples 0.1 m high in triaxial tests, with an assumption that grain properties were uniform within this grain column 0.1 m high.

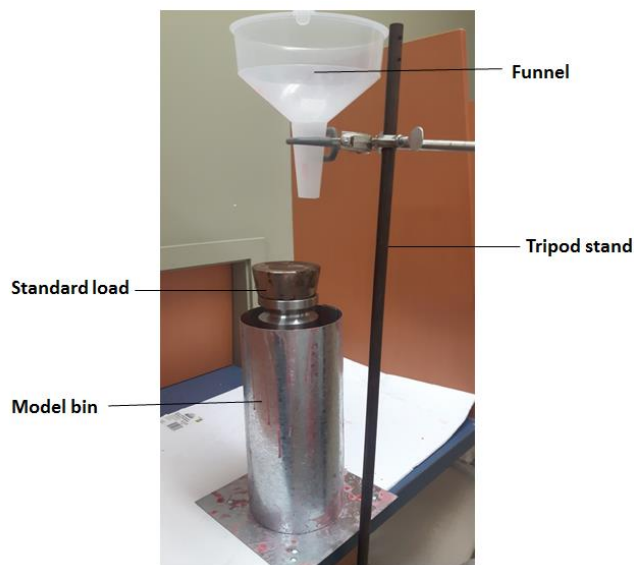


Figure 3.1 Experiment set-up for the compaction test.

This filling procedure was used to ensure a reproducible structure of the soybean grain bed. A similar filling procedure was used by Molenda et al. (2005) to ensure that the bulk density of grain in all experimental runs were the same. After filling, the grain heap was gently leveled manually and then a dead weight was applied on the top surface to simulate the grain mass that exerted a vertical pressure on the test sample. Janssen's (1895) equation (3.4) was solved to determine the vertical pressures, and consequently the over-burden loads (dead weights) that simulated the grain pressure in real storage bins. Calculations were performed for hypothetical bin with a diameter of 5 m and six different grain depths (0.2, 0.5, 1.0, 1.5, 1.8, and 2.2 m). The parameters used in calculating the pressures are as follows; the coefficient of friction between the stored soybean grain and the galvanized metal sheet wall was 0.134, and the bulk density of the soybean grain 731 kgm^{-3} . These values were reported by Onu, 2016. For the lateral to vertical pressure ratio, $K=0.5$ was used (Schwab et al., 1994). The calculated over-burden loads used for the compaction tests are shown in Table 3.2. (Equation 3.5).

$$P_L = \left(\frac{wR}{\mu} \right) \left[1 - e^{-\frac{K\mu h}{R}} \right] \quad (3.4)$$

$$\frac{P_L}{P_V} = K = 0.5 \quad (3.5)$$

Where P_L = Lateral pressure (kPa), P_V = Vertical pressure (over burden pressure) (kPa), R = Radius of the storage structure (m), w = Bulk density (kgm^{-3}), K = Lateral to vertical pressure ratio (dimensionless), and μ = Coefficient of friction (dimensionless).

Table 3.2. Applied loads used for simulated stress condition (vertical pressures).

Depth (<i>m</i>)	Vertical Pressure (kPa)	Load (N)
0.20	1.43	25.28
0.50	3.46	61.24
1.00	6.58	116.25
1.50	9.37	165.68
1.80	11.89	210.08
2.20	14.15	249.97

A preliminary experiment was carried out to determine the duration after which no further compaction would occur for a particular load. The experiment was conducted with the smallest vertical pressure of 1.43 kPa , equivalent to the load of 25.28 N . In the experiment, the bin was filled to a height of 0.12 m and the initial bulk density was estimated from the total volume and the mass of the grain in the bin. A dead weight was placed on the top grain surface through a 500 g rigid disc plate. The settling of grain surface (from which bulk density was estimated) was measured every 24 hours. The result indicated that the maximum (stable) bulk density was achieved after 48 hours. The 48 hours stabilization period was then used in all subsequent experiments.

3.2.2. Vibration tests

The experiment was conducted using a vertical vibration table (Model 307-97056, Cougar Industries Inc., Peru, IL, USA) as shown in figure 3.2. The vibration table was driven by a pneumatic piston with compressed air and controlled by a pressure regulator to achieve different vibration intensities. The table (vibration) was restricted to move only in the vertical direction by three piston-spring assemblies.

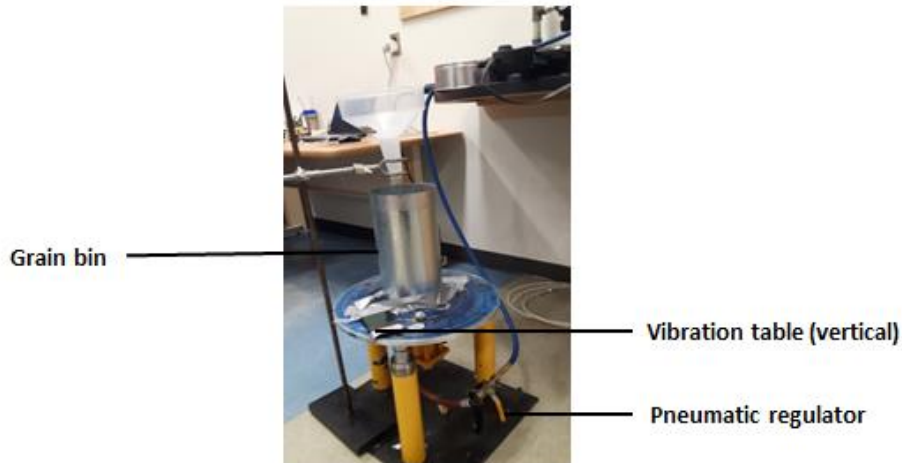


Figure 3.2 Experiment set-up for the vibration test.

A cylindrical model bin of 0.28 m in height and 0.15 m in diameter was used to conduct the experiment. The bin was made of 1.5 mm thick sheet steel and had an observation window of transparent plastic on one side of the wall for visual observation of re-arrangement of the grain kernels during vibration (fig. 3.3).



Figure 3.3 Transparent cut-section windows on the wall for visualization.

The model bin was fixed to the vibration table and soybean sample was poured into the bin using the same method as in the compaction tests to ensure that the grain packing

could be reproduced. The initial packing density was estimated by the ratio of the grain mass to the volume occupied by the grain. The volume was calculated based on the average of the packing heights measured at different positions on the grain surface. The bin was then subjected to vibration for 30 s at known vibration intensities (0.5, 1.0, 1.5, 2.0, 2.5 and 3.0*g*). Where *g* is the acceleration due to gravity expressed in $m s^{-2}$. These intensity levels were chosen based on the observations reported by Jones et al. (1996) that the vibration intensity on structures on the ground at distances of 5 to 80 m from railway traffic ranged between 5 to 10*g*. Also, equipment commonly used for bulk grain handling, such as fans, elevators; augers and so on usually cause vibration at frequencies between 18 Hz and 50 Hz (Ge et al., 2000). Recent studies by Feldbusch et al. (2017) indicated the potential of mobile devices for vibration analysis, system identification and structural monitoring using smartphone apps. They carried out a verification study to compare professional accelerometers and smartphone vibration sensor app with benchmark tests conducted under laboratory conditions by means of two beams of different stiffnesses (1.8 Hz and 12.5 Hz), representing a low and high-frequency system. The beams were excited by tapping and the acceleration was recorded with smartphone app until complete decay of the vibration and the results were compared with that obtained from a professional measuring device. They concluded that although the characteristics of accelerometers installed in smartphones differ from professional acceleration sensors, however, smartphone successfully measured vibration in the range of 4 *g* (and more) depending on the sensors in the smartphone. An iOS based smartphone with vibration analyzer app (VibroChecker, ACE International, Langenfeld, Germany) was attached firmly with duct tapes to the surface

of the vibration table to enable the smartphone vibrate rigidly together with the vibration table. The iOS based smartphone vibration analyzer app was used to indicate the different vibration intensity at each adjusted pressure regulator use to control compressed air that drove the vibration table to achieve the desired vibration intensities (0.5, 1.0, 1.5, 2.0, 2.5 and 3.0g).

3.2.2 Stabilizing pore structure of test samples

Colored (red) paraffin wax bar slowly melted at 35 °C to form a liquid wax was gently poured into the grain sample in the bin to stabilize (fix) the pore structure of the test sample after compaction or vibration. The liquid wax flowed into pore spaces of the sample and was allowed to solidify at room temperature. Once the sample was “fixed” (wax solidified), the grain sample was extracted from the bin by releasing the metal buckles that held the bin together. An electrical saw was used to cut out three cylindrical sub-samples of 0.04 m in thickness and 0.15 m in diameter from the top, middle and bottom regions of the extracted sample (fig. 3.4). The compaction and the vibration tests were repeated three times at each compaction pressures and vibration intensities.

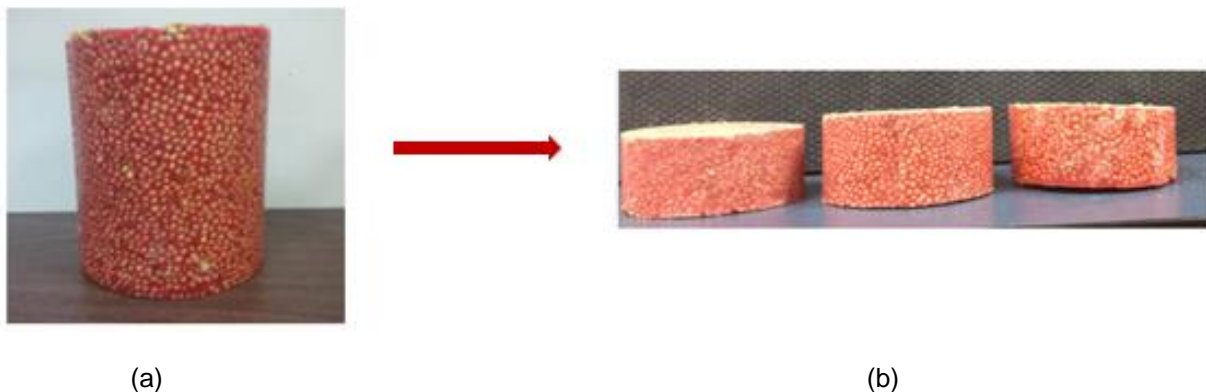


Figure 3.4 Example of (a) extracted sample and (b) three subsamples cut from the top, middle, and bottom of the sample.

3.3 Image analysis

3.3.1 Image acquisition

Immediately after cutting out the sub-samples from the wax-stabilized sample, surfaces of the of the sub-samples were gently cleaned with soft paper to clean ground particles of grain kernels from the surfaces and an image of the cross section was captured with an HD camera (Exilim EX-F1 Casio Computers Co., Ltd, Tokyo, Japan). The images obtained were processed and used for quantifying 2D parameters of the pore structures. For the 3D reconstruction, each of the sub-samples were further cut into disc of $0.01m$ thickness and the surface of each of discs were imaged and reconstructed with 0.2 cm space between each disc image during image analysis to obtained a 3D volume of each sub-samples.

3.3.2 Image processing methods

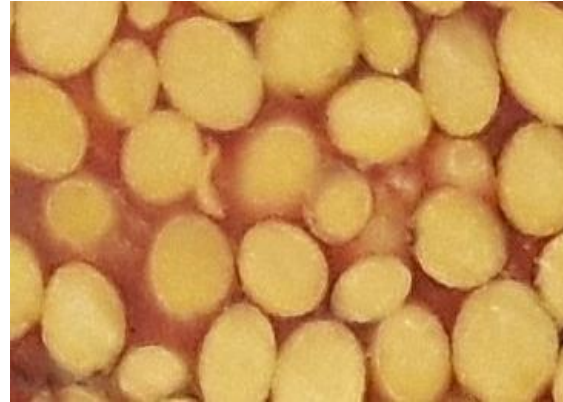
The acquired images were processed with ImageJ, a Java-based image processing software developed by the United State National Institute of Health (NIH, Bethesda, MD, US). The image analysis procedures used in this study were grouped into four main steps: Pre-processing, Segmentation, 3D volume reconstruction, and pore detection and measurements.

3.3.2.1 Image pre-processing

All images were resized to 362×229 pixel to include the area with vivid details of the pores across the section (fig. 3.5) and then the RGB images were pre-processed to ease the identification and quantification of pores during measurements (fig. 3.5).



(a)



(b)

Figure 3.5 Example of the (a) RGB 2D section image re-sized to (b) Region of interest (ROI) of size 362 x22 pixels.

A uniform contrast enhancement filter was applied to normalize all the section images and reduce the effect of differences in the pixels between neighboring sections. The images were then sharpened by deconvolving an unsharpened kernel out of each pixel by using an alpha value of 1. Finally a noise reduction filter, median filter, was applied to all the images to reduce sparse noise within the image by setting each pixel in the image to be equal to a median pixel value of its specified neighborhood ((Schneider et al., 2012) (fig 3.6).

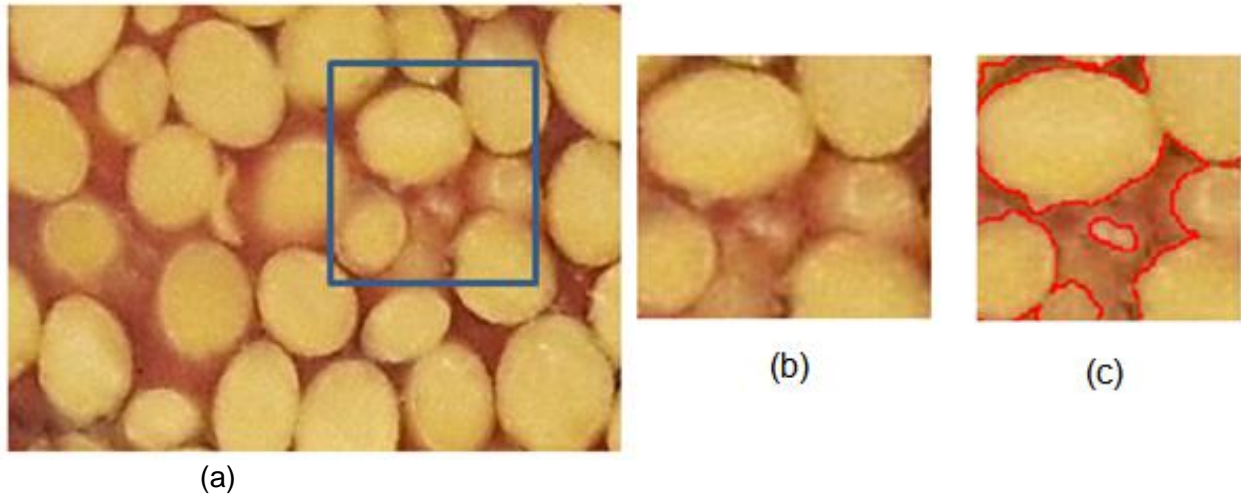


Figure 3.6 Example of RGB image with noise at the grain kernel boundaries (b) close-up view showing the blurred grain kernel boundaries (c) close-up image after noise reduction filter has been applied.

3.3.2.2 Image segmentation

Most images after pre-processing had marginal distribution of the pixel values representing grain kernels overlapped with those representing pores. This introduced a certain amount of noise into the images which were mostly evident at pore-grain kernel boundaries and manifested as a tiny pores or tiny kernel points within the pores.

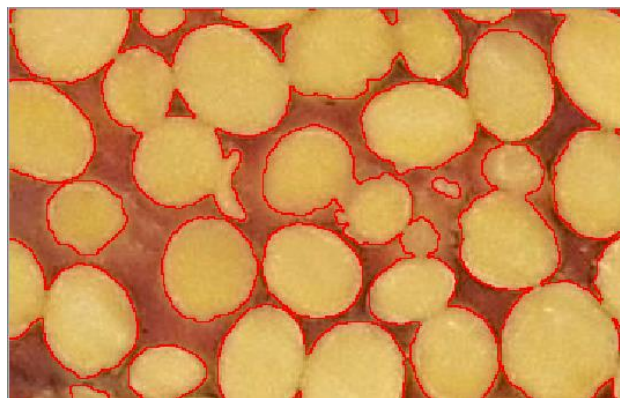


Figure 3.7 Example of RGB image after erosion and dilation operation.

A significant amount of this noise would affect results during quantification of the pore structure characteristics. To reduce this noise, a morphological filter was applied to all images (Schneider et al., 2012). The filter operation consisted of two sequential applications, i.e., the dilation and erosion operations using the same specified threshold number to sequentially grow and shrink features that were surrounded by a number of selected pixel greater than or equal to the specified threshold value in an image under consideration. For these operations, the same threshold value that corresponded to the size of the noise features was used to separate the noise features from the images (fig. 3.7). As a result of morphological filtering operations, irregular small features introduced by noise were eliminated (fig. 3.8a-b).

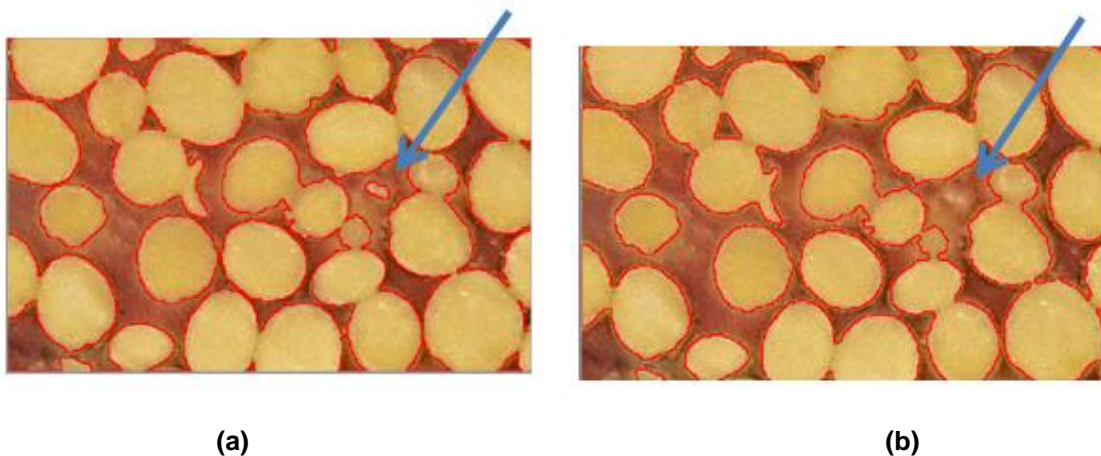


Figure 3.8 Image representation of the (a) presence and (b) elimination of irregular features.

The connected (touch) grain kernel features were separated using a built-in watershed algorithm in ImageJ based on the principle of segmentation that involved creating a separation at the point where two local intensity minima were joined together. An example of the resulting image after the application of the watershed is shown in figure 3.9.

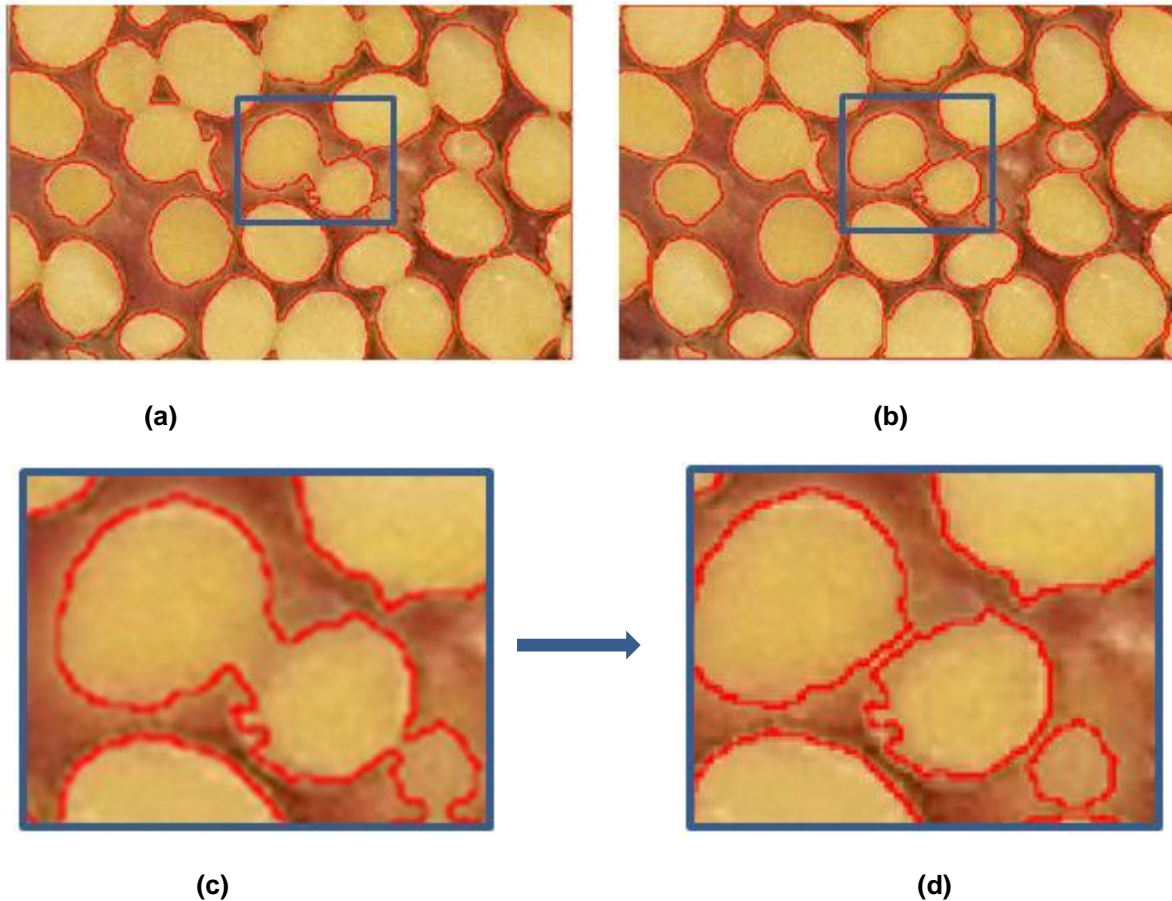
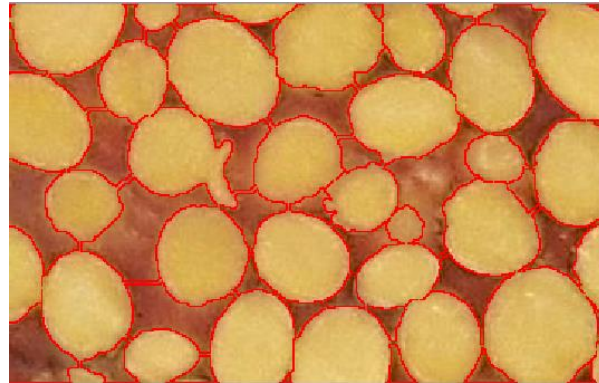


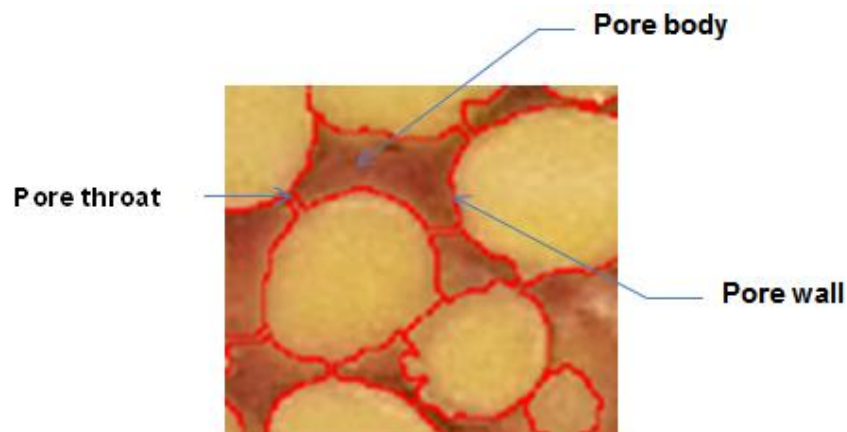
Figure 3.9 RGB image of the red wax-filled pores of soybean grain: (a) conjoined grain kernels after the previous image processing operations; (b) result of imageJ watershed algorithm to separate the conjoined grain (c) and (d) show close-up view of (a) and (b), respectively.

Pore structure partitioning was carried out in a similar way as in partitioning the connected grain kernels. All adjoining pores with no obvious geometrical connecting throats were automatically identified by ImageJ and the boundaries between the connected pores were separated using the watershed macro in ImageJ that implemented an iterative algorithm based on a morphological thinning technique (Tsukahara et al., 2008). This technique was based on the principle of segmentation that created a separation at the point at which two local intensity minima were joined

together (Tsukahara et al., 2008). Figure 3.10a-b shows an image after pore separation was performed using watershed.



(a)



(b)

Figure 3.10 RGB image of the red wax filled pores of soybean sample. (a) result of ImageJ watershed algorithm to separate pores; and (b) close-up image of a local area.

Once the pores had been partitioned, the 2D section images were converted to 8 bit-images before segmentation.

Segmentation of an image is the process of separating each pixel of the image as being a member of any one of two or more set (Rizk et al., 2014). In this study, all the images of the 2D sections were segmented based on a threshold value that separate the pixels

that belong to the red colored wax that filled pores from the pixels of yellow grain kernels. This created binary images with intensity value of 1 (white) for the grain kernels and 0 (black) for the pores in the image (fig. 3.11). Several built-in thresholding algorithms in ImageJ such as Otsu's algorithm and Maximum Entropy algorithm were tested on the images. However, results obtained were not satisfactory. So in this study, the method for selecting threshold value was subjective. The method involved increasing the pixel value gradually until the image agrees with the visual inspection of the unedited image.

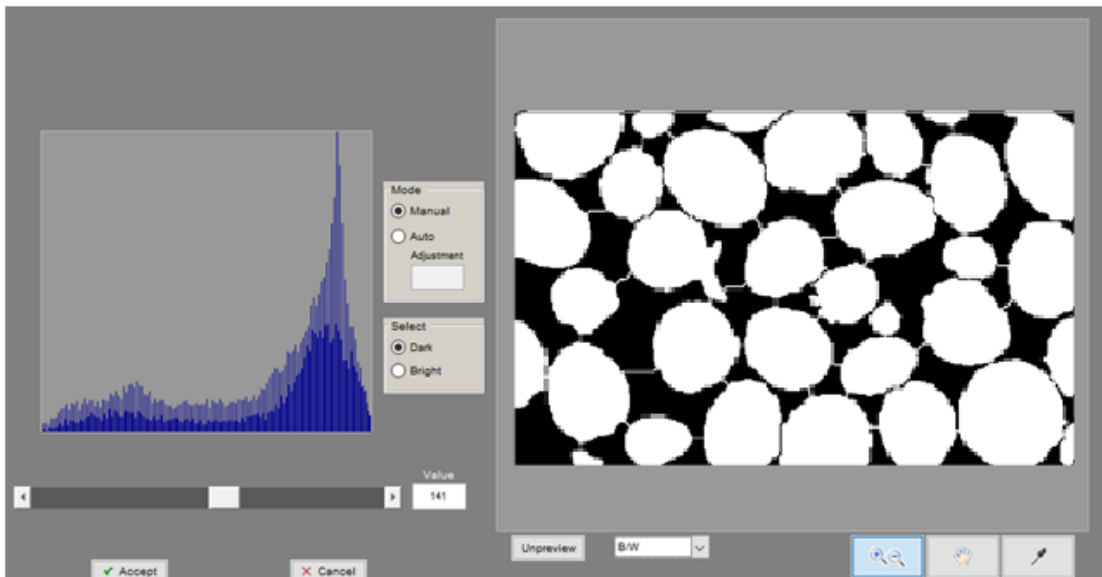
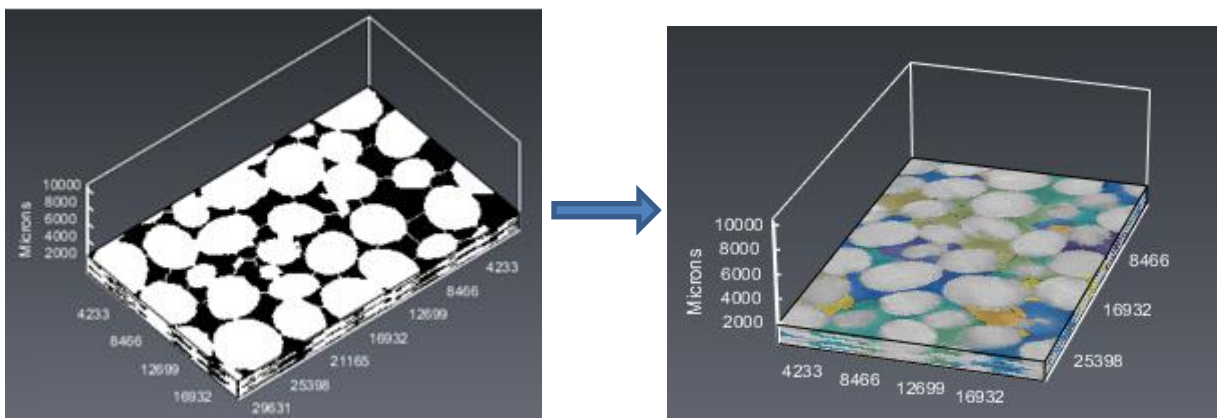


Figure 3.11 Segmented image of a 2D section showing the image after binarization into pores (black) and grain (white) with the thresholded histogram based on manual setting.

3.3.2.3 Three- Dimensional (3D) image reconstruction

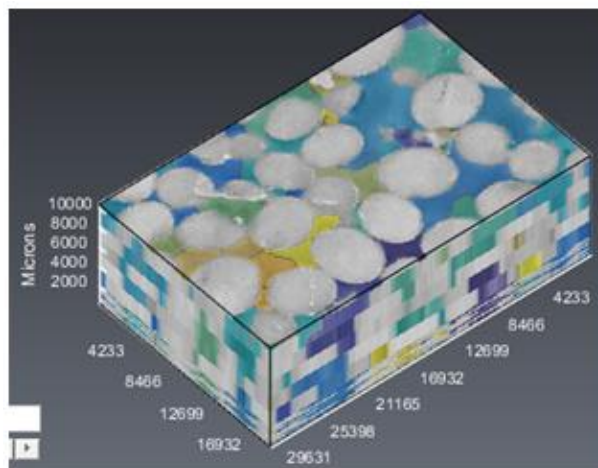
Three dimensional (3D) images were constructed from the obtained 2D images by using the 3D Xlib plug-In in ImageJ (Munch, et al., 2006). This 3D plug-In was designed for constructing a 3D volume from 2D section images. First, the pores in the 2D

thresholded binary images were separated with colors (blue, green and yellow) of different intensities to represent the different pores sizes. These 2D images with colour separated pores were then stacked (aligned) by using StackReg, another ImageJ plug-in (Thevenaz et al., 1998). The plugin aligned image slices by registering the slices in turn; each slice was used as the template with respect to which the next slice was aligned, so that the alignment proceeded by propagation from the first slice to the last (Thevenaz et al., 1998). And then the 3D Xlib ImageJ plug-in was applied for the 3D reconstruction. Figure 3.12a-c graphically illustrates process of constructing the 3D images from 2D sections.



(a)

(b)



(c)

Figure 3.12 Graphic illustration of 3D image construction. (a) 2D slice section images of 0.2 cm thickness (b) 2D slice section image with colour separated pores of 0.2 cm thickness stacked and aligned; (c) constructed 3D volume.

The reconstructed 3D images could provide not only a quantitative data sets for estimating some critical parameters of pore structure but also a means of visualizing all the pore channels within the bulk grain.

3.3.3 Quantification of pore structures from 3D volume images

Once the 3D reconstructed volumes were obtained, some critical pore structure parameters, including porosity and tortuosity, were quantified by using the 3D Xlib plugin in ImageJ (fig. 3.13). The pores in the 3D images were identified according to the pore definition given by Dullian et al. (1992), that is, a pore is a portion of the pore space bounded by a solid surface and planes erected where the hydraulic radius of the pore space exhibit local minima. This was implemented in ImageJ by the use of the watershed macro (Tsukahara et al., 2008). After pores were identified and the pore volume was calculated, porosity was estimated as the ratio of the total pore volume to the total sample volume as follows:

$$\varepsilon = \frac{V_p}{V_s} \quad (3.6)$$

where ε =porosity, V_p = total pore volume (voxel), V_s = total sample volume (voxel)

The degree of pore connectivity in a given bulk grain determines to a great extent how “easy” fluid can flow through the bulk grain. Not all the pores in a porous medium are connected (there exist dead pores) and only connected pores formed flow paths.

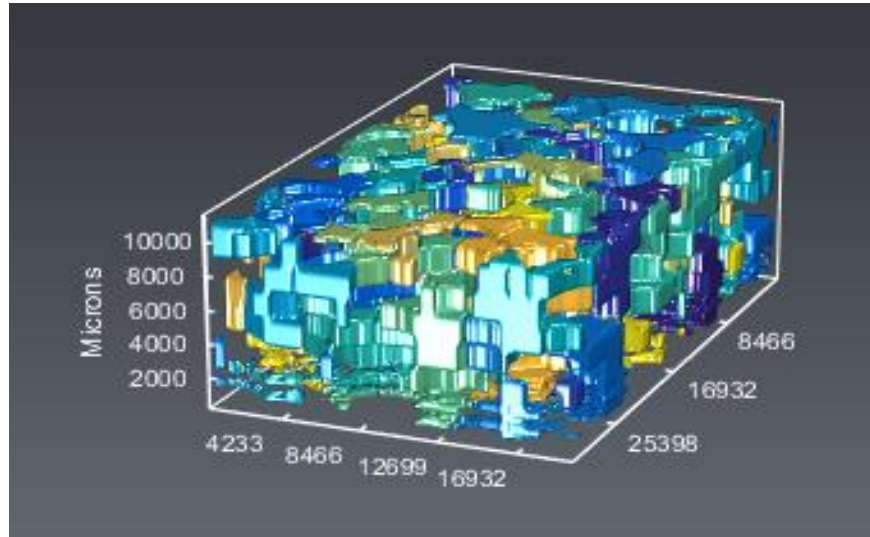


Figure 3.13 Airflow paths (each color shades represent an individual inter-connected paths) within a 3D volume

In this study, the degree of connectivity was estimated based on the volume ratio of the inter-connected pores that formed flow paths to the total pore volume estimated using the connectivity function in the 3D Xlib ImageJ plug-in that automatically connected the pores having the same colour intensity through the stack.

$$c = \frac{V_{lp}}{V_s} \quad (3.7)$$

where c = degree of connectivity, V_{lp} = volume of the inter-connected paths (voxel), V_s = total pore volume (voxel).

Tortuosity is grossly defined as the ratio between the effective length of (tortuous) flow path and the nominal length of flow path. However, the effective length becomes elusive given that fluid flow branches at any point within the porous bed. So, the question is: which branch(es) should be considered in determining the effective length? Researchers have used different ways of “measuring/determining” the effective length. (Sobieski et al., 2012; Nwaizu and Zhang, 2015, Yue and Zhang, 2017). Sobieski et al.

(2012) predicted tortuosity for airflow through porous beds consisting of randomly packed spherical particles by using geometrically constructed *shortest* flow branch (path). Nwaizu and Zhang (2015) determined tortuosity based on the *shortest and longest* flow branches within a soybean grain bed. Yue and Zhang (2017) estimated geometric tortuosity based on *the narrowest and the widest* flow branches in simulated porous beds consisting spherical particles.

In this study, we presented a new approach of determining tortuosity from multiple airflow paths (branches) that are inter-connected. Specifically, the effective length was determined as the length of a flow path that had the highest degree of connectivity.

Since flow would naturally follow the least resistance paths among the notoriously complex, bundles of flow paths that exist within a given grain bed, the inter-connected airflow path with the highest degree of connectivity was identified from all the 3D reconstructed airflow paths. This inter-connected airflow paths with the highest degree of connectivity would contribute more to flow when compared to the single isolated widest, narrowest, shortest, or longest airflow path. Some examples of identified flow paths with the highest degree of connectivity are illustrated in Appendix A.

Once a flow path with the highest connectivity was identified (fig.3.14), its image was skeletonized with Skeleton3D an ImageJ plug-in (Ignacio Arganda-Carreras et al., 2010) to obtain the effective path length. Figure 3.15 shows an example of the steps in obtaining the skeletonized image of the inter-connected flow braches with the highest connectivity. First, the image of the 3D inter-connected flow path was converted to a 2D stack binary image. Then, this image was fed into Skeleton3D plug-In in ImageJ, in which a thinning algorithm was used to reduce all the volumes in the image to their

center-lines while keeping their morphological information in order to estimate euclidean path length and effective lengths use to determine the tortuosity value.

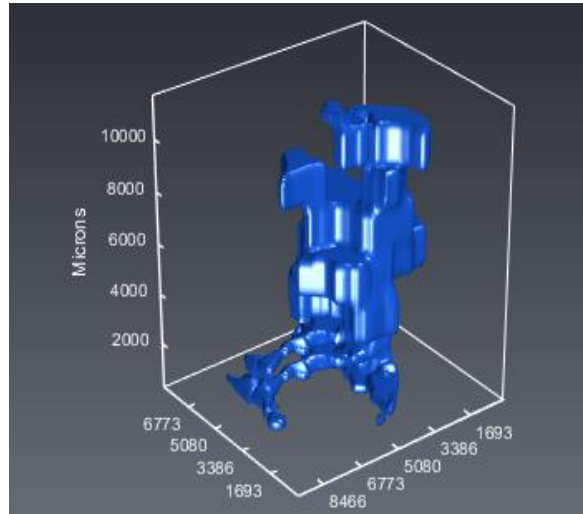


Figure 3.14 Extracted 3D reconstructed of the inter-connected paths with the highest degree of connectivity.

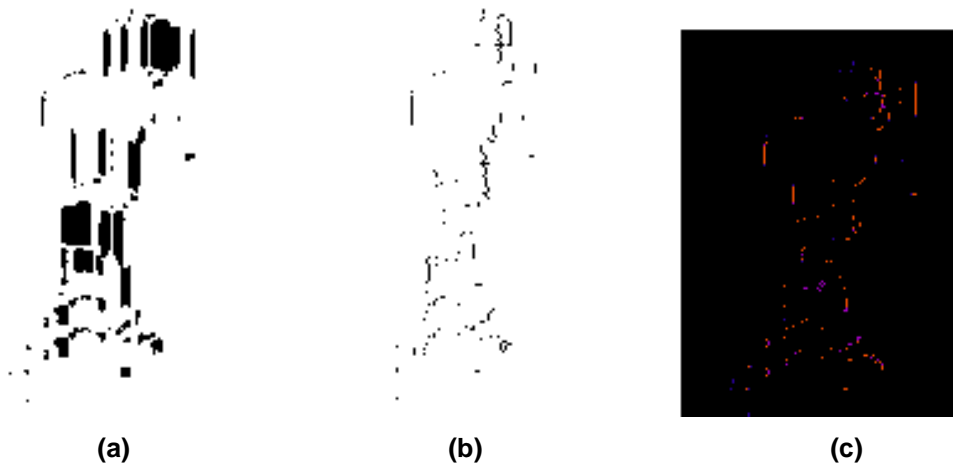


Figure 3.15 Result of direct skeletonization process from (a) binary image of the inter connected flow paths with highest degree of connectivity and applied Skeleton3D to obtain (b) thin skeletonized image, which was then analyzed by analyzedSkeleton3D to formed (c) pruned thin skeletonized image from which different possible paths/branches from the thin skeleton were estimated.

3.4 Statistical analysis

Statistical analyses were carried out with SAS (Statistical Analysis Systems, version 9.4, 2016) to analyze the effect of various factors on porosity and tortuosity. Analyses of variance (ANOVA) were conducted to determine which of the factors had a significant effect on porosity and tortuosity. An effect was considered significant if $P < 0.05$. The Tukey test was employed to compare means of samples. Residual and R-student curves were plotted for testing the normality. When mathematical were fit to experimental data, fitting was carried out using non-linear functions with coefficient of determination (R^2) and the standard error of estimate (SEE) for evaluating the goodness of fit. The SAS codes used in all analysis and results were illustrated in Appendix B.

3.5 CFD simulations

3.5.1 Overview of the CFD Fluent simulations

The empirical porosity and tortuosity models developed from the experimental data were incorporated into flow equations in CFD models to numerically investigate the effects of pore structure on airflow through grain bulks. A commercial CFD software package ANSYS Fluent (ANSYS, Version 17.2, Canonsburg, PA, USA) was used to conduct CFD simulations. The simulation steps are illustrated in the flowchart in Figure 3.16.

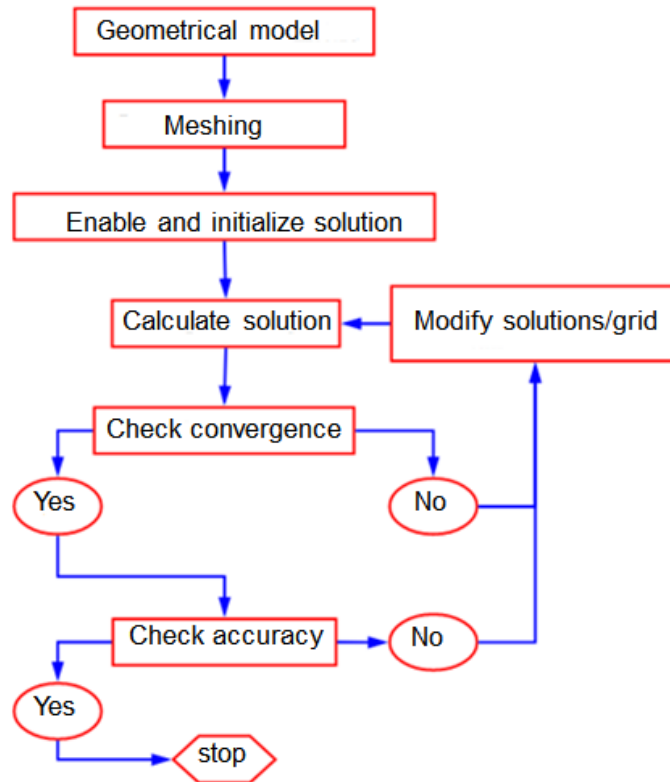


Figure 3.16 CFD Fluent-simulation process.

Simulating variations in pore structure (porosity and tortuosity) is not currently available as a standard feature in any commercial CFD package, including ANSYS Fluent. Therefore, the empirical models (Equations 4.1 and 4.3) developed from the experimental data describing the variation in porosity and tortuosity as a function of grain depth were incorporated as source terms in the Fluent solver by developing user-defined functions (UDF) using C programming language. The UDF(s) developed in this study were coded in their entirety, and then verified to work as expected before being compiled into Fluent for simulations. Details of UDF(s) developed were presented in Appendix C and formulation details are discussed in Section 3.5.2.

In all the CFD simulations, the soybean grain was considered as a porous media and air was considered as the flowing fluid. Airflow from the aeration/drying fan was assumed constant and the momentum transfer was modeled as a steady-state process. The results from the model simulations were validated against experimental results reported in literature by Khatchatourian et al. (2004). The models were then applied to flat bottom grain storage structures to study the effect of bin floor configurations, aspect ratio (H:D, height to diameter) and flow direction on air velocity and static pressure distribution in the grain bulk. Generalized fluid flow and energy balance based on the Navier Stokes equation were implemented in the ANSYS Fluent CFD code by using the Porous Media Model and the User Defined Functions (UDF). For this study, UDF's were developed to modify the generalized model by incorporating pore structure variation into the simulations. The κ - ϵ equations were used to introduce turbulent effect into the simulations (Olatunde et al., 2016). The simple pressure-velocity coupling algorithm was used to iteratively solve the governing equations, discretized by the second-order upwind differencing scheme with Under Relaxation Factors (URF's) reduced to 10^{-4} to 10^{-6} as the appropriate URFs for all simulations. This URF was chosen by trial and error to stabilize the iterative process and cause the UDF hooked-simulation to converge to a solution. After the simulation had converged, the post-processing interface was used to produce contour plots to illustrate the flow patterns or details at specific locations. Also, some of the quantitative data were exported into Microsoft Excel for further analysis.

3.5.2 CFD Fluent formulation for compaction effect due to grain pressure

The governing equations under porous media formulation in Fluent included the continuity and momentum equations representing the conservation of mass and momentum respectively (Olatunde et al., 2016).

$$\frac{\partial p}{\partial t} + \frac{\partial(\rho u_i)}{\partial x_i} = 0 \quad (3.8)$$

$$\frac{\partial \rho}{\partial t} + \frac{\partial(\rho u_i)}{\partial x_i} = \frac{\partial P}{\partial t} + \rho g_i + \frac{\partial}{\partial x_j} (\mu + \mu_t) \left(\frac{\partial u_i}{\partial x_j} + \frac{\partial u_j}{\partial x_i} \right) + S_i \quad (3.9)$$

where ρ the air density ($kg\ m^{-3}$), t is time (s), u_i and u_j are the average superficial velocity component respectively ($m\ s^{-1}$), p is the static pressure (Pa), μ is the viscosity ($Pa\cdot s$) and S_i is the source term for the momentum equation. g_i is the acceleration due to gravity (ms^{-2}).

The momentum source term S_i is given as follows (ANSYS version 17.2, Canonsburg, PA).

$$S_i = - \left(D_{ij} \mu u + C_{ij} \frac{1}{2} |u| u \right) \quad (3.10)$$

Where D_{ij} = the viscous resistance coefficient C_{ij} = inertial resistance coefficient

The terms D_{ij} and C_{ij} are represented in ANSYS Fluent as the inverse of the viscous loss coefficient α and the inertial loss coefficient C_2 respectively (ANSYS Inc.: Fluent 6.3 User's Guide, Chapter 7.2.3: Porous Media Conditions, September 2006). The viscous loss coefficient α and inertial loss coefficient coefficients C_2 were derived from Ergun's equation presented in Eq. 3.9 (Ergun, 1952; Lawrence and Maier, 2012)

$$\frac{\Delta P}{L} = \frac{150\mu(1-\varepsilon)^2}{d_p^2\varepsilon^3}u + \frac{1.75\rho(1-\varepsilon)}{d_p\varepsilon^3}u^2 \quad (3.11)$$

as

$$\alpha = \frac{150(1-\varepsilon)^2}{d_p^2\varepsilon^3} \quad (3.12)$$

$$C_2 = \frac{3.5(1-\varepsilon)}{d_p\varepsilon^3} \quad (3.13)$$

Where d_p is the average particle diameter, ε is the porosity, μ is the viscosity (Pa.s), $\frac{\Delta P}{L}$ is the static pressure drop

Therefore, D_{ij} and C_{ij} were expressed as:

$$D = \frac{1}{\alpha} = \frac{d_p^2\varepsilon^3}{150(1-\varepsilon)^2} \quad (3.14)$$

$$C = C_2 = \frac{3.5(1-\varepsilon)}{d_p\varepsilon^3} \quad (3.15)$$

The empirical model for porosity variation due to compaction by grain pressure (depth) developed in chapter 4 was used to substitute porosity ε in equation (3.14) and (3.15):

$$D = \frac{d_p^2(\varepsilon_o - B(1 - e^{-\lambda z}))^3}{150(1 - (\varepsilon_o - B(1 - e^{-\lambda z})))^2} \quad (3.16)$$

$$C = \frac{3.5(1 - (\varepsilon_o - B(1 - e^{-\lambda z})))}{d_p(\varepsilon_o - B(1 - e^{-\lambda z}))^3} \quad (3.17)$$

User Defined Functions (UDF) was developed based on equations (3.16) and (3.17) and incorporated into the momentum equation (3.7) through the source term equation

3.8. The k - ε turbulence model in Fluent (eqns. 3.16, 3.17, and 3.18) was used to simulate flow turbulence (ANSYS Inc.: Fluent 6.3 User's Guide, Chapter 12: Modeling Turbulence, September 2006).

$$P = p + (1/2)k \quad (3.18)$$

$$\frac{\partial(k)}{\partial t} = \frac{\partial}{\partial x_j} \left[\left(\mu + \frac{\mu_t}{\sigma_k} \right) \frac{\partial k}{\partial x_j} \right] + \mu_t S^2 - \rho \varepsilon \quad (3.19)$$

$$\frac{\partial(\varepsilon)}{\partial t} = \frac{\partial}{\partial x_j} \left[\left(\mu + \frac{\mu_t}{\sigma_\varepsilon} \right) \frac{\partial \varepsilon}{\partial x_j} \right] + \frac{\varepsilon}{k} (C_{1\varepsilon} \mu_t S^2 - \rho C_{2t} \varepsilon) \quad (3.20)$$

$$\mu_t = C_\mu \frac{k^2}{\varepsilon} \rho \quad (3.21)$$

Where, p is the pressure (Pa), k is the turbulent energy ($m^2 s^{-2}$), μ_t is the mean turbulent viscosity (Pa s), $C_{1\varepsilon}$, C_{2t} , σ_k and C_μ are constants. S is the mean modulus of the rate of strain tensor.

The effect of tortuosity variability due to compaction was also introduced into the flow simulation through the formulation of a standard effective diffusivity in Fluent as follows (ANSYS Inc.: Fluent 6.3 User's Guide, Chapter 7.2.3: Porous Media Condition, September 2006). The porosity and tortuosity variation models for c

$$D_{eff} = \frac{\varepsilon}{\tau} \delta_p \quad (3.22)$$

Where D_{eff} is the diffusion coefficient of air flowing through pores of size δ_p , ε is the porosity, and τ is the tortuosity. Compaction due to grain depth developed in chapter 4

were used to substitute porosity ε and tortuosity τ , respectively in equation (3.22) and the modified equation is obtained as follows:

$$D_{eff} = \frac{(\varepsilon_o - B(1 - e^{-\alpha z}))}{(a - b \ln(\varepsilon_o - B(1 - e^{-\alpha z})))} \delta_p \quad (3.23)$$

The above equation was used to develop a User Define Scalar (UDS) (see details in Appendix C), which was incorporated into the Fluent CFD model through the diffusivity equation 3.19.

3.5.3 Geometry

Cylindrical flat-bottom grain storage bins with different air duct configurations and aspect ratios were used in the CFD simulations. The dimensions of bins are illustrated in figs. 3.17, 3.18 & 3.19. In figure 3.17, three layouts of air ducts, namely rectangular, cross and circular partial perforated flooring were considered to investigate the effect of commonly used partial floor configurations on airflow in grain bins. The three bins had the same diameter of 8 m filled to a grain depth of 10 m (that include both the eave height of 7 m and the grain peak depth 3 m). The three bins also had the same air inlet cross section area. Figure 3.18 shows three storage bins with different aspect ratio: H:D= 0.75, 1.00 and 1.50 (H:D, height to diameter). The three bins had the same diameter 8 m but different grain depths of 6, 8, and 12 m, respectively. Figure 3.19 represents two different configuration of horizontal airflow. The first configuration (fig. 3.19a) consisted of four cylindrical perforated tubes (aerators) 1.0 m in diameter and 7.0 m long, installed vertically at equidistant along the bin circumference to serve as the inlets. Air moved radially from the aerator tubes towards an outlet tube (1.0 m in

diameter and 10 m high) placed at the center of the bin. The second configuration (fig. 3.19b) featured a cone-shaped inlet duct system. The inlet consisted of four perforated cone-shaped tubes (7 m high with a base diameter of 1 m) equidistantly spaced along the bin circumference as air inlets, and a perforated cone-shaped tube (10 m high with a base diameter of 1 m) located at the center of the bin extending from the floor to the grain surface to serve as the outlet.

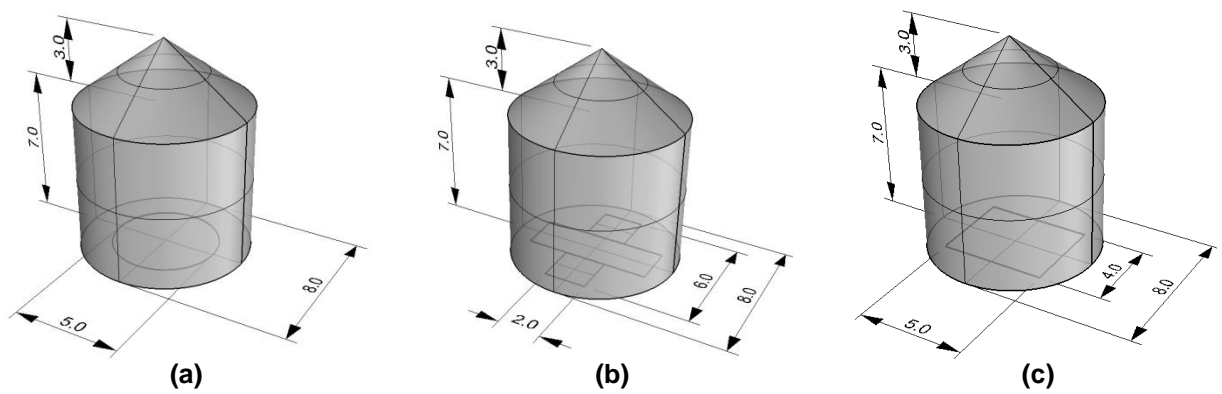


Figure 3.17 Three-dimensional model geometry for the flat-bottom grain storage bins with (a) circular partial perforated floor configuration (b) cross partial perforated floor configuration (c) rectangular partial perforated floor configuration.

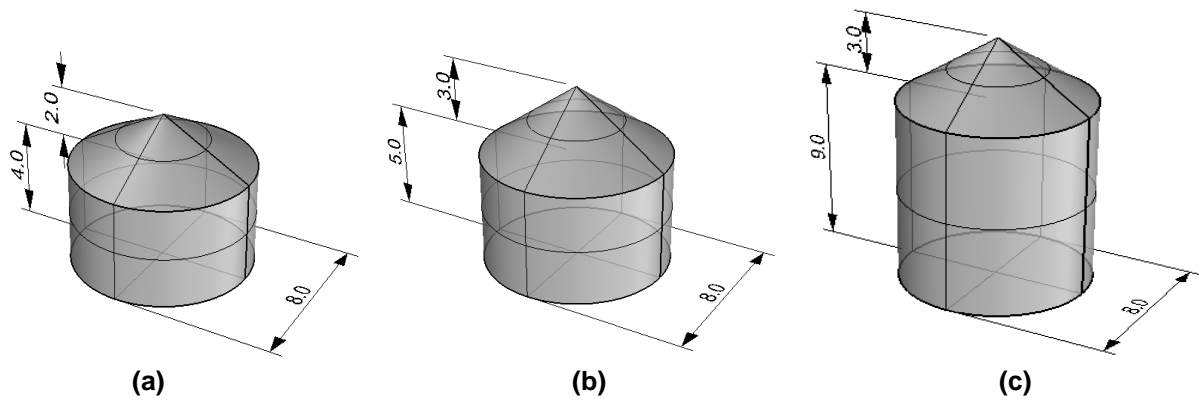


Figure 3.18 Three-dimensional model geometry for the flat-bottom grain storage bins with different aspect ratios (a) H:D = 0.75 (b) H:D = 1.00 (c) H:D = 1.50.

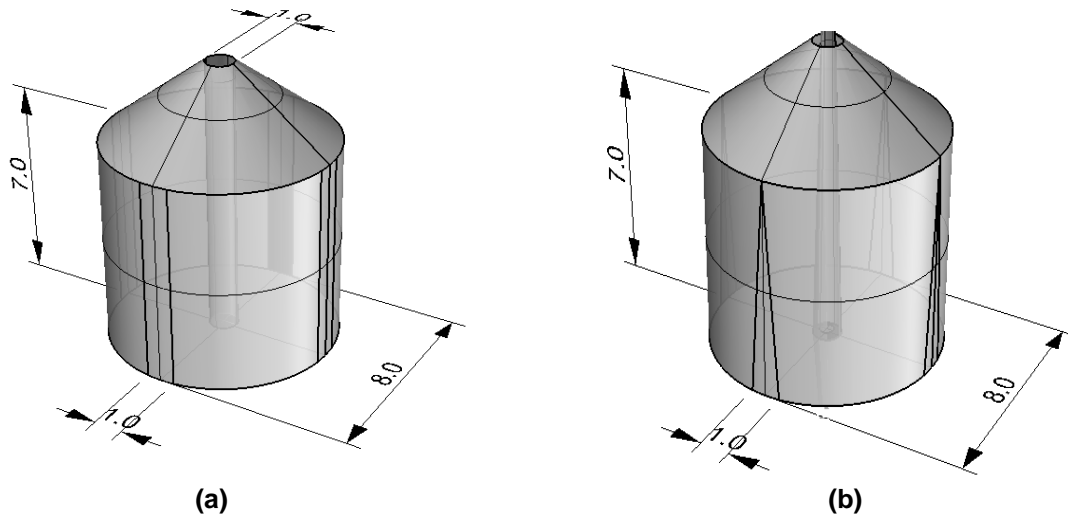


Figure 3.19 Three-dimensional model geometry for the flat-bottom grain storage bins with horizontal airflow (a) cylindrical-shaped tube inlet (b) cone-shaped tube inlet.

3.5.4 Mesh generation

Geometrical models of the storage structures were developed with AUTOCAD (Autodesk Inc., AutoCAD 2016, San Rafael California, USA) and 3D-Rhinoceros (Robert McNeil & Associates, Rhino3D Version 5, Seattle WA USA), and then imported into Fluent. Meshing was developed with the ANSYS built-in meshing tool to create 3D tetrahedral cells. Meshing could significantly affect the accuracy of the simulation results and the computation time. If the mesh is too coarse, the solution might not converge or errors might be large. Conversely, if the mesh is too fine, the solution time might be unnecessarily long. Mesh independence analysis were carried out by continuously refining the tetrahedral mesh and comparing the predicted distributions of airflow velocity and static pressure for the different mesh sizes. It was found that these two key variables (airflow velocity and static pressure) for mesh sizes 0.4 mm and 0.2 mm were

mostly indistinguishable. Therefore, subsequent simulations were conducted with mesh sizes between 0.2 mm and 0.4 mm for all the geometrical models.

Details of mesh independence test results for the fully perforated; partially perforated, and horizontally airflow geometry models were presented in Appendix C. To ensure that the tetrahedral meshes used in this study were reliable to produce a stabilize solution without divergence errors for all the geometrical models used for the simulations, convergence analyses were carried out. The residual RMS error values were monitored and ensured to reduce to an acceptable value ($<10^{-4}$) for all simulations.

3.5.5 Simulation parameters and boundary conditions

The wall boundary condition was used on the inwards facing surfaces of the containing structures to represent the contact area between the air and solid phase with no slip condition to simulate that there were no fluid flows through the wall boundary. The air inlet and outlet were specified as locations at which air entered and left the grain storage system, respectively (Appendix C). The base of the bin was set as a velocity-inlet boundary condition with uniform velocity inlet based on the designed flow rate of $0.0016 \text{ m s}^{-3} \text{ t}^{-1}$ which was sufficient to supply inlet superficial velocity typical for grain aeration. The grain surface was used as the exits described by pressure outlet boundary condition set at zero-gauge atmospheric pressure to model that the system was open to the atmosphere (Collins et al., 2015; Olatunde et al., 2017). Table 3.3. summarizes the main physical properties of air that were initialized in the CFD simulations, considering the turbulence effect that could occur at the interface between the plenum and the porous grain bulk as air flow from the plenum into the porous bed

(Galvan et al., 2011; ANSYS Inc.: Fluent 6.3 User's Guide, Chapter 7.2.2: Determination of Turbulence Parameters, September 2006).

Table 3.2 Physical Properties of air used in the simulations.

Property	Values	Unit
Density	1.2	kgm^{-3}
Fluid viscosity	1.7×10^{-5}	$Pa.s$
Turbulent Kinetic Energy	3.75×10^{-7}	m^2m^{-2}
Turbulent Dissipation Rate	8.66×10^{-11}	m^2m^{-3}

3.6 Pore-scale geometrical models based on compaction for predicting resistance to airflow

3.6.1 Geometrical model for predicting resistance to airflow in the horizontal direction

Bulk grain in a storage bin may contain billions and trillions of pores. Compaction by the self-weight of grain would change the characteristics of pore structure of the grain bulk in the bin, which consequently leads to changes in the airflow velocity and pressure drop through the grain bulk. Generally speaking, compaction results in smaller pores at the bin bottom. In other words, each layer of grain in the grain bed would be subjected to different compaction and the size of flow channels (pores) within the grain bed would decrease with the grain depth. We propose herein to use cylindrical tubes to represent flow channels in the grain bulk and the tube diameter decreases with the grain depth. The proposed geometrical model is based on the following assumptions: (1) the porous medium has simple pore structures that could be represented by cylindrical tubes; and (2) flow is incompressible and laminar. If air flows in the horizontal direction, the air goes through cylindrical tubes arranged in parallel (fig. 3.20).

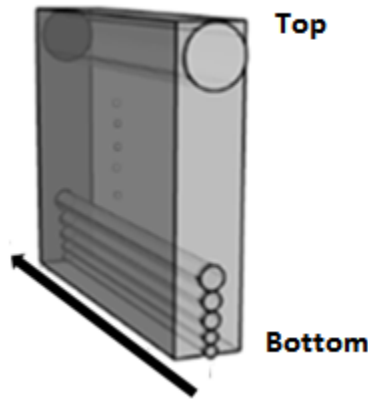


Figure 3.20 Schematic diagram of the porous media model for airflow in the horizontal direction in a grain bed.

First, the whole grain bulk is treated as a porous medium with a nominal intrinsic permeability. From Darcy's law, the total flow rate through the porous medium is determined as (Darcy, 1856).

$$Q_h = \frac{k_h A_h}{\mu} \left(\frac{\Delta P}{L} \right)_h \quad (3.24)$$

where Q_h is the total horizontal flow rate ($m^3 s^{-1}$), k_h is the horizontal intrinsic permeability (m^2), A_h is the total horizontal cross sectional area (m^2), μ is the air viscosity ($Pa \cdot s$), ΔP is the pressure drop (Pa), and L is the length of flow path (m).

Second, the airflow rate through each cylindrical tube is considered:

$$Q_i = \frac{k_i A_i}{\mu} \left(\frac{\Delta P}{L} \right)_i \quad (3.25)$$

where Q_i is the horizontal flow rate ($m^3 s^{-1}$) through i^{th} tube, k_i is the horizontal intrinsic permeability (m^2) of the i^{th} tube, A_i is the horizontal cross sectional area (m^2) of the i^{th} tube.

Since all tubes are in parallel, the total flow rate Q_h (m^3s^{-1}) through the grain bulk is the sum of flow rates from all tubes:

$$Q_h = Q_1 + Q_2 + Q_3 \dots + Q_n \quad (3.26)$$

where $Q_{1,2,3,\dots,n}$ is the horizontal flow rate (m^3s^{-1}) through tube 1 to n

Substituting equation (3.25) into (3.26) yields:

$$\frac{k_h A_h (\Delta P)}{\mu} \left(\frac{\Delta P}{L}\right)_h = \frac{k_1 A_1 (\Delta P)}{\mu} \left(\frac{\Delta P}{L}\right)_1 + \frac{k_2 A_2 (\Delta P)}{\mu} \left(\frac{\Delta P}{L}\right)_2 + \frac{k_3 A_3 (\Delta P)}{\mu} \left(\frac{\Delta P}{L}\right)_3 \dots + \frac{k_n A_n (\Delta P)}{\mu} \left(\frac{\Delta P}{L}\right)_n \quad (3.27)$$

All tubes are subjected to the same pressure drop:

$$\left(\frac{\Delta P}{L}\right)_h = \left(\frac{\Delta P}{L}\right)_1 = \left(\frac{\Delta P}{L}\right)_2 = \left(\frac{\Delta P}{L}\right)_3 \dots = \left(\frac{\Delta P}{L}\right)_n \quad (3.28)$$

Therefore, equation (3.28) is reduced to:

$$k_h A_h = [k_1 A_1 + k_2 A_2 + k_3 A_3 \dots + k_n A_n] \quad (3.29)$$

$$k_h A_h = \sum_{i=1}^n k_i A_i; \quad A_i = \pi R_i^2; \quad A_h = \sum_{i=1}^n A_i \quad (3.30)$$

where R_i is the pore radius (m) of the i^{th} tube

Abass et al. (2011) proposed a formula to estimate the hydraulic radius in porous media from the particle diameter and porosity as follows:

$$R_h = \frac{d_p}{6} \left[\frac{\varepsilon}{1 - \varepsilon} \right] \quad (3.31)$$

where R_h is the hydraulic radius of pore (m), ε is the porosity (*fraction*), d_p is the particle diameter (m).

For a circular cross-section: $R_h = R_i/2$.

$$R_i = \frac{d_p}{3} \left[\frac{\varepsilon}{1 - \varepsilon} \right] \quad (3.32)$$

Using equation (3.29), with a porosity value of 0.4 and soybean particle diameter of $5mm$, the pore radius was estimated as $1.1mm$. This was within the range for the value of bulk grains pore radius measured with the use of X-ray CT by Neethirajan et al. 2008. To consider the effect of compaction on pore size, an empirical model developed in a previous study (Nwaizu and Zhang, 2017) was used to predict porosity as a function of grain depth:

$$\varepsilon_z = 0.41 - B(1 - e^{-\lambda z}) \quad (3.33)$$

where ε_z is the porosity at a given depth (*fraction*), z is the grain depth (m), B and α are two empirical parameters ($B = 0.35$ and $\lambda = 0.07$)

Therefore, the pore radii can be calculated for as a function of grain depth as follows:

$$R_i = \frac{d_p}{3} \left[\frac{0.41 - B(1 - e^{-\lambda z_i})}{1 - (0.41 - B(1 - e^{-\lambda z_i}))} \right] \quad (3.34)$$

z_i is the grain depth at the i^{th} layer.

The Hagen–Poiseuille law (cited by Frederick, 2010) is commonly used for describing the relationship between flow rate and pressure drop in fluid flow through long cylindrical pipes.

$$Q = \frac{\pi D^4 \Delta P}{128 \mu L} \quad (3.35)$$

where D is the pipe diameter (m).

Equation (3.32) can be re-written as:

$$Q = \frac{1}{8} R^2 \frac{A \Delta P}{\mu L} \quad (3.36)$$

Comparing equation (3.36) with equation (3.25) yields:

$$k_i = \frac{1}{8} R_i^2 \quad (3.37)$$

Now equations (3.37), (3.34), and (3.29) can be used sequentially to determine k_h , which can then be used to determine the overall pressure drop with equation (3.24) for airflow in the horizontal direction.

3.6.2 Geometrical model for predicting resistance to airflow in vertical direction

For the vertical direction, the flow channels were represented by cylindrical tubes in series, with gradually decreasing diameters from the top to the bottom to represent the effect of material compaction (fig. 3.21).

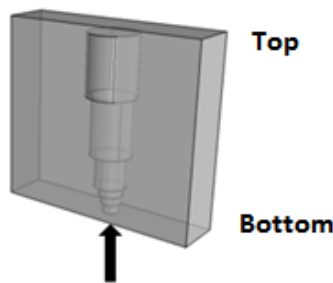


Figure 3.21 Schematic diagram of the porous media flow path model in vertical direction.

For a representative cylindrical tube i , the pressure drop is determined by Darcy's equation as follows:

$$\left(\frac{\Delta P}{L}\right)_i = \frac{Q_i \mu}{k_i A_i} \quad (3.38)$$

The total flow rate Q_v through tubes in vertical direction is the same as that through individual cylinders:

$$Q_v = Q_1 = Q_2 = Q_3 \dots \dots = Q_n \quad (3.39)$$

And the total pressure drop is determined as the sum of pressure drops through all cylinders:

$$\left(\frac{\Delta P}{L}\right)_t = \left(\frac{\Delta P}{L}\right)_1 + \left(\frac{\Delta P}{L}\right)_2 + \left(\frac{\Delta P}{L}\right)_2 \dots \dots + \left(\frac{\Delta P}{L}\right)_n \quad (3.40)$$

$$\frac{Q_v \mu}{k_v A_v} = \frac{Q_1 \mu}{k_1 A_1} + \frac{Q_2 \mu}{k_2 A_2} + \frac{Q_3 \mu}{k_3 A_3} \dots \dots + \frac{Q_n \mu}{k_n A_n} \quad (3.41)$$

$$\frac{1}{k_v A_v} = \left(\frac{1}{k_1 A_1} + \frac{1}{k_2 A_2} + \frac{1}{k_3 A_3} \dots \dots + \frac{1}{k_n A_n} \right) \quad (3.42)$$

$$\frac{1}{k_v A_v} = \sum_{i=1}^n \frac{1}{k_i A_i} \quad (3.43)$$

where Q_v is the total vertical flow rate ($m^3 s^{-1}$), k_v is the vertical intrinsic permeability (m^2), A_v is the total inlet area for the vertical flow. Pressure drops were determined as the summation of all the pressure drops through the individual flow paths estimated based on their smallest inlet area A_1 .

Substituting Intrinsic permeability k_i and the area A_i obtained from equation (3.37) and (3.30) respectively into equation (3.43), k_v can be determined. And using the determined k_v , the overall pressure drop in the vertical direction can be determined using Darcy's equation.

4 Results and Discussion

4.1 Location effect

Porosity and tortuosity were determined from sub-samples extracted from three different locations (top, middle, and bottom) at different grain pressures (simulated depths) and vibration intensities (fig. 4.1). Analysis of variance (ANOVA) was conducted to determine the effect of sub-sample locations and compaction caused by the grain depth (grain pressure) and vibration on porosity and tortuosity.

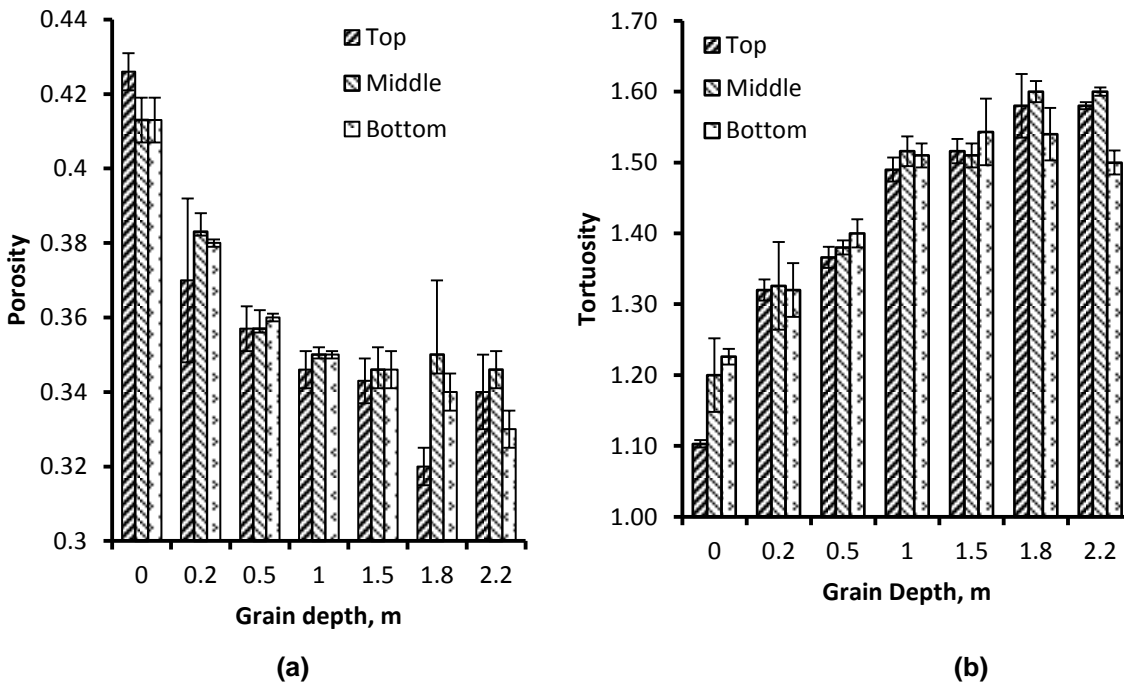


Figure 4.1 Measured porosity (a) and tortuosity (b) at different grain pressures (depths) at different sample locations (Top, Middle, and Bottom).

At 0.2 m grain depth, porosity values were quantified as 0.37 ± 0.022 , 0.38 ± 0.005 , and 0.38 ± 0.006 (standard error) and tortuosity values 1.32 ± 0.015 , 1.33 ± 0.052 , and 1.32 ± 0.011 from the sub-samples extracted from the Top, Middle and Bottom locations, respectively. At a greater grain depth 2.2 m, porosity values were quantified as 0.340 ± 0.010 , 0.346 ± 0.005 , and 0.330 ± 0.005 , and tortuosity values 1.58 ± 0.005 ,

1.60 \pm 0.005 and 1.50 \pm 0.017 from the sub-samples extracted from the Top, Middle and Bottom locations, respectively. ANOVA results (details in Appendix B) showed that the grain depth (grain pressure) significantly ($P < 0.05$) affected porosity and tortuosity, while sub-sample locations (Top, Middle, and Bottom) had no significant ($P > 0.05$) effect on porosity and tortuosity. Similarly, vibration intensity significantly ($P > 0.05$) affected both the porosity and tortuosity. There were no significant ($P > 0.05$) differences in the porosity and tortuosity among the sub-samples extracted from the top, bottom, and middle locations.

4.2 The effect of compaction on pore structure

4.2.1 Porosity variation with compaction pressure (grain depth)

Porosity decreased with the grain depth (compaction pressure) as expected (fig. 4.2). The rate of decrease in porosity was higher at the lower pressure and then gradually approached a minimum value. Without compaction, the initial porosity was determined to be 0.42, and reduced to 0.36 at a compaction pressure equivalent to 0.5 *m* of grain depth. The initial quick decrease in the porosity was mainly due to the re-arrangement of the grain particles (Thompson and Ross, 1983). It was also observed that as the grain depth increased, porosity gradually approached a minimum value of 0.34. This gradual (slow) reduction in porosity at high pressure (> 0.5 *m* grain depth) implied that changes in the pores structure was due to grain kernel breakage or deformation.

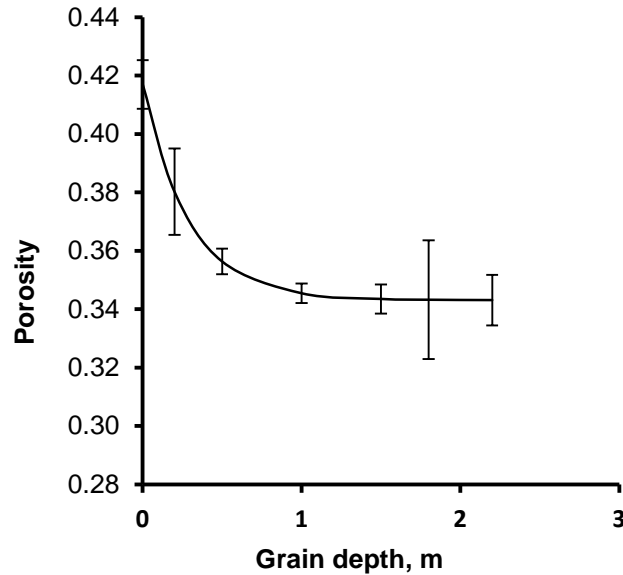


Figure 4.2 Variation in porosity with grain depth.

Similar results have been reported for other porous beds such as soil (Richard et al. 2001), cements (Barrallet et al. 2002), rocks (Olson, 1999), and packed beds (Hague et al. 2011). Barralet et al. (2002) showed a decrease in porosity from 50% to 31% with compaction pressure increased from 18 to 106 MPa in a cement bed. Richard et al. (2001) studied changes in porosity as a result of compaction on silt soil; they concluded that there was a great difference in total void ratio (porosity) between the compacted and the un-compacted silt soil. Hague et al. (2011) developed a mathematical model to determine void fraction at different depths of a granular material in a deep bed. Their results indicated that void fraction (porosity) decreased to a minimum value as the depth of the packed bed increased.

Models have been developed to predict bulk density as a function of compacting pressure (Thompson et al. 1987; Hague, 2013; Cheng et al. 2015). In this study, the following exponential model was proposed based on the experimental data to correlate porosity (ϵ) as a function of grain depth (z):

$$\varepsilon = \varepsilon_0 - B(1 - e^{-\lambda z}) \quad (4.1)$$

where ε is the predicted porosity at a given grain depth, ε_0 is the maximum porosity obtained at the surface of the grain bed (where $z = 0$); B and λ are the empirical model parameters. Using the SAS NLIN procedure, the two model parameters B and α were determined to be $B = 0.07 \pm 0.001$ and $\lambda = 0.35 \pm 0.03$. The model predictions compared well with the experimental data (fig. 4.3), with a relative error less than 5%.

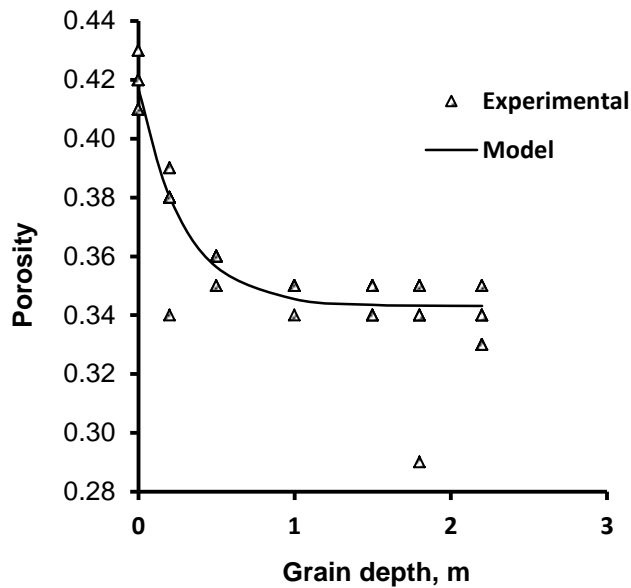


Figure 4.3 Comparison between the porosity predicted by porosity variation model based on compaction (grain depth) and experimental results.

To further validate the model, the model predictions were compared with a data set reported by Khatchatourian et al. (2004) for soybeans stored in a lab-scale polyvinyl chloride bin with a diameter of 0.2 m. The bin was contained in a wooden structural support equipped with lever-operated compacting device to apply force that could simulate up to a grain depth of 50 m. Table 4.1 (column “A”) shows the relative errors and it can be seen that predictions by the present model were in close agreement with the reported experimental data. And also, Table 4.1 (column “B”) reveals the

comparison with relative errors less than 13% between the present model and the prediction from a model proposed by Haque et al. (2011).

Table 4.1 Comparison between the predicted porosity with experimental and other model.

Grain depth (m)	Porosity			Relative error (%)	
	Experimental**	Model (Haque et al.)	Model (present study)	A	B
1	0.391	0.353	0.397	1.5 ^a	11.1 ^b
5	0.385	0.343	0.359	7.2	4.5
10	0.382	0.332	0.349	9.4	4.9
20	0.375	0.319	0.347	8.1	8.1
30	0.371	0.311	0.347	6.9	10.4

** Khatchatourian et al. (2004)

^a Relative error comparing the present model with the experimental results.

^b Relative error comparing the model by Haque et al. (2011) with the experimental results.

Compaction would change not only porosity, but also pore size and shape. Pore sizes and shapes were examined at a grain depth of 2.2 m (high compaction), and 0 m (no compaction). The pore size was quantified by the pore volume, and the sphericity value (that is, sphericity value equal to 1 means a pore with a perfect sphere shape) was used to quantify the pore shapes. Results indicated that compaction resulted in more small pores in 1 - 2 mm³ range and less large pores in the range greater than 3 mm³ (fig. 4.4). Similar experimental results were reported by Robertson and Campbell (1997).

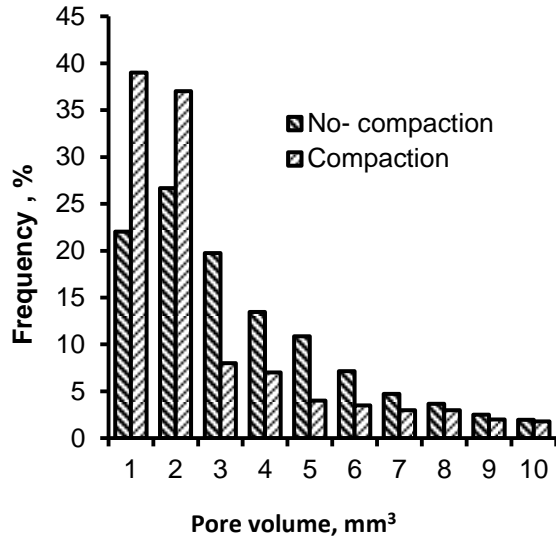


Figure 4.4 Effect of compaction on pore volume.

Also, the results indicated that compaction resulted in higher sphericity (fig. 4.5), meaning that most of the pores were closer to being spherical in shape at higher compaction pressure.

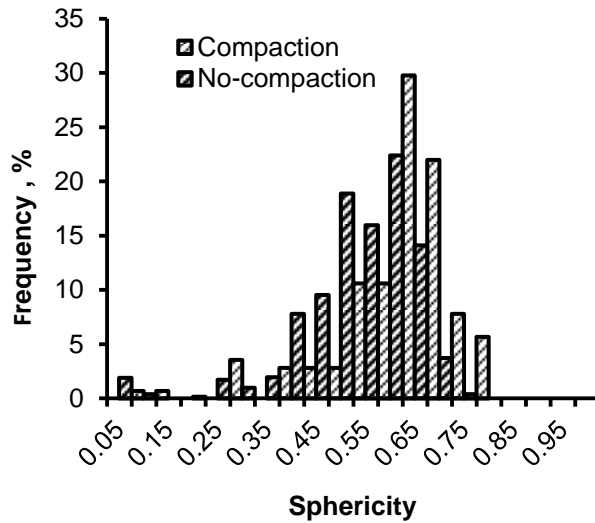


Figure 4.5 Effect of compaction on pore shape (sphericity).

4.2.2 Tortuosity variation with compaction pressure (grain depth)

Figure 4.6 illustrates that the predicted tortuosity increased with the grain depth, from 1.17 at the grain surface to 1.57 at 2.2 m, or an increase of 34%.

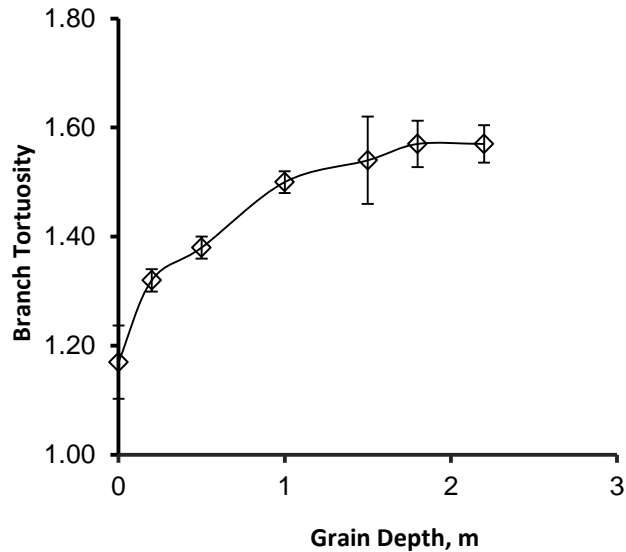


Figure 4.6 Variation in tortuosity with grain depth.

Many models have been proposed to correlate tortuosity to porosity. Based on the model proposed by Yun et al. (2005), tortuosity was correlated to the grain depth as follows:

$$\tau = a - b \ln(\varepsilon) \quad (4.2)$$

where τ is the tortuosity, ε is the porosity, a and b are empirical model parameters

Substituting equation 4.1 into 4.2 yields:

$$\tau = a - b \ln[\varepsilon_0 - B(1 - e^{-\lambda z})] \quad (4.3)$$

The SAS statistical NLIN procedure was conducted to determine the values for the two model parameters, a and b . Parameter a was estimated as 0.95 ± 0.05 and parameter b 0.36 ± 0.03 . The details of NLIN procedure output are shown in Appendix B.

Model predictions compared well with the experimental data with relative errors less than 5 % (fig. 4.7).

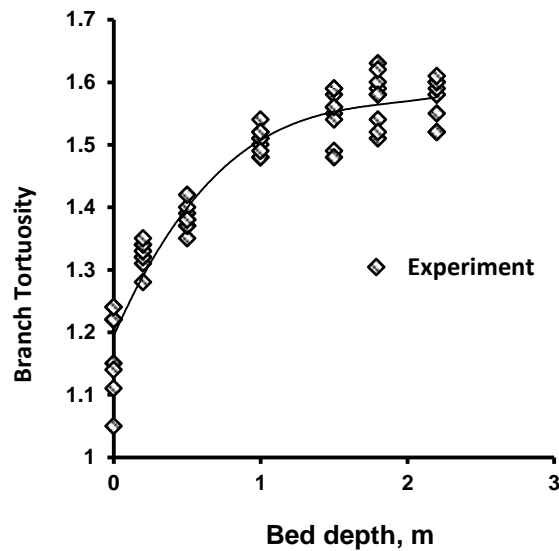


Figure 4.7 Comparison between the tortuosity predicted by the proposed model based on compaction and experimental data.

4.3 The effect of vibration on pore structure

4.3.1 Porosity variation due to vibration

It has been established that vibration causes increase in bulk density of porous media (James et al., 1985; Hao et al., 1994; Ge et al. 2000; Xiao et al., 2008; An et al., 2009; An et al., 2011). Ge et al. (2000) developed a mathematical model to predict grain consolidation as a result of vibration and explained that vibration induced compaction because of the “wedge-in” mechanism which was described as the downward movement of upper laying particles “wedging” into the lower layer particles to create a consolidated layer during vibration.

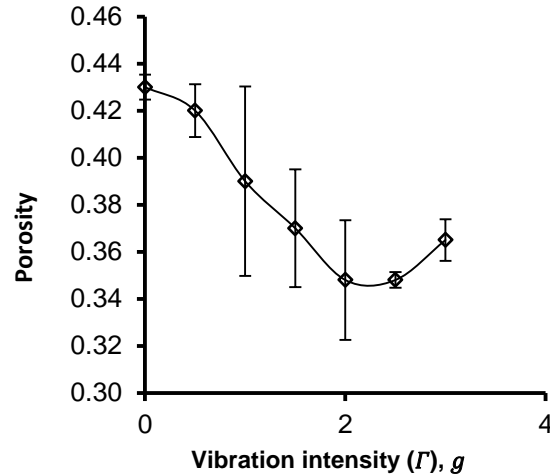


Figure 4.8 Variation in porosity with vibration intensity.

It was observed in this study that porosity initially decreased with increase in vibration intensity Γ to a minimum value and thereafter started to increase (fig. 4.8). Porosity reached a minimum value of 0.34 at around vibration intensity $\Gamma = 2.5g$, and further increase in vibration intensity caused a gradual increase in porosity. Many researchers explained the reduction in porosity by vibration as a result of external energy that breaks the loose inter-particle arrangement of the grain kernels to a denser packing state which consequently caused the reduction in porosity (An et al., 2011; Zhang and Rosato, 2006; Yue and Zhang, 2016). However, An et al. (2005) observed that vibration caused increases in porosity. Also, Xiao et al. (2008) studied changes in pore structure during vibration and observed that porosity increased during vibration. Vibration caused rearrangement of grain kernels into a denser packing at low vibration intensity ($<2g$), but high intensity vibration over-excited the grain kernels to the extent that the dense packing was broken into loose packing, which consequently resulted into a gradual increase in porosity (An et al., 2009, Yue and Zhang, 2016).

Based on the observed pattern of variation in porosity shown in figure 4.8, the following equation was proposed to describe the relationship between porosity and vibration intensity.

$$\varepsilon_{\Gamma} = \varepsilon_o - A(\sin\beta\Gamma) \quad (4.4)$$

Where ε_{Γ} is the porosity after vibration, ε_o is the initial porosity (before vibration), Γ is the vibration intensity (g), A and β are the empirical model parameters.

The SAS NLIN procedure was conducted to determine the values for the two model parameters, A and β ; A was estimated to be 0.08 ± 0.004 and β was estimated 0.63 ± 0.069 (the NLIN procedure output is shown in Appendix B).

The model provided a reasonably good prediction when compared with the experiment data with relative errors less than 5 % (Table 4.2, column “A”) (fig. 4.9).

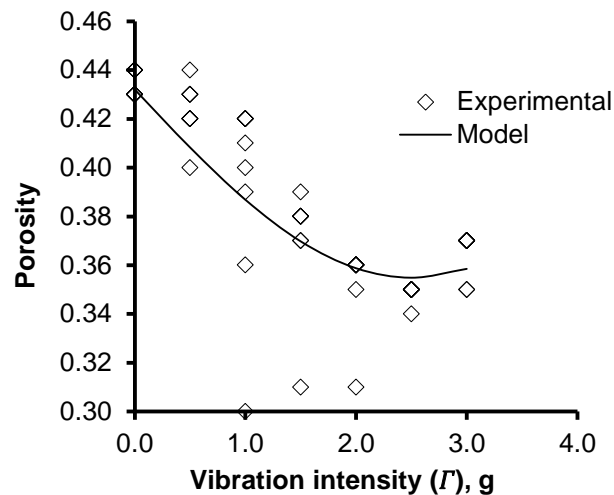


Figure 4.9 Comparison between the porosity predicted by porosity variation model based on vibration and experimental results.

The model prediction was also compared with the DEM simulations reported by Yue and Zhang, 2016 (Table 4.2, column “B”) and good agreement was observed.

Table 4.2 Comparison between the predicted porosity with experimental and other model.

Vibration intensity, (Γ)g	Porosity			Relative error (%)	
	Experiment	Model (Yue & Zhang)	Model (present study)	A	B
0.0	0.434	0.409	0.432	0.5	5.6
0.5	0.423	0.395	0.408	3.7	3.3
1.0	0.393	0.390	0.386	1.8	1.0
1.5	0.370	0.380	0.369	0.3	2.9
2.0	0.348	0.375	0.358	2.8	4.5
2.5	0.340	0.382	0.354	4.0	7.3
3.0	0.365	0.385	0.358	2.0	7.0

^A Relative error comparing the present model with the experimental results.

^B Relative error comparing the model by Yue and Zhang (2011) with the experimental results.

4.3.2 Tortuosity variation due to vibration

Figure 4.10 shows the effect of vibration on tortuosity. As the vibration intensity increased from 0 to 2g, tortuosity increased to a maximum value of 1.39, and further increase in vibration intensity caused reduction in tortuosity. This pattern of variation in tortuosity was a mirror image (reverse) of that of porosity. Studies have shown that vibration caused large pores to decrease in size, creating more pores of smaller sizes (Xiao et al., 2008; An et al., 2008), and consequently greater tortuosity. Nwaizu and Zhang (2015) used an imaging technique with smoke to visualize airflow paths through bulk grain subjected to vibration and observed that reduction in porosity after vibration caused “lateral branching” of the vertical air flow through a grain bed. The observed “lateral branching” was an indication of greater tortuosity (more air flowed sideways instead of upwards through the grain bed). Further increase in vibration intensity $\Gamma > 2g$ caused a gradual reduction in tortuosity due to increase in porosity as higher vibration energy loosened the grain packing.

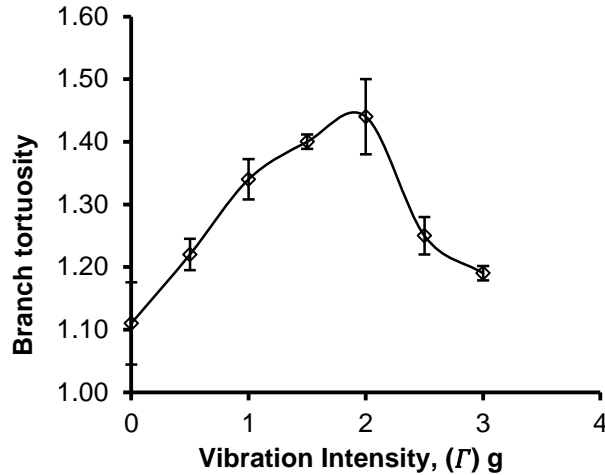


Figure 4.10 Variation in porosity with vibration intensity.

Based on the observed pattern of variation in tortuosity, the following empirical model was proposed to describe the relationship between tortuosity and vibration intensity:

$$\tau_{\Gamma} = a + b\Gamma - c\Gamma^2 \quad (4.5)$$

Where τ_{Γ} the tortuosity after vibration, Γ is the vibration intensity, a , b and c are the empirical model parameters

Using the SAS NLIN procedure the values of three parameters, a , b and c were estimated to be $a = 1.05 \pm 0.05$, $b = 0.62 \pm 0.07$, and $c = 0.14 \pm 0.02$ (the NLIN procedure output is shown in Appendix B).

The model well represented the experimental data (relative differences between the model and the data were less than 5 %) (fig. 4.11).

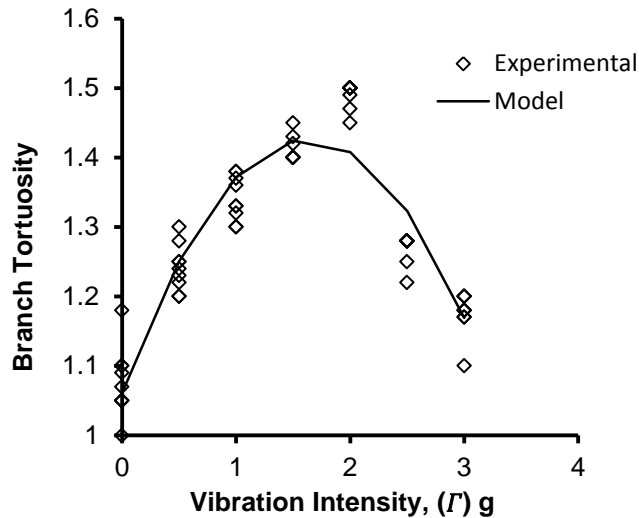


Figure 4.11 Comparison between the tortuosity predicted by tortuosity variability model based on vibration and experimental results.

4.4 The effect of vibration on pore structure

4.4.1 Validation of the CFD simulation models

Validation of the static pressure distribution was carried out using data reported in the literature by Khatchatourian et al. (2004) obtained from an experimental study on soybeans of moisture content of 13% and impurity of 2% stored in a lab-scale polyvinyl chloride bin with a diameter of 0.2 m. The bin was supported in a wooden structure equipped with a lever-operated compacting device, which could apply forces to simulate up to 50 m depth of grain. A centrifugal fan was used to supply airflow through the perforated bottom of the bin to the soybean grain bed. The changes in porosity were measured as a function of the grain depth. Static pressure drops values were measured through the compacted soybean grain bed at five different airflow velocities (0.1, 0.2, 0.3, 0.4 and 0.5 ms^{-1}) through a grain layer 1 m thick. Although the unique contribution of this study was to include the compaction effect (variations of pore structure, i.e., porosity and tortuosity) in CFD simulations, simulations for non-compaction (the

constant pore structure, porosity $\varepsilon = 0.41$ and tortuosity $\tau = 1.10$) was carried out for comparison. Furthermore, the ASABE Standard (ASAE R2011.D272.3, 2011) was used as a reference.

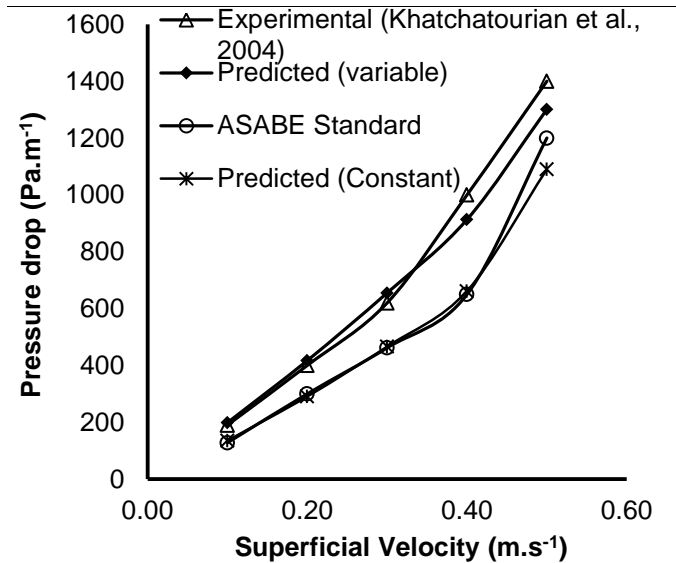


Figure 4.12 Comparison of CFD model simulations with ASABE Standard and experimental data reported in the literature.

For both the constant and variable pore structure simulations, pressure drop increased with the superficial velocity as expected (fig. 4.12). However, the simulated pressure drop for the variable pore structure (with compaction) was higher than that for the constant pore structure (without compaction) (fig. 4.12). As velocity increased from 0.1 to 0.5 ms^{-1} , the pressure drop increased from 198.7 to 1301.0 Pam^{-1} and from 135.3 to 1090.0 Pam^{-1} for the variable and constant pore structure simulations, respectively. This meant that the simulated static pressure drop for compaction was about 31.9% higher than that for non-compaction at airflow velocity of 0.1 $m s^{-1}$, and 16.2% higher at 0.5 $m s^{-1}$.

The relative differences in pressure drop between the experimental data and simulated values for compaction ranged from 4.1% to 9.5% (Table 4.3, column “A”), whereas the

differences between the experimental data and the simulated values without considering compaction ranged from 28.1% to 51.8% (Table 4.3, column “B”). This indicated that the model simulations including the compaction effect were in close agreement with the reported experimental data, whereas the simulated pressure drops without considering compaction were lower than in comparison with the experimental data.

Table 4.3 Relative errors between experimental value and values predicted by the variable and constant pore structure simulations.

Airflow(m/s)	Static Pressure (Pa.m ⁻¹)			Relative Error (%)	
	Experimental	Predicted (variable)	Predicted (constant)	A	B
0.1	190.0	198.7	135.3	4.4	40.4
0.2	400.0	417.1	290.7	4.1	37.6
0.3	620.0	655.3	466.3	5.4	33.0
0.4	1000.0	913.3	662.0	9.5	51.1
0.5	1400.0	1301.0	1090.0	7.6	28.4

^A Relative error comparing the predicted (variable) model with the experimental results.

^B Relative error comparing the predicted (constant) model with the experimental results.

In contrast, the simulated pressure drops without considering compaction (constant pore structure) were closer to the values by the ASABE Standard than those simulated with compaction effect (fig. 4.12). Specifically, the relative differences were below 10 % (Table 4.4, column “B”) and more than 35 % (Table 4.4, column “A”) for the simulations without and with compaction effect, respectively. This observation was consistent with the fact that pressure drop values from the ASABE Standard were based on non-compacted, homogenous grain bed.

Table 4.4 Relative errors between ASABE standard and values predicted by the variable and constant pore structure simulations.

Airflow(ms^{-1})	Static Pressure (Pam^{-1})			Relative Error (%)	
	ASABE	Predicted(variable)	Predicted(constant)	A	B
0.1	128.0	198.7	135.3	35.6	5.4
0.2	300.0	417.1	290.7	28.1	3.2
0.3	462.0	655.3	466.3	29.5	0.9
0.4	650.0	913.3	662.0	28.8	1.8
0.5	1200.0	1301.0	1090.0	7.8	10.1

^A Relative error comparing the predicted (constant) model with the ASABE results.

^B Relative error comparing the predicted (variable) model with the ASABE results.

4.4.2 Simulating the effect of compaction on airflow

CFD simulations were further conducted for both constant and variable pore structures (porosity and tortuosity) in a large cylindrical flat bottom bin with a diameter of 8 m filled with soybeans grain to a eave height of 7 m and peak height of 3 m at 31° angle of repose for soybeans (Onu et al., 2016) to investigate the effect of compaction on the airflow pattern and resistance to airflow occurring in actual grain storage bins.

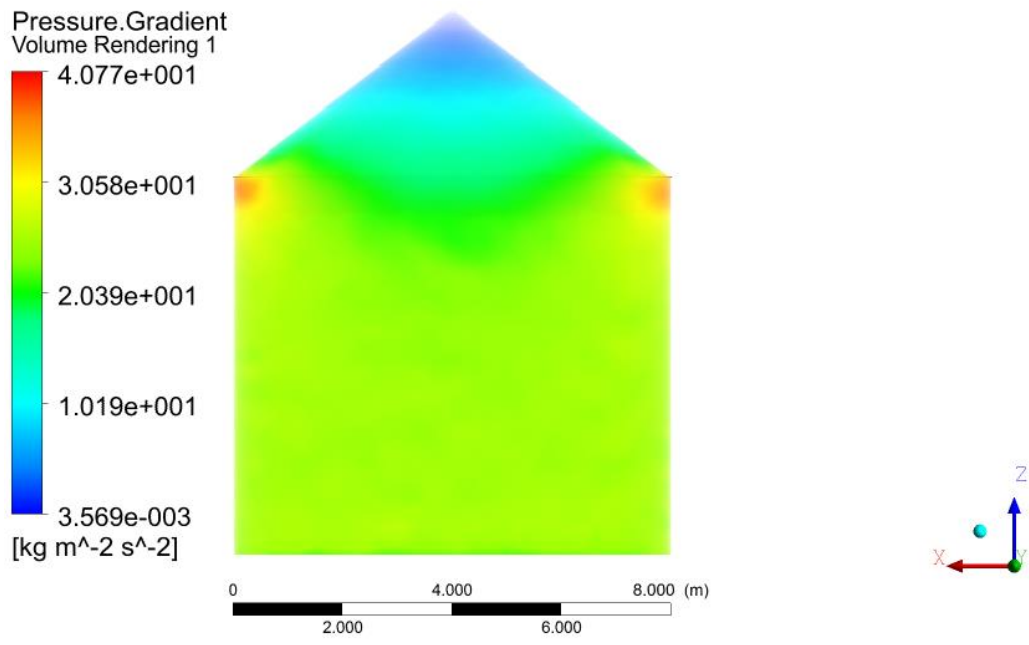
For the variable pore structure simulation, the porosity and tortuosity variation along the depth of the grain caused by compaction effect due to the grain pressure were incorporated into the CFD Fluent simulations by using the developed equations (4.1) & (4.2) for predicting porosity and tortuosity, respectively. The porosity was predicted to be 0.42 at grain depth $z = 0 \text{ m}$ (top) and 0.34 at the bottom of the grain bed ($z = 10 \text{ m}$). The tortuosity was predicted to be 1.14 and 1.48 for the top and bottom of the grain bed, respectively. In simulating the constant pore structure, porosity and tortuosity were chosen to be constant values of 0.41 and 1.10, respectively.

The total volume of soybean grain to fill the 8 m diameter cylindrical grain bin to a depth of 10 m was 294 tons, for which the total airflow was estimated to be $0.50 \text{ m}^3 \text{ s}^{-1}$, based

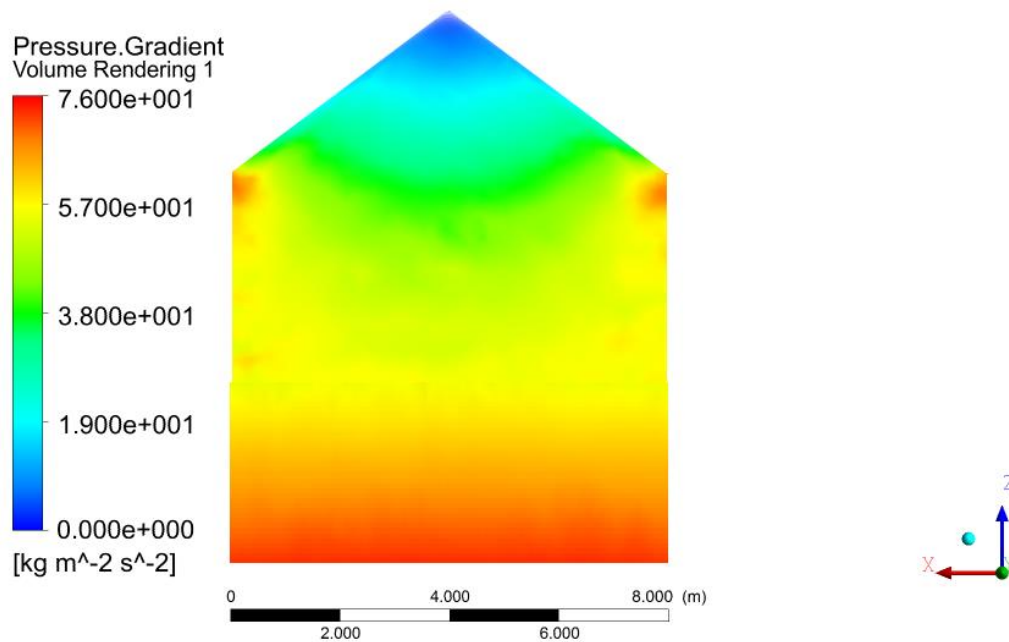
on the designed flow rate of $0.0017 \text{ m}^3\text{s}^{-1}\text{t}^{-1}$ that was sufficient to supply inlet airflow velocity of 0.01 ms^{-1} (Navarro and Noyes., 2002).

Figure 4.13 shows the simulated pressure drop distribution for the constant and variable pore structure beds. It was generally observed that the pressure drop was more uniform for the constant pore structure simulation (fig. 4.13a) in comparison with the variable pore structure simulation (fig. 4.13b). For the variable pore structure bed, higher pressure drop occurred at the bottom region of the grain bed. At $z = 10 \text{ m}$ the predicted pressure drop was 75 Pa.m^{-1} , and it then decreased progressively to 72 Pa.m^{-1} at $z = 9 \text{ m}$, and 35 Pa.m^{-1} at $z = 4 \text{ m}$ through the core of the grain mass (fig.4.13b). It was observed that pressure drop decreased at a slower rate through the grain under the peak than the grain near the wall from the bottom of the bin towards the grain surface. Similar results were reported by Bartosik and Maier (2006) that resistance to airflow (pressure drop) increased with the grain depth, with the bottom of the grain bed posing the largest resistance to airflow. For the constant pore structure bed, pressure drop predicted at the inlet was 20.4 Pa.m^{-1} . And within the core of the grain mass pressure drop was fairly uniform. The pressure drop close to the bottom of the grain bed was predicted as 19.9 Pa.m^{-1} , which was much lower than that from the variable pore structure simulation (75 Pa.m^{-1}). This observation of higher pressure drop in the lower part of the grain bed for the variable pore structure simulation was a result of the reduction in size of the flow channel due to compaction by self-weight of grain that caused reduction in porosity and more tortuous flow. This further suggests that the constant pore structure bed was not a true representation of the events occurring within large grain storage systems. In both cases, there were lower pressures per unit length

regions at the grain peaks. From figure 4.13 at 3 m height, variations in pressure drop values between the central region directly under the grain peak and regions near the wall were from $23 Pa.m^{-1}$ to $38 Pa.m^{-1}$, for the constant pore structure bed and $32 Pa.m^{-1}$ to $73 Pa.m^{-1}$ for the variable pore structure bed, respectively. This means that more air flow towards the region near the walls because of the flow paths towards the grain peak that air require to navigate before getting to the surface of the grain are much longer compare to the shorter flow paths towards the grain surface-wall boundaries. And since air followed the path of least resistance, more air tends to flow sideways towards the grain surface-wall boundaries. As a result, air pressure per unit length in the peaked grain mass decreases as air approaches the cone tip.



(a)

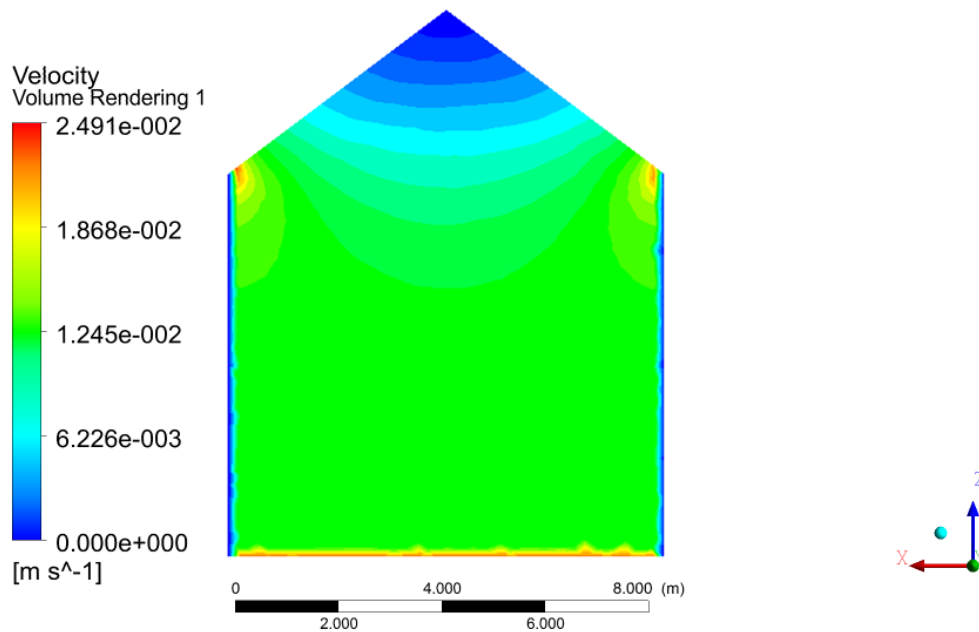


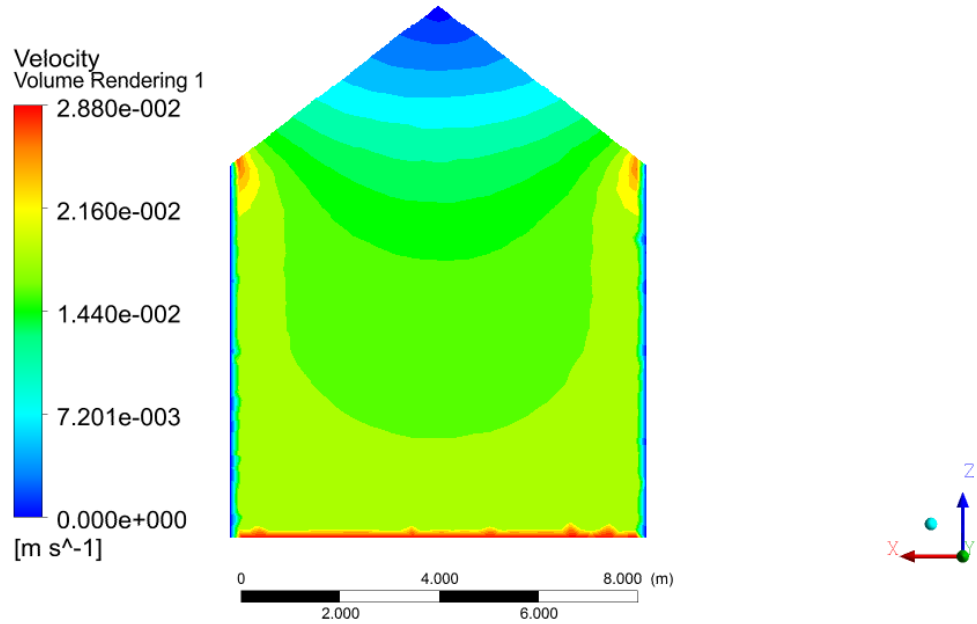
(b)

Figure 4.13 Simulated pressure drop distribution within the soybean bed at air inlet velocity of 0.01 ms^{-1} (a) without compaction, (b) with compaction.

Air velocity distributions for the constant and variable pore structure beds are illustrated in figure 4.14. The simulated air velocity varied more within the grain bed for the variable pore structure bed than that for the constant pore structure bed. For the variable bed, air was flowing into the grain bed through the inlet located at ($z = 10$) at a very high velocity of 0.028 ms^{-1} and started to decrease progressively to 0.0023 ms^{-1} at $z = 9 \text{ m}$, and 0.014 ms^{-1} at $z = 4 \text{ m}$ and then close to zero at the grain peak. It can be observed that airflow velocity within the grain core under the peak was lower compared to the faster air flowing through the periphery of the grain mass. This is because of the longer airflow paths towards the grain peak. The higher velocity at the bin bottom was attributed to compaction, which resulted in lower porosity and higher tortuosity at this region. For the constant pore structure bed, airflow velocity at the bin

bottom was around 0.024m s^{-1} , which was lower than that for the variable pore structure bed. And within the core of the grain mass, airflow velocity was fairly uniform. For example, the air velocity at $z = 9\text{ m}$ and $z = 4\text{ m}$ were predicted as 0.021 m s^{-1} and 0.019 m s^{-1} respectively, or 5.2 % in difference. In both cases, higher airflow velocities were observed at the headspace close to the wall boundaries and this is because of the lower air flow velocity flowing towards the grain peak, therefore air flow velocity has to increase around corner of the grain surface close to the wall in order to maintain energy balance based on Bernoulli's principle (law of conservation of energy). The lower air velocity at the peak region predicted for the variable and constant pore structure beds would increase transverse time (the time require to effectively dried or cool the grain mass) and consequently might leads to the problem of over drying other parts of the grain mass where air flow velocity are much higher or create a perfect condition for grain deterioration (Neyo and Navarro, 2002)





(b)

Figure 4.14 Simulated airflow velocity distribution for the soybeans bed at air inlet superficial velocity of 0.01 m s^{-1} (a) without compaction, (b) with compaction.

4.4.3 Simulating different grain aeration systems

4.4.3.1 Effect of bin floor configurations on airflow and pressure drop distribution

Different bin floor configurations have been used for drying or aeration purposes, ranging from fully perforated floor configurations to various partially perforated floors where only a portion (typically 50% to 60%) of the total floor area is perforated for air to enter the bin. Generally, the most popular floor configuration currently in use are the fully perforated floor configurations because they are easier to install and offer lesser resistance to airflow than partially perforated floor configurations. However, with low airflow requirements for aeration applications, fully perforated floor configuration systems might not be needed to save installation cost as well as optimize operations (Moses et al., 2014). Partially perforated floor configurations provide relatively low

volume of airflow and can be efficiently designed to suite the airflow requirement for aeration. But if not designed properly, partially perforated floors may result in non-uniform airflow distribution that consequently would require large capacity fans at a high cost and would take more time to aerate the grain.

CFD simulations were conducted based on the variable pore structure model to investigate static pressure and airflow velocity distributions for three commonly used partially perforated floor configurations, namely, rectangular, cross and circular perforations, with all three having the same perforated area. The total volume of soybean grain to fill the 8 m diameter grain bin to a depth of 10 m was 294 tons and the total airflow was of $0.50 \text{ m}^3\text{s}^{-1}$, based on the designed flow rate of $0.0017 \text{ m}^3\text{s}^{-1}\text{t}^{-1}$ to achieve the inlet airflow velocity of 0.025 ms^{-1} .

The simulated static pressure distributions for the rectangular and circular partial perforated floor appeared similar, whereas, the cross perforation had a different distribution pattern (fig. 4.15). Specifically, for all three configurations, there was a high pressure zone at the inlet, but this zone was smaller for the cross perforation than the other two configurations. The highest static pressure were predicted to be 57.5 Pa at $z = 10 \text{ m}$ for the rectangular and circular perforations, and 61 Pa for the cross perforation.

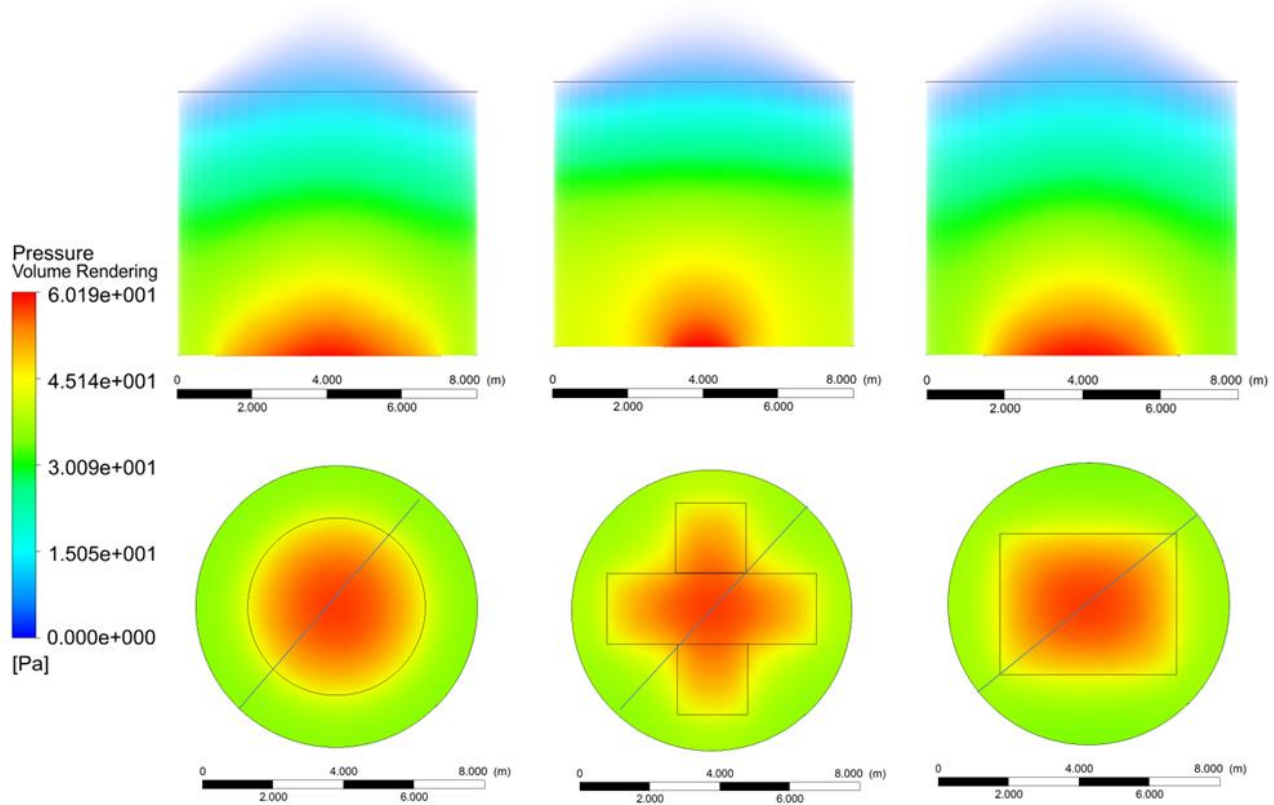


Figure 4.15 Simulated pressure distribution for soybean bed at air inlet superficial velocity of 0.025 ms^{-1} for circular, cross and rectangular partial perforated floor configurations.

Outside the high pressure zone, static pressure decreased uniformly towards the grain surface. The static pressure was more uniform away from the center of the bin towards the wall boundaries for the cross perforation than the other two configurations. For example, the pressure at $z = 10 \text{ m}$ was 61 Pa at the center of the bin and 59.2 Pa at the wall. In comparison, the pressure at $z = 10 \text{ m}$ was 57.5 Pa and 30 Pa at the centre of the bin and the wall, respectively. However, this difference or non-uniformity in static pressure in the radial direction disappeared in the upper portion of the bin.

From the figure 4.16, it is evident that low velocity regions occurred close to the bottom of the grain bed at the wall for all three floor configurations. Moses et al. (2014) suggested

that increasing the perforation area could improve the uniformity in airflow velocity distribution close the bottom of the grain bed for partial perforated floor configurations. Generally speaking, the cross perforation gave the best uniformity of airflow velocity distribution, but the average air velocity was lower than that for the other two configurations (0.0067ms^{-1} vs. 0.013ms^{-1}) through the core of the grain mass, and thus it would require longer time and higher operational expense to dry or cool grain using the cross perforation.

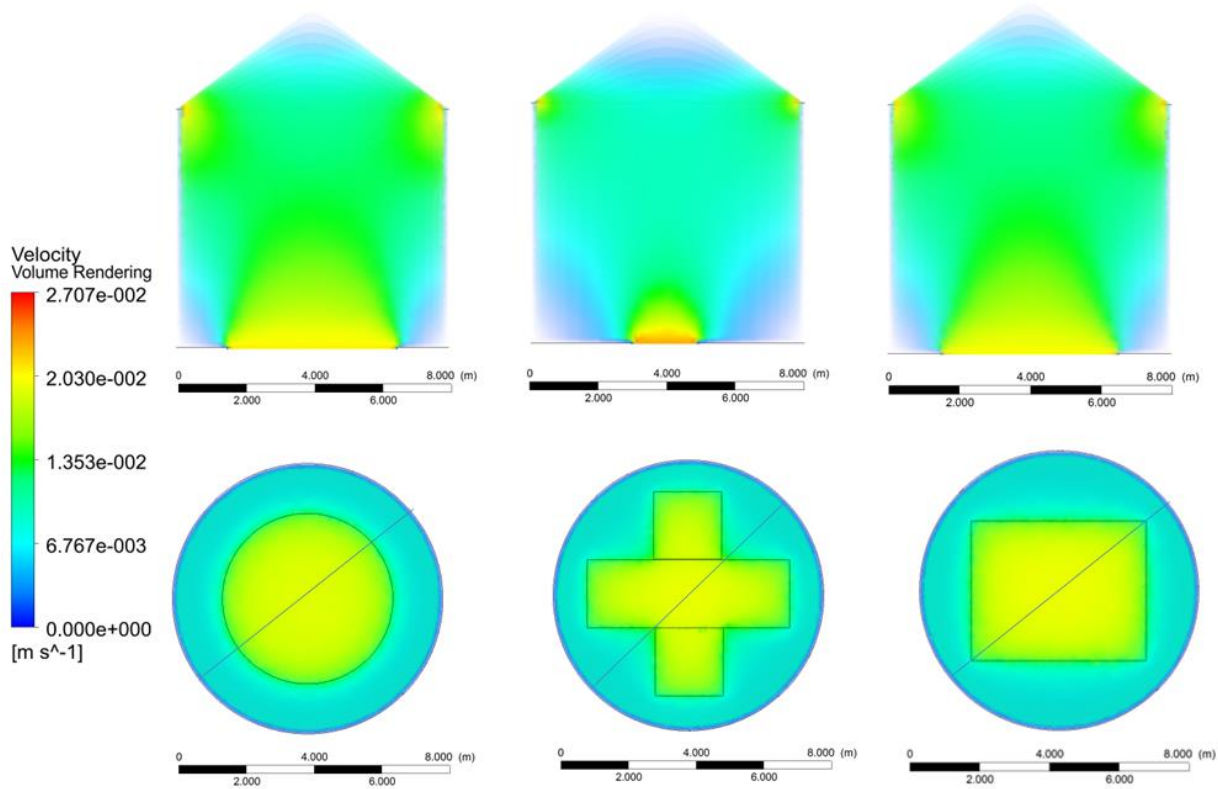


Figure 4.16 Simulated airflow velocity distribution for the soybeans bed at air inlet superficial velocity of 0.025ms^{-1} for circular, cross and rectangular partial perforated floor configurations.

4.4.3.2 Effect of aspect ratio (H:D) on airflow and pressure drop distribution

Simulations were conducted based on the variable pore structure to study airflow velocity and pressure drop for fully perforated floor cylindrical bins with different bin height (H) to diameter (D) ratio (aspect ratio), H:D= 0.75, 1.00 and 1.50. These are typical aspect ratios in commercial grain storage bins.

The total amounts of soybean grain to fill the bins were 172, 220, and 367 tons for aspect ratios of 0.75, 1.00 and 1.50, respectively. The corresponding airflow rates were $0.29 \text{ m}^3 \text{ s}^{-1}$, $0.37 \text{ m}^3 \text{ s}^{-1}$ and $0.62 \text{ m}^3 \text{ s}^{-1}$, based on the designed flow rate of $0.0017 \text{ m}^3 \text{ s}^{-1} \text{ t}^{-1}$ for the three aspect ratios. These airflow rates produced the inlet air velocities of 0.005 m s^{-1} , 0.007 m s^{-1} , and 0.01 m s^{-1} , respectively, to simulate the typical aeration condition.

As expected, the higher the aspect ratio, the greater the pressure drop in the lower portion of the bin as well as within the core of the grain mass. For H:D= 1.50, pressure drop was predicted as $92 \text{ Pa} \cdot \text{m}^{-1}$ at the bottom of the grain bed close to the inlet ($z = 12 \text{ m}$) and this was 63% and 45.7% greater than the pressure drops for H:D= 0.75 and H:D= 1.00, respectively. Greater variation in pressure drop occurred within the core of the grain mass inside the bin for the higher aspect ratio. Specifically, the predicted pressure drop within the core of the grain mass ranged from 87 to $38 \text{ Pa} \cdot \text{m}^{-1}$ between the grain depth 11 m and 4 m for H:D=1.50, or about 56.3% variation in pressure drop. The corresponding pressure drop ranged from 47 to $24 \text{ Pa} \cdot \text{m}^{-1}$ between the grain depth 7 m and 4 m, or 48.9% for H:D= 1.00, and from 13 to $11 \text{ Pa} \cdot \text{m}^{-1}$ between $z = 5 \text{ m}$ and $z = 3 \text{ m}$, or 15.4% for H:D= 0.75. (Figs 4.17, 4.18 & 4.19)

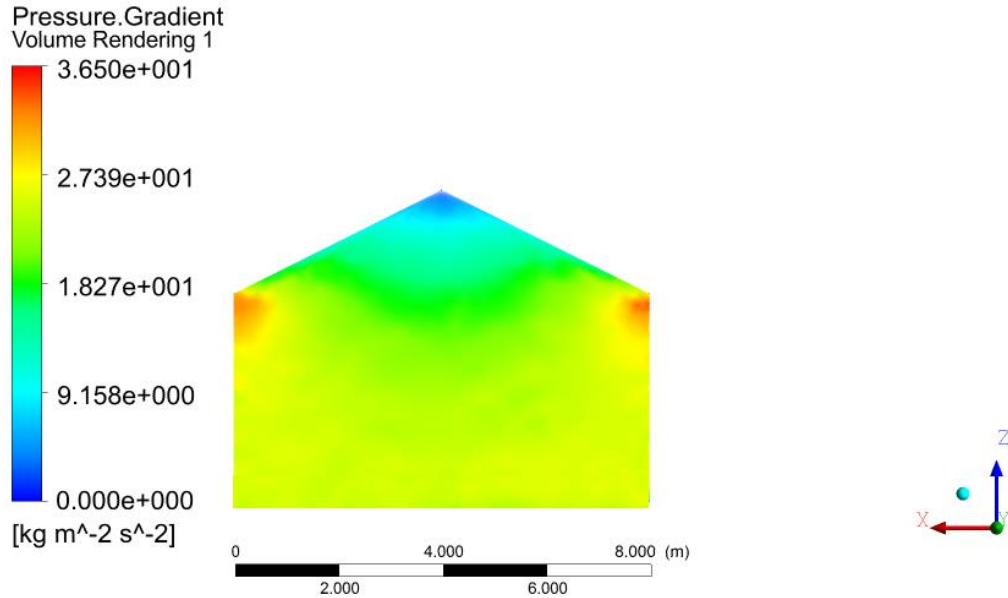


Figure 4.17 Simulated pressure drop distribution for the soybeans bed at air inlet superficial velocity of 0.005 m s^{-1} (based on design flow rate of $0.0017 \text{ m}^3 \text{ s}^{-1} \text{ t}^{-1}$) for cylindrical bin with H:D = 0.75.

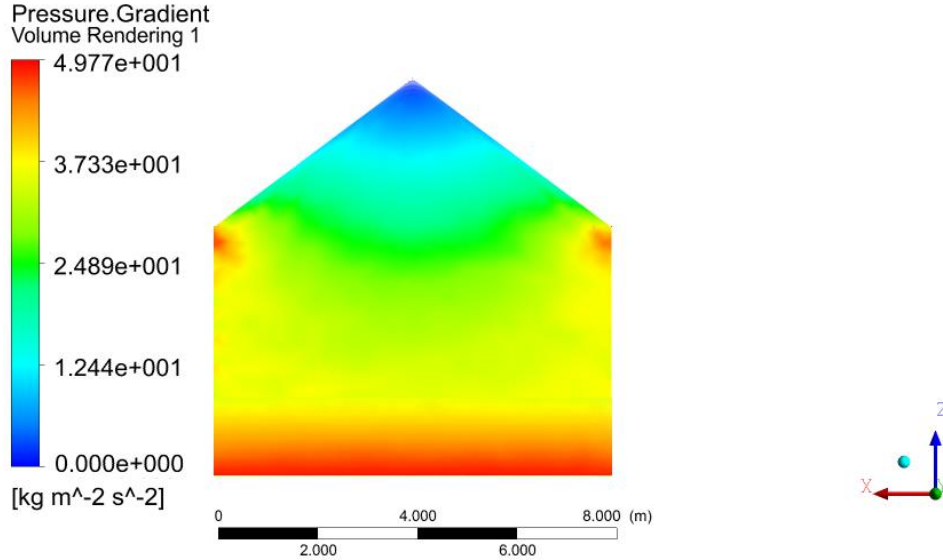


Figure 4.18 Simulated pressure drop distribution for the soybeans bed at air inlet superficial velocity of 0.007 m s^{-1} (based on design flow rate of $0.0017 \text{ m}^3 \text{ s}^{-1} \text{ t}^{-1}$) for cylindrical bin with H:D = 1.00.

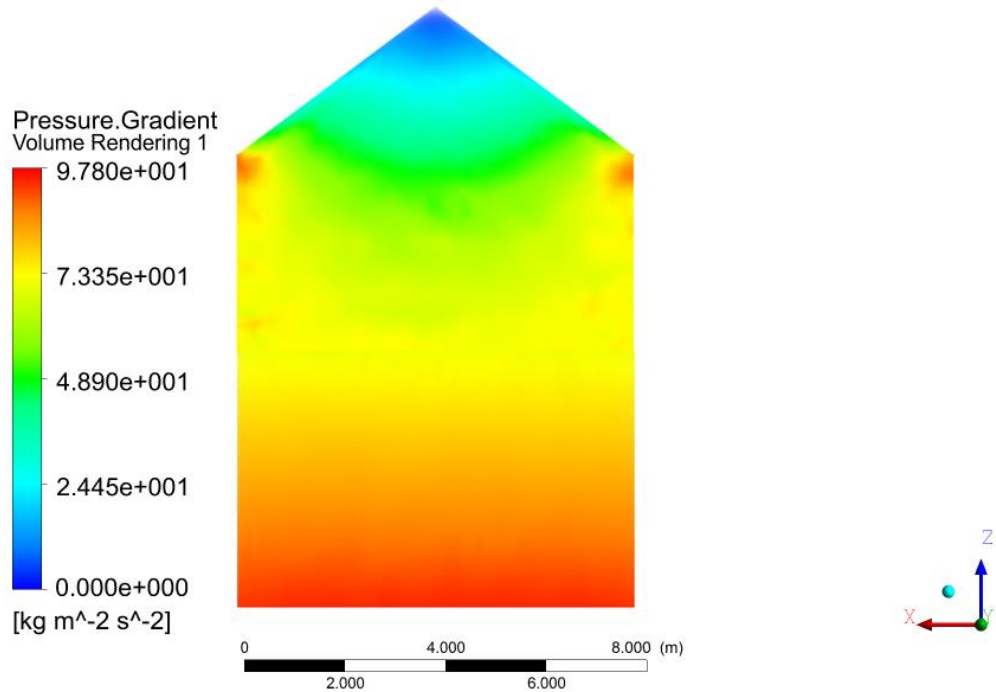


Figure 4.19 Simulated pressure drop distribution for the soybeans bed at air inlet superficial velocity of 0.01 ms^{-1} (based on design flow rate of $0.0017 \text{ m}^3 \text{ s}^{-1} \text{ t}^{-1}$) for cylindrical bin with H:D =1.50.

As expected, slower airflow velocities were observed at the grain peak than any other parts of the grain mass for all the three bins (figs 4.20, 4.21 & 4.22). And for all aspect ratios, distinct higher velocity zone rights above the bin floor were visible. This indicated higher air flow initially at the bottom of the grain beds close to the inlet due to smaller pores near the bin bottom that resulted in higher pressure drop at this location.

As the air flow progressively through the grain, the velocity magnitude reduced because of the increase in porosity and lower tortuosity which resulted into lower pressure drop as the grain depth reduces.

For the H:D =1.50, airflow velocity varied from 0.029 ms^{-1} at the bottom close to the inlet to 0.014 ms^{-1} at $z = 4 \text{ m}$ which was about 20.6 % and 28.5 % higher than airflow velocity variation that occurred in the storage bin with H:D =1.00 predicted as 0.023

ms^{-1} at the bottom to $0.010 ms^{-1}$ at $z = 4 m$, respectively. However, there were no observed change in airflow velocity within the core of the grain mass filled into bin with $H:D = 0.75$ from the bottom to the depth at $z = 4 m$. This is because the bin was shallow (lesser depth) and had minimum compaction effect due to grain depth.

At the corners of the grain surface close the wall boundaries, the airflow velocity magnitude for the bin with higher aspect ratio ($H:D=1.50$) was 24.1 % and 48.2 % greater than the airflow velocity that occurred at the corner of the grain surface close to the wall boundary for the bin with $H:D = 1.00$ and $H:D = 0.75$, respectively. This further supported the statement that increasing grain depth would increase non-uniformity in airflow in the storage bins (Khatchatourian and Savicki, 2004). That is, higher aspect ratio ($H:D$) caused heavy non-uniformity in the airflow distribution which consequently would require higher airflow rates and operation time for efficient aeration. Grain storage bins filled up to a large grain depth would be subjected to poor airflow distribution due to compaction by the grain self-weight. Storage bin aspect ratio should be thoroughly considered during grain storage bin design and installation in order to develop a more efficient aeration system

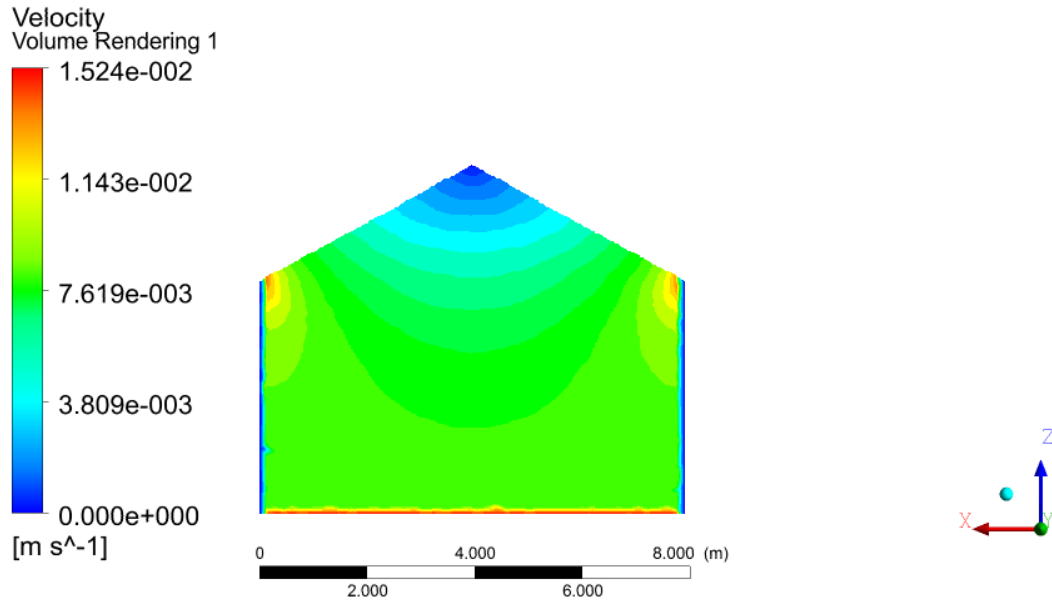


Figure 4.20 Simulated airflow velocity distribution for the soybeans bed at air inlet superficial velocity of 0.05 m s^{-1} (based on design flow rate of $0.0017 \text{ m}^3 \text{ s}^{-1} \text{ t}^{-1}$) for cylindrical bin with H:D = 0.75.

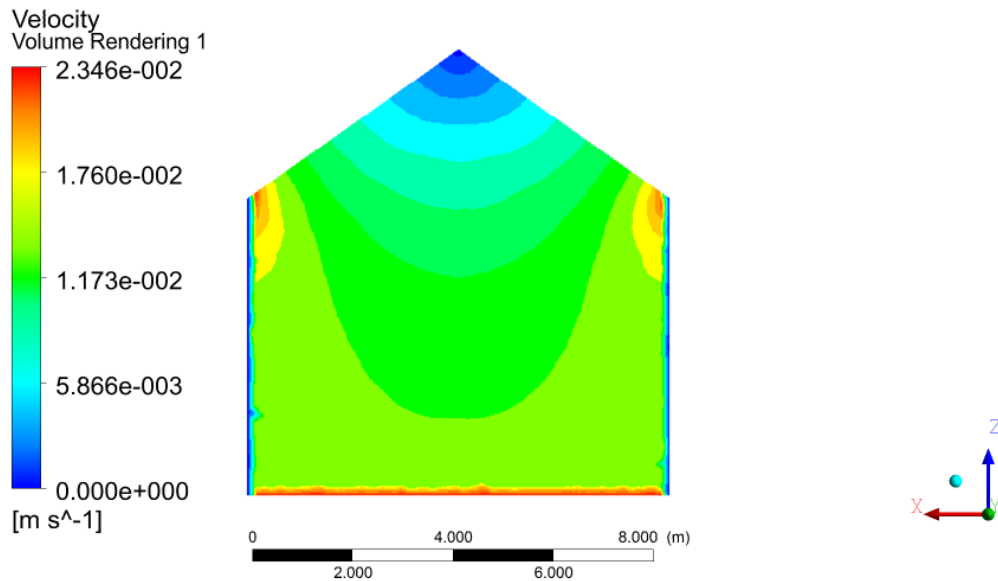


Figure 4.21 Simulated airflow velocity distribution for the soybeans bed at air inlet superficial velocity of 0.07 m s^{-1} (based on design flow rate of $0.0017 \text{ m}^3 \text{ s}^{-1} \text{ t}^{-1}$) for cylindrical bin with H:D = 1.00.

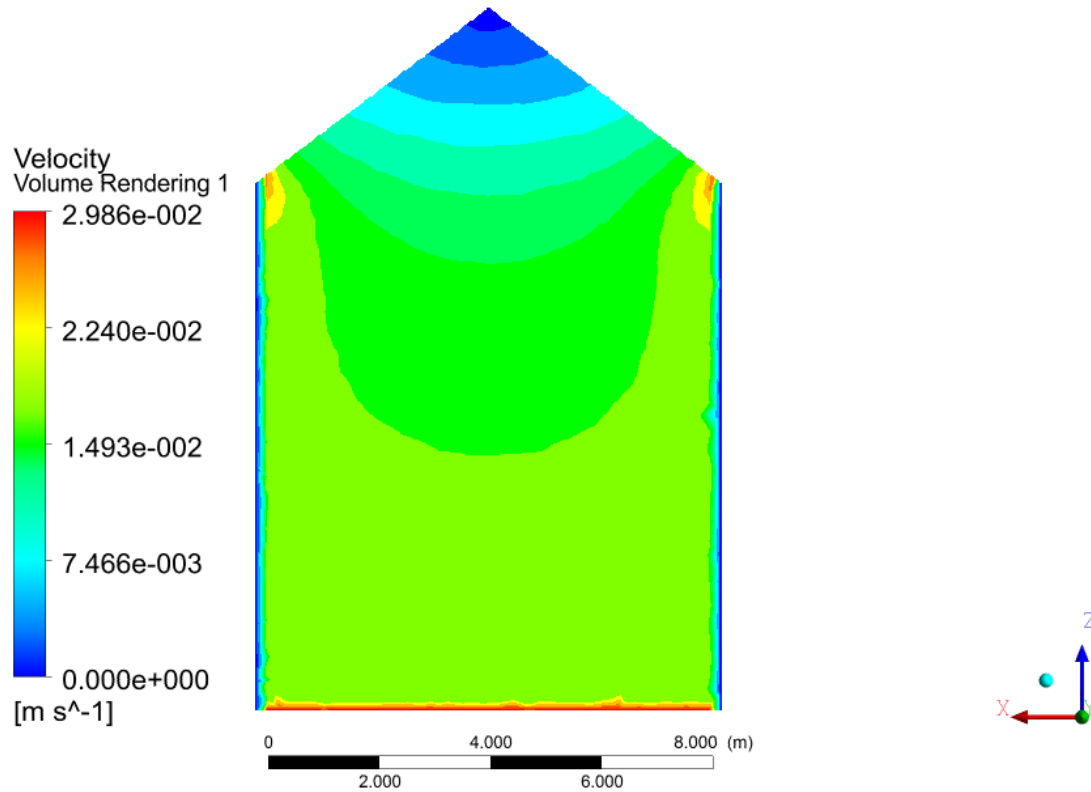


Figure 4.22 Simulated airflow velocity distribution for the soybeans bed at air inlet superficial velocity of 0.01 ms^{-1} (based on design flow rate of $0.0017 \text{ m}^3 \text{ s}^{-1} \text{ t}^{-1}$) for cylindrical bin with H:D =1.50.

4.4.3.3 Horizontal airflow aeration system

Studies have shown that moving air horizontally in grain mass appears to be easier than the traditional vertical flow of air due to lower resistance to airflow in the horizontal direction (Kumar and Muir, 1986; Jayas and Muir, 1991; Jayas and Mann, 1994; Noyes, 2006; Neethirajan et al., 2008; Chelladurai et al., 2015). CFD simulations based on the variable pore structure model (that is, variable porosity and tortuosity to account for compaction due to the self-weight of grain) were conducted to evaluate airflow and pressure patterns in a horizontal airflow system. The simulations were based on a similar bin design patented by Schreiner (Schreiner G., U.S. Patent No.0106042, 2016).

The bin consisted of perforated tubes (aerators) approximately 1.0 m in diameter and 7.0 m long, installed vertically at equidistance on the wall of the bin. Air moves radially from the aerator tubes towards the outlet tube (1.0 m in diameter and 10 m high) located at the center of the bin. The total amount of soybean grain to fill the 8 m diameter grain bin to a depth of 10 m was 459 tons and the total airflow rate was $0.78\text{m}^3\text{s}^{-1}$, which was based on the design flow rate of $0.0016\text{m}^3\text{s}^{-1}\text{t}^{-1}$ to achieve an inlet airflow velocity of 0.001ms^{-1} . The simulated distributions of pressure and airflow velocity are presented in figure 4.23 and 4.24, respectively.

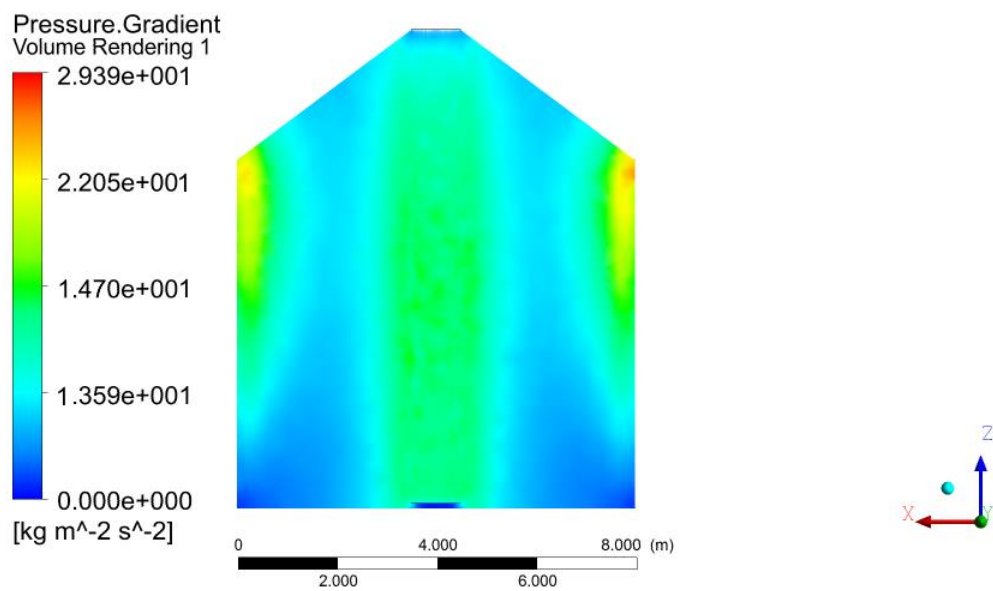


Figure 4.23 Simulated pressure pattern for variable pore structure grain bed for the horizontal airflow system.

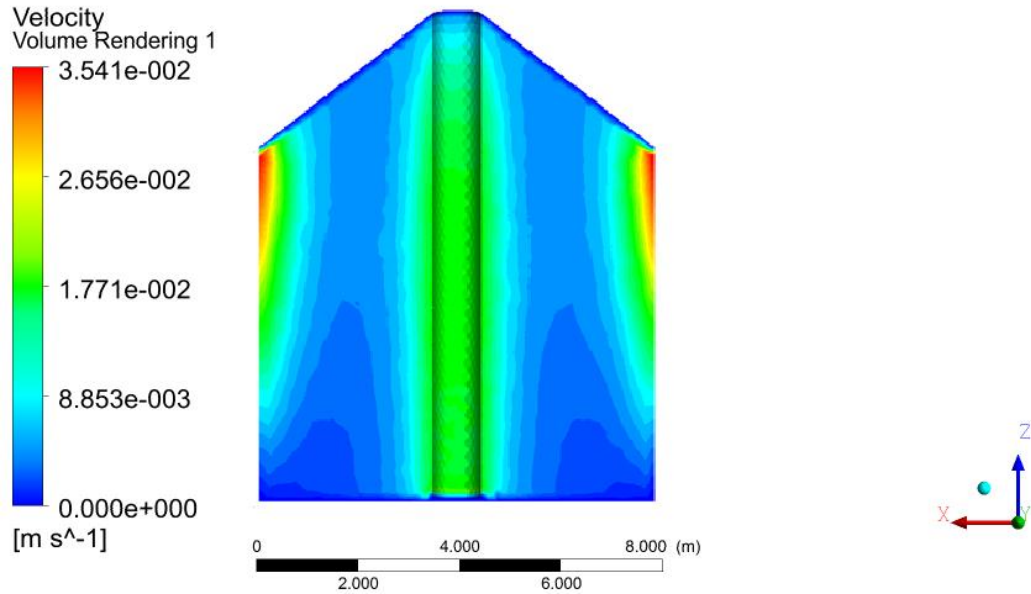


Figure 4.24 Simulated air velocity pattern for variable pore structure grain bed for the horizontal airflow system.

The simulated airflow velocity at the bottom of the grain bed where $z = 10\text{ m}$ was predicted as 0.0065 m s^{-1} , 1.7 m away from the walls and was 84.6 % lower than the airflow velocity at the top of the grain bed where $z = 4\text{ m}$ predicted as 0.012 m s^{-1} 1.7 m away from the wall (fig. 4.24). This very big difference in airflow velocity along the grain depth with horizontal airflow was as a result of the grain bed compaction effect due to the overlying grain depth that created pores of smaller sizes (lower porosity) at the bottom of the grain bed compared to larger pore sizes at the overlying top layers through the grain depth. So, even with the same aeration rate applied at the inlet, air entering into the bottom of the grain bed would encounter higher resistance. Simulation result reveals a dome-like velocity pattern at the bottom of the bin with lower air velocity that suggested that air was flowing through the least resistance upper region of the grain bed at relatively higher velocity to get to the exist tube located at the center of the grain mass but avoiding the bottom paths that pose higher resistance to its flow. This

observation might be one of major defects with horizontal aeration systems. Which means that, in large commercial grain storage bins, horizontal airflow would encounter immense non-uniformity in air flow as a result of the air flowing through the path of least resistance at the top of the grain bed. To benefit from the huge advantage of using horizontal airflow for the purpose of aeration, there should be a re-think in ducts design in order to optimize the horizontal airflow storage systems or a general re-design of large storage bins.

There have been many studies on horizontal duct designs for cylindrical vertical bins (Jayas et al., 1990; Jayas and Muir, 1991; Jayas and Mann, 1994; Neyos, 2006; Chelladurai et al., 2015). Jayas et al. 1990 suggested that using increase number of ducts would decrease non-uniformity that would occur as a result of horizontal airflow.

This was further confirmed in the simulation result completed in this study, increasing the number of ducts from 4 to 8 aerator tubes, installed on the bin wall did increased the effectiveness of aeration due to higher airflow velocity and pressure distribution all through the grain bed (fig 4.25c & 4.26d) compared with the airflow velocity and pressure pattern distribution when four aerator tubes were used (figs. 4.25a 74.25b). However, there was still, to some extent, non-uniformity in airflow and pressure distribution within the storage bin.

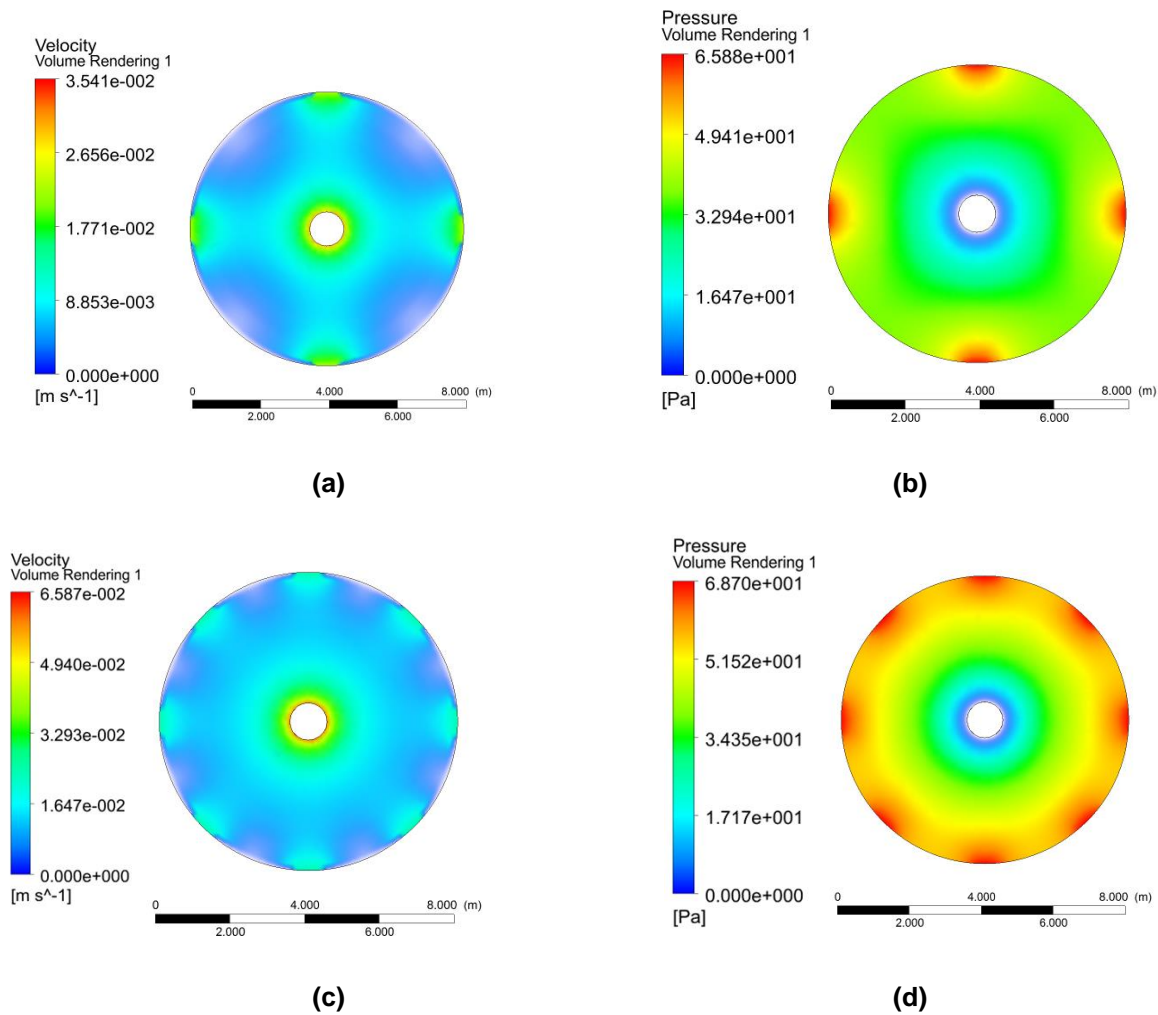


Figure 4.25 Simulated results of (a) airflow velocity distribution using four inlet tubes and (b) pressure distribution using four inlet tubes (c) airflow distribution using eight inlet tubes (d) pressure distribution using eight inlet tubes.

Another simulation was conducted to evaluate a variable sized duct system (variable inlet sectional area) and determine an inlet pressure distribution profile that would minimize non-uniformity within the grain storage bin. Specifically, variable inlet section area was created by using cone-shaped inlet tubes (7 m high with a base diameter of 1 m) mounted on the wall, equally spaced. One perforated cone-shaped tube (10m high with a base diameter of 1m) was located along the center of the bin extending from the

bottom of the bin to the roof to serve as the air outlet. The pressure distribution profile applied at the inlet was assumed to vary linearly with increase in the grain depth by implementation of a Fluent UDF that was based on a linear interpolation function to represent the inlet pressure profile in which higher pressure $P = 254 P$ was exerted on the inlet at the bottom of the grain bin at $z = 10 m$ and then the pressure progressively reduced along the grain depth based on the interpolation function to a second pressure applied on the inlet at the top of the bin $P = 10P$ at $z = 3 m$.

Figure 4.27 shows that the predicted airflow distribution based on the pressure profile applied on the inlet was sufficiently uniform compare with figure 4.24. The primary design goal of this system was to create higher pressure in the lower portion of the grain bed to compensate the compaction effect (fig. 4.26). The contour diagram showed that using cone-shaped tubes with linear interpolated pressure profile resulted in a fairly uniform airflow velocity distribution within the storage bin (fig. 4.27). That is, with a constant design airflow rate, applying higher pressure at the larger section area and lower pressure at the smaller section area of the inlet cone-shaped tube at the bottom and top of the bin respectively gave fairly uniform distribution within the grain storage systems. On the other hand, the decrease in the air inlet section area with corresponding pressure reduction achieved based on interpolation function is preferable than an increase in pressure under a smaller area or using a uniform cross section area and pressure at the inlet. The effectiveness of aeration process in horizontal airflow storage bin needs to be greatly improved. These improvements can be achieved, in particular, by optimizing the locations and numbers of the air inlet tubes (as shown in fig 4.25), or its sectional areas or the corresponding air pressure at the air inlet.

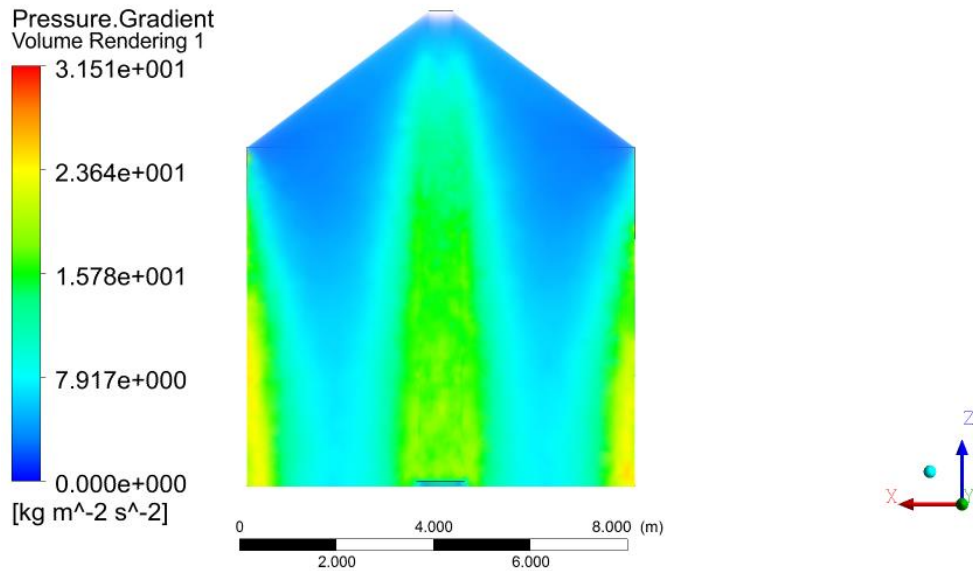


Figure 4.26 Results of airflow velocity distribution of variable pore structure simulation for the horizontal airflow using cone-shaped inlet tubes.

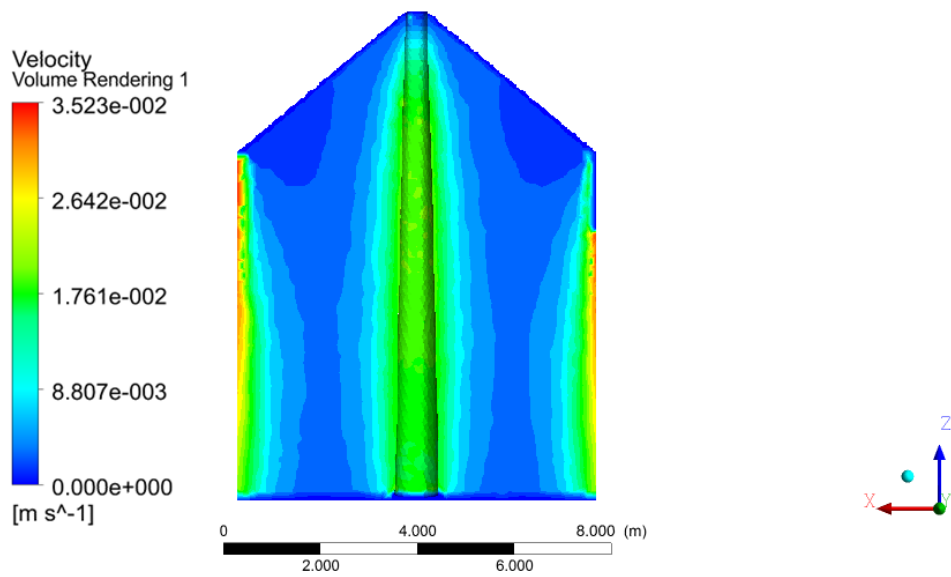


Figure 4.27 Results of airflow velocity distribution of variable pore structure simulation for the horizontal airflow using cone-shaped inlet tubes.

4.5 Predictions of anisotropic airflow by pore scale geometrical models

The models developed in section 3.6.2 were used to predict resistance to airflow, in which pore channels in the grain bulk was approximated by tube bundles stacked to a depth of 10 m. Using equation 3.31 the pore radius was predicted as a function of grain depth (fig. 4.28a). Similarly the intrinsic permeability was predicted by using equation 3.34 (fig. 4.28b). The predicted pore radius decreased from 1.19 to 0.86 mm from the top surface to the bottom, or a reduction of 28% for a 10 m deep bed due to compaction. The intrinsic permeability was estimated to be 1.78×10^{-7} and $9.7 \times 10^{-8} \text{ m}^2$ at the top and bottom (10 m) of the grain bed, respectively, or a 18.5% reduction.

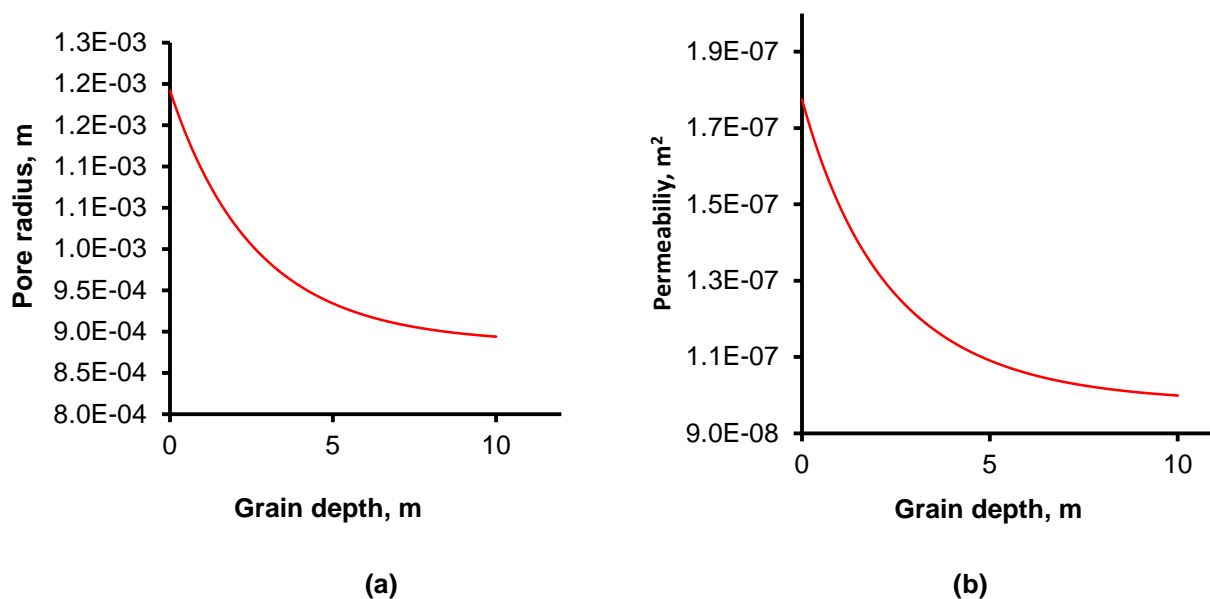


Figure 4.28 Predicted pore radius (a), and predicted intrinsic permeability (b) for 10m deep bed.

The permeability values predicted using the proposed pore-scale geometrical model were all in the range reported in the literature for bulk grains (Hunter, 1983; Khankari et al. 1995; Montross and McNeill, 2005). Khankari et al (1995) analyzed Patterson's et al.

(1971) data and calculated the permeability for corn to be in the range of $2.06 \times 10^{-8} m^2$ to $3.45 \times 10^{-8} m^2$. Hunter (1983) reported permeability of $2.55 \times 10^{-9} m^2$ and $5.84 \times 10^{-8} m^2$ for corn and wheat, respectively, based on Shedd's data (Shedd, 1953). Montross and McNeill (2005) conducted an experiment to measure the permeability of corn, soybeans, soft white winter wheat, and soft red winter wheat as a function of bulk density and moisture content. They reported that wheat had the lowest permeability between $1.15 \times 10^{-8} m^2$ and $7.29 \times 10^{-9} m^2$ depending on bulk density and moisture content, while corn and soybeans have similar permeability that varied between $1.30 \times 10^{-8} m^2$ and $3.03 \times 10^{-8} m^2$.

Using equations 3.27 and 3.40, the overall intrinsic permeability for a grain bed 10 m deep were calculated to be $1.21 \times 10^{-7} m^2$ for the horizontal direction, and $7.24 \times 10^{-8} m^2$ for the vertical direction. Similarly, the values of permeability for the horizontal and vertical directions were $1.34 \times 10^{-7} m^2$ and $9.23 \times 10^{-8} m^2$, respectively for a 5 m deep grain bed; and 1.62×10^{-7} and $1.47 \times 10^{-7} m^2$, respectively for a 1-m deep grain bed.

Using equations 3.21 and 3.35, the pressure drops were calculated from the permeability values for airflow velocities between $0.1 ms^{-1}$ and $0.5 ms^{-1}$ for the three different grain beds of 1 m, 5 m and 10 m (figs. 4.29, 4.30, and 4.31).

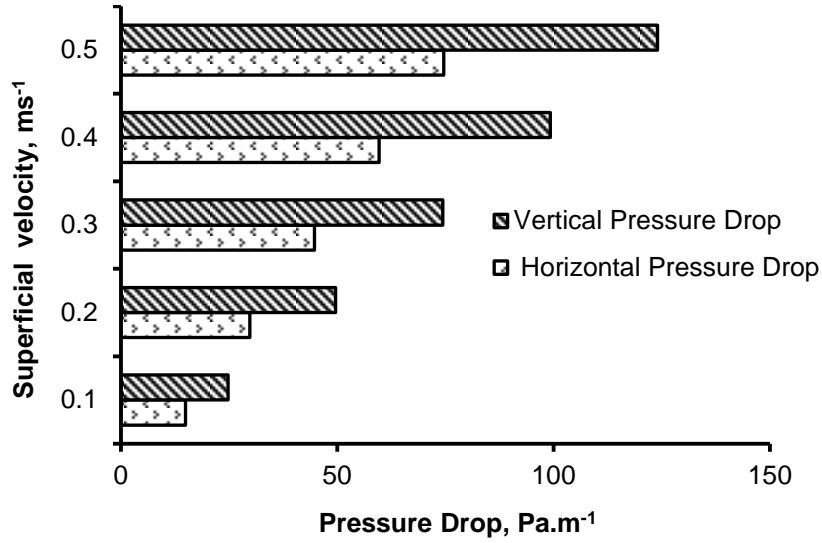


Figure 4.29 Comparison between vertical and horizontal pressure drop for a 10 m deep grain bed.

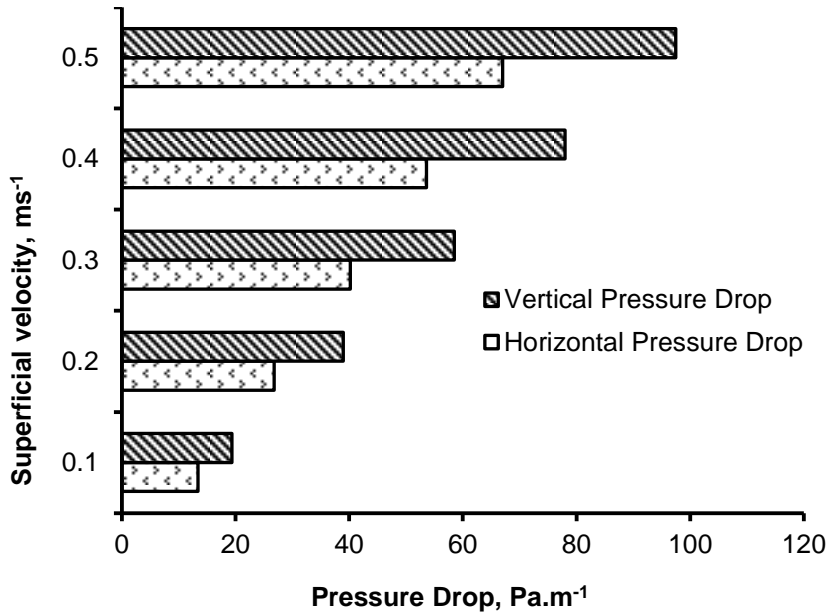


Figure 4.30 Comparison between vertical and horizontal pressure drop for a 5m deep grain bed.

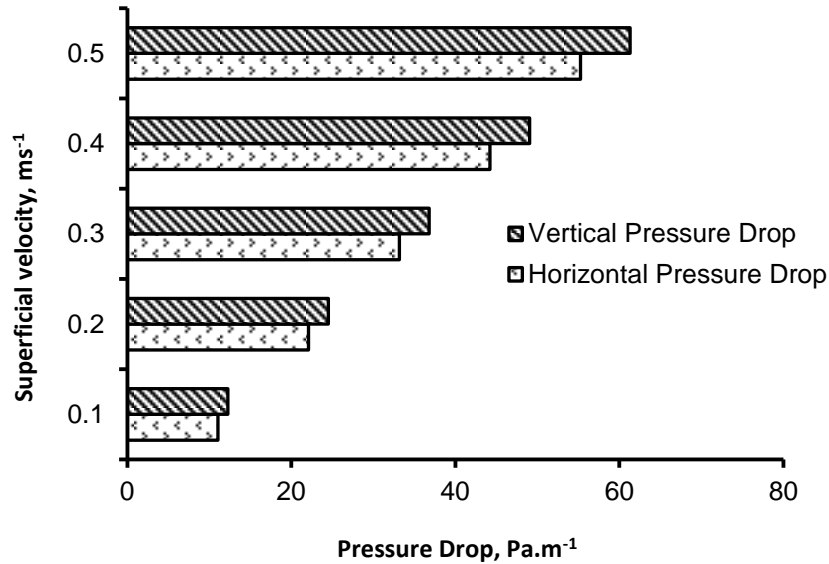


Figure 4.31 Comparison between vertical and horizontal pressure drop for a 1 m deep grain bed.

Three general observations could be made from the predicted pressure drops: i) the predicted resistance to airflow in the horizontal direction was lower than that in the vertical direction; ii) the difference in resistance to airflow between the horizontal and vertical directions increased with the grain depth, and iii) the relative difference in resistance to airflow between the horizontal and vertical directions did not vary with the air velocity. Specifically, at air velocity of $0.5 ms^{-1}$, the flow resistance in the horizontal direction was 60% of that in the vertical direction for the 10 m bed, 69% for the 5 m bed, and 90% for the 1 m bed. For the 10 m bed, the flow resistance in the horizontal direction was 60% of that in the vertical direction for all air velocities considered in this study (0.1 to $0.5 ms^{-1}$).

The predicted horizontal to vertical pressure drop (airflow resistance) differences were in the range reported in the literature. Kumar and Muir (1986) reported the differences in horizontal to vertical pressure drop ranged from 47%-65%. Jayas et al. (1987) reported

that airflow resistance was up to 50% higher in the vertical direction than in the horizontal direction. Neethirajan et al. (2008) reported that the differences in resistance to airflow in horizontal and vertical directions range between 15-90%.

The flow resistance in vertical direction predicted by the current model was 40% lower than that recommended by the ASABE Standard (ASAE R2011.D272.3, 2011). The large difference might be attributed to the simplified flow channels (tubes) in the current model, which did not explicitly account for complexities involved in pore structure within bulk grains. However, the overall intention of this model was to illustrate that compaction of grain layers was a contributing factor for differences in pressure drop (resistance to airflow) between the vertical and horizontal directions within bulk grains.

5 Conclusions and Recommendations

5.1 Conclusions

5.1.1 Effect of compaction on pore structure in bulk grains

The effect of compaction on pore structure characteristics (porosity and tortuosity) of bulk grain (soybean) was studied by using an image processing technique. The results showed that proposed method of 3D image reconstruction had potential of quantifying critical pore structure parameters such as porosity, tortuosity and pore connectivity in bulk grains. Compaction caused by grain pressure (depth) and vibration affected both porosity and tortuosity significantly. Specifically, porosity increased quickly at the low grain pressure and then gradually approached a minimum value. Porosity decreased from 0.42 to 0.34, or 19%, when the grain mass was subjected to a compaction pressure of 14.2kPa (equivalent to 2.2 m of grain depth). Tortuosity increased with the compaction pressure from 1.15 at 0 kPa to 1.58 at 14.2kPa , or by 37.4%. The effects of vibration on pore structure characteristics (porosity and tortuosity) were evident. At lower vibration intensity ($< 1g$), porosity and tortuosity changed little. Porosity reached a minimum value at critical vibration intensity around $2g$, and further increase in vibration intensity loosened the grain bulk, causing porosity to increase. At the critical vibration intensity ($2g$), porosity decreased from its initial value by 21%, whereas tortuosity increased by 15%.

5.1.2 Effect of pore structure variation on simulating airflow through bulk grains

Integrating pore structure models that describe variations of porosity and tortuosity in the grain bed into fluid mechanics model (e.g., CFD) simulations opened new possibilities to study airflow through bulk grains. A good agreement was found between

the CFD simulations considering variable pore structure and experimental data reported in the literature. Specifically, the relative difference was below 10% when the variable pore structure was considered in simulating pressure drops, whereas the relative difference was greater than 40 % when the constant pore structure was used in the simulations. This suggested that it is important to consider variations in pore structure when using CFD to simulate airflow through bulk grains. The validated variable pore structure model was demonstrated to have the capability to adequately predict airflow velocity and pressure drop distributions in grain aeration systems and can be sufficiently apply to determine operational risk locations such as non-aerated/stagnant zones within the aeration systems.

5.1.3 Directional dependency of resistance to airflow in bulk grains

Grain compaction may be an important contributing factor to anisotropic behaviour of airflow through bulk grains. Specifically, compaction may cause higher resistances to airflow in the vertical direction than in the horizontal direction because compaction results in smaller pores at greater grain depth. The geometrical models developed based on the compaction mechanism predicted pressure drop in the horizontal direction to be 60%, 68% and 90% of that in the vertical direction for 10 m, 5 m, and 1 m grain depths, respectively. This suggested that the anisotropic behaviour of airflow was more pronounced for deeper grain beds.

5.2 Recommendations

5.2.1 Further characterization of pore structure in bulk grains

Even with the success achieved in this study in the characterization and visualization of 3D pore structure within soybean grain bed, complete description of pore morphology in bulk grains still remains a formidable task. Although, there have been intensive research done on realistic porous media characterization, knowledge is still very limited in the area of bulk grains. In this study, we characterized porosity and tortuosity based on 3D reconstruction volumes and inter-connected airflow paths respectively and used the obtained data to investigate the effect of compaction and vibration on pressure drop and airflow distribution. Another interesting direction for future investigation is to study the effect on pressure drop and airflow distribution by variation in minor characteristics of pore structure such as pore volume, pore thickness or pore throat. This will be an immense topic for pore structure characterization within bulk grains.

5.2.2 Analyzing entrance and wall effects

One of our conclusions is that the entrance effects in porous media are dependent on pore structure characteristics and aspect ratio. From simulation conducted, there were clear deviations of higher pressure drop at the inlet for the variable pore structure bed that involved incorporating variable porosity and tortuosity to account for compaction due to the self-weight of grain into CFD Fluent simulation. Also, result from the simulations conducted reveal that bulk grain bed with higher aspect ratio has higher entrance effect and as the aspect ratio decreases, entrance effect reduced drastically. The reason provided for this was that higher aspect ratio consists of more grain mass which exerted higher compaction effect on the grain layer close to the entrance and

consequently caused reduction in pore sizes and increased in pressure drop. Apart from the entrance effect, complicating matters further, the wall region is likely to be highly influential. It is a known fact that at the wall, the porosity is likely to be considerably higher; therefore, this becomes the pathway of least resistance and increased airflow activity. In this study, we have been able to develop methodology based on CFD simulations to visually reveal patterns of airflow and pressure drop distribution within grain storage bins and how the pore structure variation affects these flow patterns. Entrance and the bin wall effects have been shown as one of the factors that were responsible for the patterns predicted through the CFD simulations. However, entrance effects on resistance to airflow in bulk grains need to be further investigated in order to understand its over-all effect on pressure drop. The configuration of the inlet pore structure conditions, flow developments, turbulences, viscous and inertial dissipations at the inlet should also all be considered in the over-all pressure drop investigation.

5.2.3 Incorporating vibration effect into flow through bulk grains

From the vibration experiment in this study, it was observed that local porosity and tortuosity varies with location (depth) during vibration and the magnitude of the variation depends on the vibration effect. And since bulk grain storage structures are sometime subjected to low amplitude vibration caused by routine operations, railway or vehicular traffic that impose dynamic force on grain storage structures (Hao et al. 1994; Ge et al. 2000). However, dynamic loads from these low amplitude vibration will not cause grain storage structural failure, but will, definitely, change grain kernels orientations which consequently will change the pore structure pattern within the bulk grain. It can be hypothesized that the dynamic load due to vibration impact on the storage structure

would create an oscillatory motion on grain kernels within the bulk grains, and consequently affect the airflow and pressure distribution. Incorporating compaction effect due to vibration on pore structure characteristics could be carried out with CFD Fluent simulation by modifying the UDF(s) developed in this study to better increase understanding of how compaction as a result of vibration would affect airflow velocity and pressure drop distribution through bulk grains in aeration systems.

Reference

- Abass, M.N. 2011. Modeling of porosity equation for water flow through packed bed of mono-size spherical packing. *Journal of Engineering and Development* 15(4): 205-226.
- Alagusundaram, K., and D.S. Jayas.1990. Airflow resistance of grains and oilseeds. *Postharvest News and Information* 1(4):279-283.
- Alagusundaram, K., D S. Jayas, F. Chotard and N.D.G. White.1992. Airflow pressure drop relationships of some specialty seeds. *Science des Aliments* 12(1):101–116.
- An, X., R., Y. Yang, K. Dong and A. Yu. 2011. DEM study of crystallization of mono-sized spheres under mechanical vibration. *Computer Physics Communications* 182:1989-1994.
- An, Z.Z., C.X. Li, R.Y. Yang, R.P. Zou and A.B. Yu. 2009. Experimental study of the packing of mono-sized spheres subjected one-dimensional vibration. *Power Technology* 196:50-55.
- An, X. Z., R.Y. Yang, R. P. Zou and A. B. Yu. 2008. Effect of vibration condition and inter-particle frictions on the packing of uniform spheres. *Powder Technology* 188: 102-109.
- ANSYS Inc.: Fluent 6.3 User's Guide, Chapter 7.2.2: Determination of Turbulence Parameters, September 2006.
- ANSYS Inc.: Fluent 6.3 User's Guide, Chapter 12: Modeling Turbulence, September 2006.
- ANSYS Inc.: Fluent 6.3 User's Guide, Chapter 3.1.1.: Porous Media Condition, September 2006.
- Anovitz L.M. and D. R. Cole. 2015. Characterization and analysis of porosity and pore Structures. *Reviews in Mineralogy and Geochemistry* 80(1): 61-164.
- ASABE Standard.2011. ASAE R2008 S352.2: Moisture measurement of unground grain and seed. St. Joseph Mich.: ASABE.
- ASABE Standard.1996. ASAE R2011. D272.3: Resistance to airflow of grains, seeds, other agricultural products and perforated metal sheet. St Joseph Mich.: ASABE.
- Aslannejad, H., S.M. Hassanizadeh, A. Raoof, D.A. Mde Winter, N. Tomozeiu and M.Th.van Genuchten. 2017. Characterizing the hydraulic properties of paper coating layer using FIB-SEM tomography and 3D pore-scale modeling. *Chemical Engineering Science* 50:275-280.

- Baldwin, C.A., A.J. Sederman, M. D. Mantle, P. Alexander, and L. F. Gladden. 1996. Determination and characterization of the structure of a pore space from 3D volume images. *Journal of Colloid Interface Science* 181:247-257.
- Barralet, J.E., T. Gaunt, A.J. Wright, I.R. Gibson and J.C. Knowles. 2002. Effect of porosity reduction by compaction on compressive strength and microstructure of calcium phosphate cement. *Journal of Biomedical Mater Review* 63(1):1-9.
- Barrande, M., R.Bouchet and R. Denoyel. 2007. Tortuosity of porous particles. *Analytical chemistry* 79(23):9115-9121.
- Bartosik, R.E and D. E. Maier. 2006. Effect of airflow distribution on the performance of NA/LT in-bin drying of corn. *Transactions of the ASABE* 49(4):1095-1104.
- Bear, J. 1972. *Dynamic of Fluids in Porous Media*, 1st edition. New York: Dove Publisher.
- Blümich, B., J. Mauler, A. Haber, J. Perlo, E. Danieli and F. Casanova. 2009. Mobile NMR for geophysical analysis and materials testing. *Petroleum Science* 6(1):1-7.
- Boccardo, G.D., R. Marchisio, R. Sethi. 2014. Micro scale simulation of particle deposition in porous media, *Journal of Colloid and Interface Science* 417:227-237.
- Bodla, K. K., V.G. Suresh and Y. M. Jayathi. 2014. 3D reconstruction and design of porous media from thin sections. *International Journal of Heat and Mass Transfer* 73:250-264.
- Boudreau, M.P.1996. The diffusive tortuosity of fine-grained unlithified sediments. *Geochimica et Cosmochimica Acta* 60:3139-3142.
- Brooker, D.B., F.W. Bakker-Arkema, and C.W. Hall.1974. *Drying cereal grains*. 2nd edition. Westport, Conn. USA: The AVI publishing Company.
- Brooker, D.B. 1961. Pressure patterns in grain drying systems established by numerical methods. *Transaction of the ASAE* 4(1):72-77.
- Chan, S. K. and K. M. Ng. 1988. Geometrical characteristics of the pore space in a random packing of equal spheres. *Powder Technology* 54:147-155.
- Chelladurai, V., V.R. Parker, D.S. Jayas, and N. D. G. White. 2015. Evaluation of a horizontal air flow in-bin grain drying system. *Applied Engineering in Agriculture* 31(5): 793-798.
- Cheng, X., Q. Zhang, X. Xiaojie, and S. Cuixia. 2015. Compressibility and equivalent bulk modulus of shelled corn. *Biosystems Engineering* 140:91-97.

- Collison, D. 2015. Geometry based prediction of laminar flow characteristics through non-homogeneous porous media. Unpublished M.Sc thesis. Christchurch, New Zealand: University of Canterbury.
- Comiti, J. and M. Renaud. 1989. A new model for determining mean structure parameters of fixed beds from pressure drop measurement: application to beds packed of parallelepipedal particles. *Chemical Engineering Science* 44:1539-1545.
- Darcy, H. 1856. Experimental research relating to the movement of water in pipes in French "Recherches Experimentales Relatives au Mouvement de L'Eau dans les Tuyaux. Paris: Mallet-Bachelier.
- Doktor, T., D. Kytýř, J. Valach and O. Jiroušek. 2010. Assessment of pore size distribution using image analysis. Trieste, Italy: YSESM.
- Dullien, F.A.L. 1992. *Porous Media: Fluid Transport and Pore Structure*. New York: Academic Press.
- Du Plessis, J. P., and S. Woudberg. 2008. Pore-scale derivation of the ergun equation to enhance its adaptability and generalization. *Chemical Engineering Science* 63(9): 2576-2586.
- Du, Q., and M. Gunzberger. 2002. Grid generation and optimization based on centroidal Voronoi tessellations. *Applied Mathematics and Computation* 133(2):591-607.
- Ergun, S. 1952. Fluid flow through packed columns. *Chemical Engineering Progress* 48(2):89-94.
- Feldbusch, A., H. Sadegh-Azar, P. Agne. 2017. Vibration analysis using mobile devices (smartphones or tablets). *Procedia Engineering* 199:2790-2795.
- Florence, C. and C. Laurent. 2008. Porous structure and water vapour sorption of hemp-based materials. *Construction and Building Materials* 22(6):1271-1280.
- Forchheimer, P. 1901. Wasserbewegung durch boden, Zeit. Ver. Deutsch. Ing. 45: 1781-1788.
- Fraser, M. A. and W.E. Muir. 1980. Energy consumptions predicted for drying grain with ambient and solar-heated air in Canada. *Journal of Agricultural Engineering Research* 25(3): 325-331.
- Fredrich, J. F., A. A. DiGiovani and D.R. Noble. 2006. Predicting macroscopic transport properties using microscopic image data. *Journal of Geophysical Research* 111:1-14.

- Hao, D., Q. Zhang and M. G. Britton. 1994. Effect of vibration on loads in a corrugated model grain bin. *Canadian Agricultural Engineering* 36 (1):29-35.
- Haque, E. 2011. Void fraction as a function of depth pressure drops of packed beds of porous formed by granular materials. *Transaction of the ASAE* 54(6):2239-2243.
- Haque, E. 2013. Estimating bulk density of compacted grains in storage bins and modifications of Janssen's load equations as affected by bulk density. *Food Science Nutrition* 1(2):150-156.
- Haque, E., G.H. Foster, D.S. Chun and F. S. Lai. 1978. Static pressure drop across a bed of corn mixed with fines. *Transaction of the ASAE* 21(5), 997-1000.
- Hickling, R., W. Wei and D.W. Hagstrum. 1997. Studies of sound transmission in various types of stored grain for acoustic detection of insects. *Applied Acoustic* 50(4):263-278
- Hihinashvili, R. and R. Blumenfeld. 2010. Structural characterization of porous and granular materials. International Conference on Water Resources. Barcelona: CIMNE.
- Hilmi, S.S. and V.C. George. 2000. Physical and mathematical aspect of tortuosity in regards to fluid flow and electric current conduction in porous media: example of Hibernia and Terra Nova reservoirs, offshore the eastern coast of Canada. *Energy source* 22:137-145.
- Hood, T.J.A. and G.R. Thorpe. 1992. The effects of the anisotropic resistance to airflow on the design of aeration systems for bulk stored grains. *Agricultural Engineering Australia* 21:18- 23.
- Hu, J. and S. Piet. 2003. Application of image analysis to assessing critical pore size for permeability prediction of cement paste. *Image Analysis and Stereology* 22:97-103
- Hukill, W.V., and N.C. Ives. 1955. Radial airflow resistance of grain. *Journal of Agricultural Engineering* 36(5):332-335.
- Hunter, A.J. 1983. Pressure difference across an aerated seed bulk for some common duct and store cross section. *Journal of Agricultural Engineering Research* 28:437-450.
- Galvan, S., M. Reggio and F. Guibault. 2011. Assessment Study of K- ϵ Turbulence Models and Near-Wall Modeling for Steady State Swirling Flow Analysis in Draft Tube Using Fluent. *Engineering Applications of Computational Fluid Mechanics* 5(4):459-478.

- Garg, D. 2005. Modeling non-uniform airflow and its application for partial chilled aeration using PHAST-FEM. Unpublished M.Sc. thesis. West Lafayette, Indiana: Purdue University.
- Garg, D. and D.E. Maier. 2006. Modeling non-uniform airflow distribution in large grain silos using Fluent. 9th International Working Conference on Stored Product Protection. PS7-12-6158.pg 754-762 Sao Paulo, Brazil. October 15-18.
- Gayathri, P. and D.S. Jayas. 2007. Mathematical modeling of airflow distribution in grain bulks – a review. ASABE Paper No. 076226. St. Joseph, MI: ASABE.
- Ge, T., Q. Zhang and M.G. Britton. 2000. Predicting grain consolidation caused by vertical vibration. *Transactions of the ASAE* 43(6):1747-1753.
- Gonzalez-Montellano, C. 2011. Applications of the discrete element method to the study of granular materials stored in silos and hoppers. Unpublished Ph.D thesis. Madrid, Spain: University of Politecnica.
- Górnicki, K. and A. Kaleta. 2015. Resistance of bulk grain to airflow – a review. part II: effect of process parameters. *Agricultural and Forest Engineering* 65:43-51.
- Iversen, N. and B. Jorgensen. 1993. Diffusion coefficients of sulfate and methane in marine sediments: influence of porosity. *Geochimica et Cosmochimica Acta* 57(3): 571-578.
- Izadi, .H., M. Baniassadl, A. Hasanabadi, B. Mehrgini, H. Memarian, H. Soltanian-Zadeh and K. Abrinia. 2017. Application of full set of two point correlation functions from a pair of 2D cut sections for 3D porous media reconstruction. *Journal of Petroleum Science and Engineering* 149:789-800.
- James, K.M., and F.B. Leslie. 1985. Compaction factors for six crops. *Transactions of the ASAE* 26(5): 1634-1636.
- James, B.K., G.F. Christopher, N.L Chun, M.J. Heinrich and R.N. Sidney. 1995. Density relaxation in a vibrated granular material. *Physical reviews* 51(5): 3957-3963.
- Janssen H.A. 1895. Versuche über Getreidedruck in Silozellen. *Zeitschrift, Verein Deutscher Ingenieure* 39:1045-1049.
- Jayas, D.S., K. Alagusundaram, G. Shunmugam, W.E. Muir, and N.D.C. White. 1994. Simulated temperatures of stored grain bulks. *Canadian Agricultural Engineering* 36:239-245.
- Jayas, D. 2012. Grain Storage for Food Security and Safety: Research at the University of Manitoba, Canada. *Journal of Agricultural Engineering* 49(1):1-12.

- Jayas, D. 2015. Forced Air Ventilation through Bulk Grains for Cooling and Drying: An Overview. Speech delivered at the University of Manitoba. Winnipeg, Manitoba. Feb 22, 2015.
- Jayas, D.S., S. Sokhansanj, E.B. Moysey and E.M. Barber. 1987. The effect of airflow direction on the resistance of canola (rapeseed) to airflow. *Canadian Agricultural Engineering* 29(2):189-192.
- Jayas, D. and N.D.G White. 2003. Storage and drying of grain in Canada: low cost approaches. *Food Control* 14(4):255-261.
- Jayas, D.S. and W.E. Muir. 1991. Airflow-pressure drop data for modeling fluid flow in anisotropic bulks. *Transaction of the ASAE* 34(1):251-254.
- Jayas, D.S. and D.D. Mann. 1994. Presentation of airflow resistance data of seed bulks. *Applied Engineering in Agriculture* 10(1):79-83.
- Jekayinfa, S.O. 2006. Effect of airflow rate, moisture content and pressure drop on the airflow resistance of locust bean seed. *Agricultural Engineering International* 9:345-359.
- Jian, F., D.S. Jayas, N.D.G. White, and K. Alagusundaram. 2005. A three-dimensional, asymmetric, and transient model to predict grain temperatures in grain storage bins. *Transaction of the ASAE*, 48: 263-271.
- Jiang, C., Daigle. H, and S. Bryant. 2015. A bundle of short conduits model of the pore structure of gas shale. Unconventional Resources Technology Conference, San Antonio, Texas, 20-22 July 2015: pp. 1530-1543.
- Jindal, V.K. and T.L. Thompson. 1972. Air pressure pattern and flow paths in two dimensional triangular shaped piles of sorghum using forced convection. *Transaction of the ASAE* 15(4): 737-747.
- Jones, C. J. C. and J. R. Block. 1996. Prediction of ground vibration from freight trains. *Journal of sound and vibration* 193(1):205-213.
- Kamath, J., B. Xu, S.H. Lee, and Y.C. Yortsos. 1998. Use of pore network models to interpret laboratory experiments on vugular rocks. *Journal of Petroleum Science and Engineering* 20:109-115.
- Karababa, E. 2006. Physical properties of popcorn kernels. *Journal of Food Engineering* 72(1): 100-107.
- Kashaninejad, M., Y.Maghsoudlou, M. Khomeiri, and L.G.Tabil. 2010. Resistance to airflow through bulk pistachio nuts (Kalleghochi variety) as affected by moisture

- content, airflow rate, bed depth and fill method. *Powder Technology* 203(2):359-364.
- Karsten, E.T. 2002. Fast and robust delaunay tessellation in periodic domains. *International Journal for Numerical Methods in Engineering* 55(11):1345-1366..
- Kenghe, R.N., P.M. Nimkar, S.S. Shirkole and K.J. Shinde. 2012. Airflow resistance in soybean. *International Agrophysics* 26:137-143.
- Kenghe, R. N., K. R. Kenghe, P.M. Nimkar, and S.S. Shirkole. 2013. Effect of Bulk Density, Moisture Content, and Grain Size on Vertical Airflow Resistance of Lathyrus (*Lathyrus sativus* L.) Grains. *Legume Genomics and Genetics* 4(2):14-20.
- Khankari, K. K., R. V. Morey and S. V. Patankar. 1995. Application of a numerical model for prediction of moisture migration in stored grain. *Transactions of the ASAE* 38(6):1789-1804.
- Khatchatourian, O.A., N. Toniazzo and F. Tosini. 2009. Experimental study and mathematical modeling of airflow in grain bulks under anisotropic conditions. 11th Pan-American Congress of Applied Mechanics, PR, Brazil, January 04-08.
- Khatchatourian, O.A. and D.L. Savicki. 2004. Mathematical modeling of airflow in an aerated soya bean store under non-uniform conditions. *Biosystems Engineering* 88(2):201-211.
- Khatchatourian, O.A., O. Manuel, and F. Vanessa. 2016. Three-dimensional simulation and performance evaluation of air distribution in horizontal storage bins. *Biosystems Engineering* 142:42-59.
- Kibar, H. and T. Öztürk . 2008. Physical and mechanical properties of soybean. *International Agrophysics* 22(3):239-244
- Klemens, F., S. Schuhmann, G. Guthausen, G. Thäter and J.K. Mathias. 2018. CFD-MRI: A coupled measurement and simulation approach for accurate fluid flow characterization and domain identification. *Computer and Fluids* 166:218-224.
- Koponen, A., M. Kataja, and J. Timonen.1996. Tortuous flow in porous media. *Physical Review* E54(1):406-410.
- Kumar, A. and W.E. Muir. 1986. Airflow resistance of wheat and barley affected by airflow direction, filling method and dockage. *Transaction of the ASAE* 29(5):1423-1426.
- Lai, F. S. 1980. Three-dimensional flow of air through non-uniform grain beds. *Transactions of the ASAE* 23(3):729-734.

- Lamond, W .J. and E. A. Smith. 1982. Modeling low temperature drying of grain in anisotropic beds. *Third International Drying Symposium*, 61-72. Birmingham, U.K.
- Lao, W., J.N. Henry and D. V. Papavassiliou. 2004. A pore network model for the calculation of non-darcy flow coefficients in fluid flow through porous media, *Chemical Engineering Communications* 191(10):1285-1322.
- Lawrence, J. and D.E. Maier. 2011. Three-dimensional airflow distribution in a maize silo with peaked, leveled and cored grain mass configurations. *Biosystems Engineering* 110(3):321-329.
- Lawrence, J. and D.E. Maier. 2012. Prediction of temperature distribution in peaked leveled and inverted cone grain mass configuration during aeration of corn. *Applied Engineering in Agriculture* 28(5):685-692.
- Lawrence, J., D. E. Maier and R. L. Strohshine. 2013. Three-dimensional transient heat, mass, momentum and species transfer model using the finite element method. Part I Model Development. *Transaction of the ASABE* 56(1):179-188.
- Liang, Z.R., Fernandes . C.P., Magnani . F.S., and P.C.Philippi. 1998. A reconstruction technique for three-dimensional porous media using image analysis and Fourier transforms. *Journal of Petroleum Science and Engineering* 21(3): 273-283
- Lukaszuk, J., M. Molenda, J. Horabik, B. Szot and M.D. Montross. 2008. Airflow resistance of wheat bedding as influenced by the filling method. *Journal Agricultural Engineering Research* 54(2):50-57.
- Lukaszuk, J., M. Molenda, J. Horabik, B. Szot and M.D. Montross. 2009. Variability of pressure drops in grain generated by kernel shape and bedding method. *Journal of Stored Product Research* 45:112-118.
- Maciej, M., K. Arzhang, K. Zbigniew. 2008. Tortuosity-porosity relation in the porous media flow. *Physical Reviews E* 78(2):1-8.
- Maciej, M., and K. Zbigniew. 2012. How to calculate tortuosity easily. Wroclaw, Poland: Institute of theoretical Physics
- Mohsenin, N.N. 1986. Physical properties of plant and animal materials: Structure, physical characteristics, and mechanical properties. New York, NY: Gordon and Breach Publisher
- Molenda, M., M.D. Montross, J. Horabik and S.G. McNeill . 2005. Airflow resistance of seeds at different bulk densities using Ergun's equation. *Transactions of the ASAE* 48(3):1137-1145.

- Montillet, A. and L.L. Coq. 2001. Characteristics of fixed beds packed with anisotropic particles – use of image analysis. *Powder Technology* 121:138-148.
- Montross, M.D., D.E. Maier and K. Haghighi. 2002. Development of finite element stored eco-system model. *Transactions of the ASAE* 45(5):1455-1464.
- Montross, M.D. and S.G. McNeill. 2005. Permeability of corn, soybeans, soft red and white wheat as affected by bulk density. *Applied Engineering in Agriculture* 21(3):479-484.
- Moses, J. A., D.S. Jayas and K. Alagusundaram. 2013. Resistance to airflow through bulk grains, oilseeds and other agricultural products – a review. *Journal Agricultural Engineering* 50:1-13.
- Moses, J. A., D.S. Jayas and K. Alagusundaram. 2014. Three-dimensional airflow pressure patterns in flat-bottom bins filled with barley for different duct configurations. *Trends in Biosciences* 7(17): 2392-2396.
- Mueller. G.E. 1997. Numerical simulation of packed beds with mono-sized spheres in cylindrical container. *Powder Technology* 92:179-183.
- Münch, B., P. Gasser, and R. Flatt. 2006. FIB Nanotomography of particulate systems - Part II: particle recognition and effect of boundary truncation. *Journal American Ceramics Society* 89(8): 2586-2595.
- Navarro, S. and R. Noyes. 2002. *The mechanics and physics of modern grain aeration management*. Boca Raton: CRC Press.
- Navarro, S., R.T. Noyes, M. Casada, and F.H. Arthur. 2012. Aeration of grain. In *Stored Product Protection*, 121-134. Kansas, US.: Kansas State University.
- Neethirajan, S., C. Karunakaran, D.S.Jayas, and N.D.G. White. 2006. X- ray computed tomography image analysis to explain the airflow resistance differences in grain bulks. *Biosystems Engineering* 94:545-555.
- Neethirajan, S., D.S. Jayas, N.D.G. White and H. Zhang. 2008. Investigation of 3D geometry of bulk wheat and pea pores using X-ray computed tomography images. *Computer and Electronics* 63:104-111
- Neyo, R.T. 2006. Development of a new low-energy environmentally compatible grain and seed drying and storage technology. 9th International Working Conference on Stored Product Protection. KP1-1, 1285-1294. Sao Paulo, Brazil. Sao Paulo, Brazil. October 15-18.

- Nguyen, T. V. 1987. Natural convection effects in stored grains: A simulation study. *Drying Technology* 5(4): 541-560.
- Nimkar, P.M. and P.K. Chattopahyay. 2002. Airflow resistance of green gram. *Biosystems Engineering* 82(4):407-414.
- Nimmo, J.R. 2004. Porosity and pore size distribution. In: *Encyclopedia of Soils in Environment*: London Elsevier.
- Nolan.G. T. and Kavanagh. P.E. 1995. Octahedral configurations in random close packing. *Powder Technology* 83: 253-258.
- Nwaizu, C. 2013. Characterizing of airflow paths in grain bulks. Unpublished Msc. Thesis: Department of Biosystems Engineering, University of Manitoba.
- Nwaizu, C. and Q. Zhang. 2015. Characterizing tortuous airflow paths in a grain bulk by using smoke visualization. *Canadian Biosystems Engineering* 57 (3):13-22.
- Nwaizu, C. and Q. Zhang. 2017. The effect of compaction on pore structure in bulk grain. Paper No. CSBE17-125, Winnipeg, MB: CSBE.
- Olatunde. G., and G. Griffiths, A. Atungulu, and S. Sadaka. 2016. CFD modeling of air flow distribution in rice bin storage system with different grain mass configurations. *Biosystems Engineering* 151:286-297.
- Olatunde. G., and G.Griffiths and A. Atungulu. 2017. Potential of turbulence interference in rough rice bin drying and storage systems fitted with cabling technology. *Biosystems Engineering* 163(1):1-14.
- Olson, J.F. 1999. Pore-scale simulation of experimentally realizable, oscillatory flow in porous rock. Earth Resources Laboratory Department of Earth, Atmospheric, and Planetary Sciences: Massachusetts Institute of Technology, Cambridge, MA.
- Onu. C.J. 2016. Selected Physical properties of soybean in relation to storage design . *International Journal of Engineering Research and Applications* 6 (2):71-75.
- Pagano, A.M., S.M. Crozza and S.M. Nolasco. 2000. Airflow resistance of oat seeds: effect of the airflow direction, moisture content, and foreign material. *Journal of Drying Technology* 18:457-468.
- Pagliai, M. and N. Vignozzi. 2012. Istituto Sperimentale per lo studio e la Difesa del suolo. Piazza M.D' Azeglio 30-50121 Firenze, Italy.

- Peng, S.,H. Qinong, D. Stefan, and M. Zhang. 2012. Using X-ray computed tomography in pore structure characterization for a Berea sandstone: Resolution effect. *Journal of Hydrology* 472:254-261.
- Rahul, V., B.L. Pamela, and S. Abdel-Fattah. 2010. New approach for determining tortuosity in fibrous porous media. *Journal of Engineered Fibers and Fabrics* 5(3):7-15.
- Rajabipour, A; Shahbazi F; Mohtasebi S; Tabatabaeefar A. 2001. Airflow resistance in walnuts. *Journal of Agricultural Science Technology* 3: 257-264.
- Rezanezhad, F., W. L. Quinton, J. S. Price, D. Elrick, T.R. Elliot and and R. J. Heck 2009. Examining the effect of pore size distribution and shape on flow through unsaturated peat using computer tomography. *Hydrology of Earth Systems Science* 13:1994-2002.
- Richard G., J.F. Cousin, A. Bruand and J. Guerif. 2001. Effect of compaction on the porosity of a silty soil: Influence on unsaturated hydraulic properties. *European Journal Of soil Science* 52:49-58.
- Rizk, A., G. Paul, P. Incardona, M. Bugarski, M. Mansouri, A. Niemann, U. Ziegler, P. Berger, and I. F. Sbalzarini.2014. Segmentation and quantification of subcellular structures in fluorescence microscopy images using Squash. *Nature Protocols* 9(3): 586-596.
- Robertson, A.G. and D.J. Campbell. 1997. Simple, low-cost image analysis of soil pore structure. *Journal of Agricultural Engineering Research* 68:291-296.
- Schneider, C. A., W.S. Rasband and K .W. Eliceiri. 2012. NIH Image to ImageJ: 25 years of image analysis. *Nature methods* 9(7): 671-675.
- Schoeman, L .2017. Characterization and quantification of microstructure, physic chemical and functional properties of oven and forced convection continuous tumble roasted cereal grains. Unpublished PhD Thesis. South Africa: Department of Food Science, Stellenbosch University.
- Schreiner, G.A. 2014. Cross Flow Aeration System. Patent No. US20140026436A1. United State Patent Application Publication.
- Schwab, C.V., I.J. Ross, G.M. White and D.G. Colliver. 1994. Wheat loads and vertical pressure distribution in a full-scale bin. *Transaction of the ASAE* 37(5):1613-1619.
- Sederman, A. J., P. Alexander, and L. F. Gladden. 2001. Structure of packed beds probed by magnetic resonance imaging. *Powder Technology* 117: 255-269.

- Shahbazi, F. 2011. Resistance of bulk chickpea seeds to airflow. *Journal of Agricultural Science Technology* 13:996-676.
- Shedd, C.K. 1953. Resistance of grains and seeds to air flow. *Agricultural Engineering* 34(9):616–619.
- Shedd, C.K. 1951. Some new data on resistance of grains to airflow. *Journal of Agricultural Engineering* 32:493-495.
- Sinha, R.N., J.T. Mills, H.A.H. Wallace and W.E. Muir. 1981. Quality assessment of rapeseed stored in ventilated and non-ventilated farm bins. *Science des Aliment* 1(2): 247-263.
- Smith, E.A. and D.S. Jayas. 2004a. Calculation and limitations of traverse time **93** in designing forced ventilation systems. *Transaction of the ASAE* 47:1635-1642.
- Smith, E.A. and D.S. Jayas. 2001. Modeling the movement of fumigant gas within grain beds. *Transactions of the ASAE* 44(3):661-667.
- Smith, E.A., D.S. Jayas and A. de Ville. 2001. Modeling the flow of carbon dioxide through beds of cereal grains. *Transport Porous Media* 44:123-144.
- Smith, E.A. and S. Sokhansanj, 1990. Moisture transport caused by natural convection in grain stores. *Journal of Agricultural Engineering Research* 47:23-34
- Sobieski, W., Q. Zhang and C. Liu. 2012. Predicting tortuosity for airflow through Porous Beds Consisting of Randomly Packed Spherical Particles. *Transport in Porous Media* 93(3):431-451.
- Sobieski, W., W. Dudd and S. Lipiński. 2016. A new approach for obtaining the geometric properties of a granular porous bed based on DEM simulation. *Technical Sciences* 19(2) 165-187.
- Sobieski, W., and S. Lipiński. 2017. The analysis of the relations between porosity and tortuosity in granular beds. *Technical Sciences* 20(1):75-85.
- Teng, Y., G. Lu, Fan . Y., Liu, L. Yu, L. Jiang, D. Wang and Y. Song. 2017. Experimental study of density-driven convection in porous media by using MRI. *Energy Procedia* 105:4210-4215.
- Thévenaz, P., U.E. Ruttimann and M. Unser. 1998. A Pyramid approach to subpixel Registration Based on Intensity. *IEEE Transactions on Image Processing* 7(1): 27-41
- Thompson, S.A. and I.J. Ross. 1983. Compressibility and frictional coefficients of wheat. *Transaction of the ASAE* 26(4):1171-1176.

- Thompson, S.A., S.G. McNeill, J.J. Ross and T.C. Bridges. 1987. Computer model for predicting the packing factors of whole grains in flat storage structures. *Applied Engineering in Agriculture* 3(2):215-221.
- Thompson, T. L. 1972. Temporary storage of high-moisture shelled corn using continuous aeration. *Transaction of the ASAE* 15(2): 333-337.
- Tsukahara, M., S. Mitrovic, V. Gajdosik, G. Margaritondo, L. Pournin, M. Ramaioli, D. Sage, Y. Hwu, M. Unser, and Th. M. Liebling. 2008. A coupled Tomo-DEM approach to explore the granular media microstructure in a jamming hourglass *Physics Review E* 77: 061306.
- Vogel, H.J. and A. Kretschmar. 1996. Topological characterization of pore space in soil- sample preparation and digital image processing. *Geoderma* 73:23-38.
- Xiong, Q., G. Todor, A. Baychev and P. Jivkov. 2016. Review of pore network modelling of porous media: experimental characterizations, network constructions and applications to reactive transport. *Journal of Contaminant Hydrology* 192:101-117.
- Xiao, M., Reddi, L.N. (2008). "Pore structure variation of porous media under vibration." Proceedings of Geotechnical Earthquake Engineering and Soil Dynamics IV Conference, Sacramento, CA. ASCE Geotechnical Special Publication No. 181, May 18-22.
- Yan, Z., C. Chen, P. Fan, M. Wang and F. Xiang. 2015. Pore structure characterization of ten typical rocks in China. *Electronic Journal of Geotechnical Engineering* 20(2):479-484.
- Yang, B., A. Wu, X. Miao and J. Liu. 2014. 3D characterization and analysis of pore structure of packed ore particles beads based on computed tomography images. *Transactions of Nonferrous Metals Society of China* 24:833-838.
- Yu, S.W., J. Lucas., V. Van, W. Henderik and V. Kess. 2006. The determination of relative path length as a measure for tortuosity in compacts using image analysis. *European Journal of Pharmaceutical Sciences* 28:434-440.
- Yue, R. and Q. Zhang. 2017. Changes of pore structure of porous beds when subjected to vertical vibration. *KONA powder and Particle Journal* 34: 224-233.
- Yue, R. and Q. Zhang. 2017. A pore-scale model for predicting resistance to airflow in bulk grain. *Biosystems Engineering* 155:142-151.

- Yun, J., Y.Yue, and B. Yu. 2010. A geometrical model for tortuosity of tortuous streamline in porous media with cylindrical. Chinese Physics letter 27(10):1047041-1047044.
- Zhang, Q., V.M. Puri and H.B. Manbeck. 1987. Determination of elastoplastic constitutive parameters for wheat en masse. Transactions of the ASAE 29(6):1739-1746.

Appendix A: 3D visualization and skeletonization

A.1.1. 3D visualization and skeletonization of largest inter-connected airflow path during compaction

- **Compaction test for grain depth = 0.2 m**

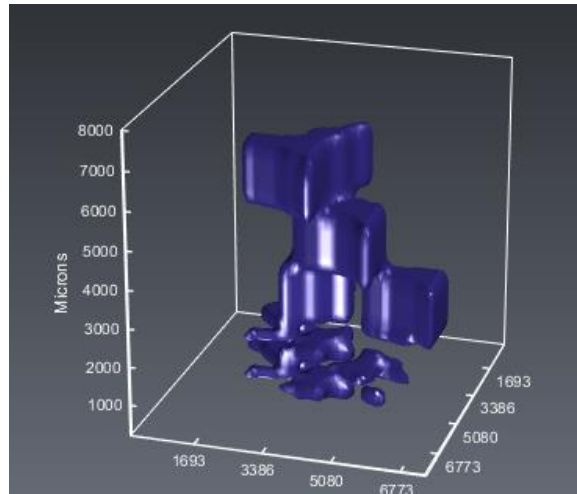


Figure A.1.0. Extracted 3D reconstructed of the inter-connected paths for grain depth, $d = 0.2\text{m}$ with the highest degree of connectivity.

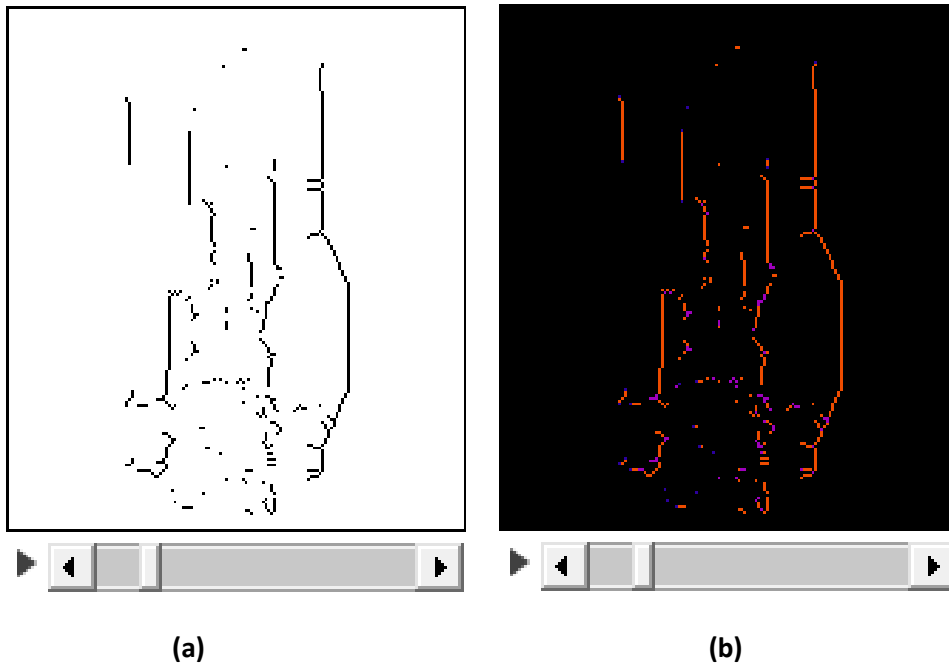


Figure A.1.1. Result of direct skeletonization process from binary image of the inter-connected flow paths with highest degree of connectivity for grain depth, $d = 0.2\text{m}$ and applied Skeleton3D to obtain (a) thin skeletonized image, which was then analyzed by AnalyzedSkeleton3D to formed (b) pruned thin skeletonized image from which different possible paths/branches from the thin skeleton were estimated.

➤ **Compaction test for grain depth = 0.5 m**

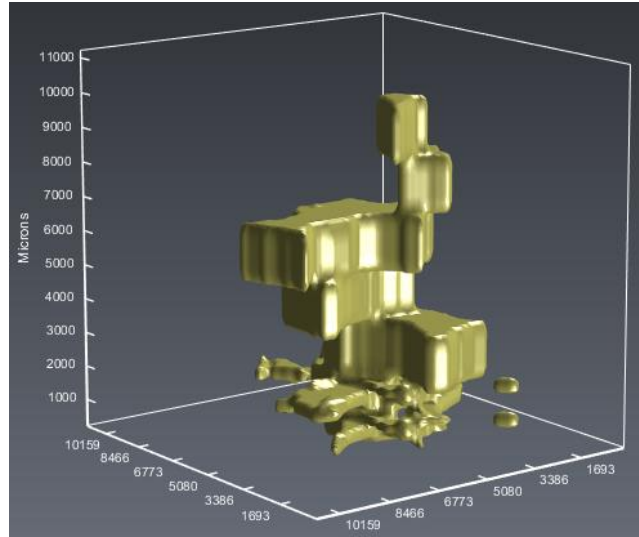


Figure A.1.2. Extracted 3D reconstructed of the inter-connected paths for grain depth, $d = 0.5\text{m}$ with the highest degree of connectivity.

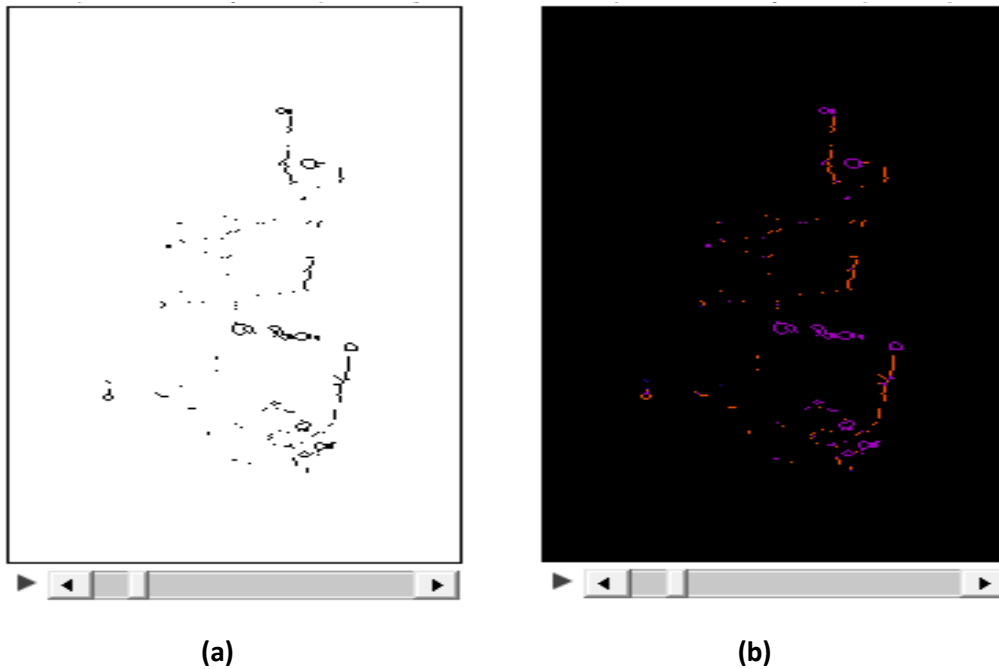


Figure A.1.3. Result of direct skeletonization process from binary image of the inter-connected flow paths with highest degree of connectivity for grain depth, $d = 0.5\text{m}$ and applied Skeleton3D to obtain (a) thin skeletonized image, which was then analyzed by AnalyzedSkeleton3D to formed (b) pruned thin skeletonized image from which different possible paths/branches from the thin skeleton were estimated.

➤ **Compaction test for grain pressure = 1.0 m**

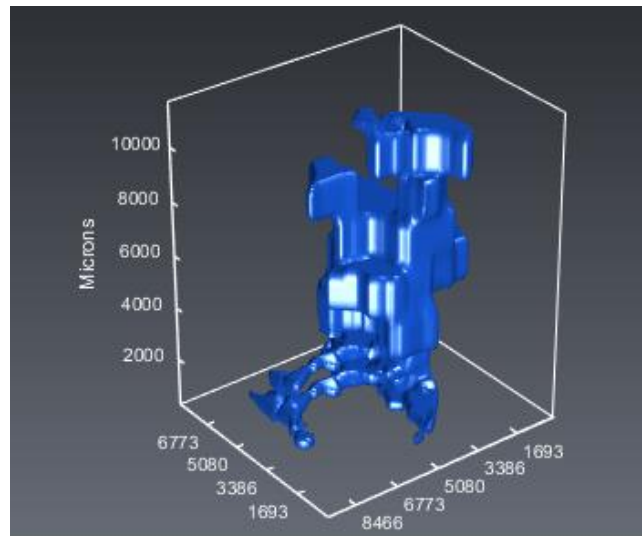


Figure A.1.4. Extracted 3D reconstructed of the inter-connected paths for grain depth, $d = 1.0\text{m}$ with the highest degree of connectivity.

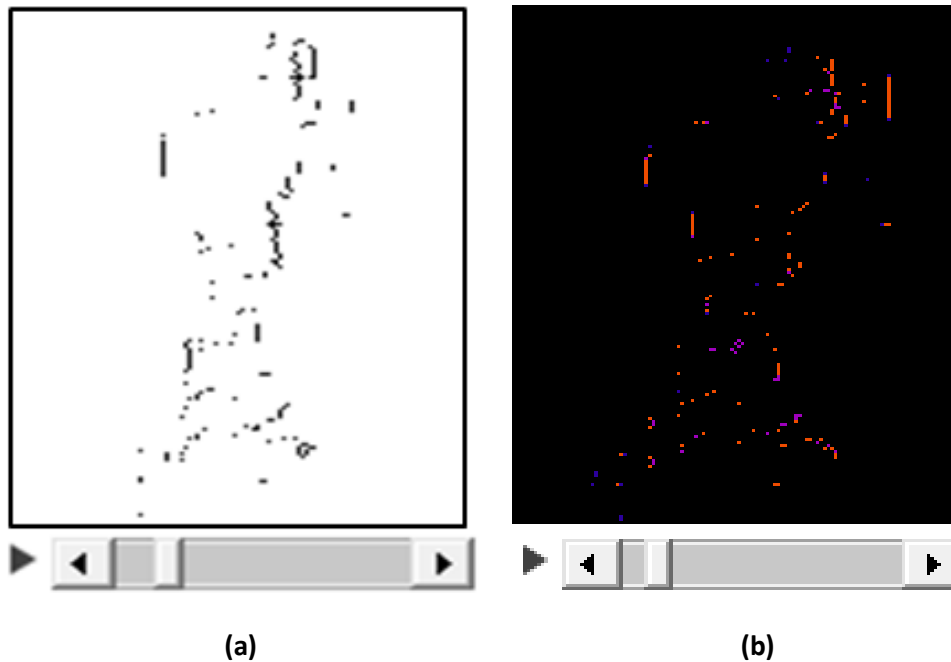


Figure A.1.5. Result of direct skeletonization process from binary image of the inter-connected flow paths with highest degree of connectivity for grain depth, $d = 1.0\text{m}$ and applied Skeleton3D to obtain (a) thin skeletonized image, which was then analyzed by AnalyzedSkeleton3D to formed (b) pruned thin skeletonized image from which different possible paths/branches from the thin skeleton were estimated.

➤ **Compaction test for grain pressure = 1.5 m**

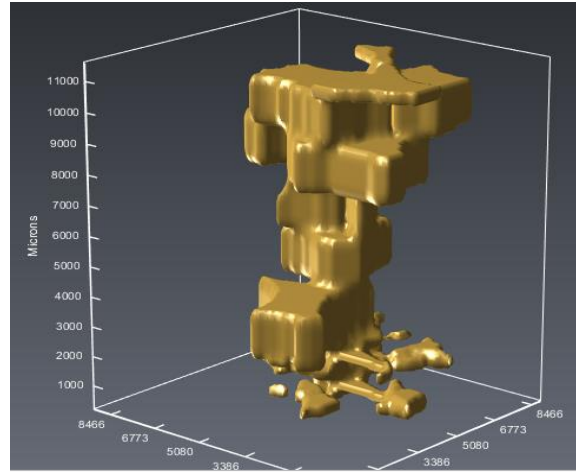


Figure A.1.6. Extracted 3D reconstructed of the inter-connected paths for grain depth, $d = 1.5\text{m}$ with the highest degree of connectivity.

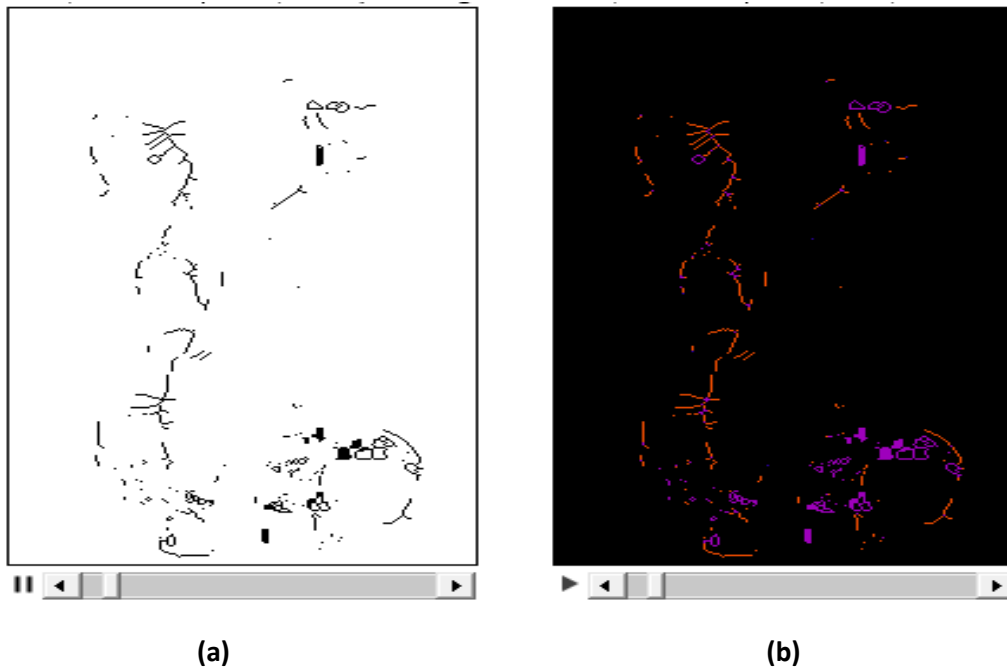


Figure A.1.7. Result of direct skeletonization process from binary image of the inter-connected flow paths with highest degree of connectivity for grain depth, $d = 1.5\text{m}$ and applied Skeleton3D to obtain (a) thin skeletonized image, which was then analyzed by AnalyzedSkeleton3D to formed (b) pruned thin skeletonized image from which different possible paths/branches from the thin skeleton were estimated.

➤ **Compaction test for grain pressure = 1.8 m**

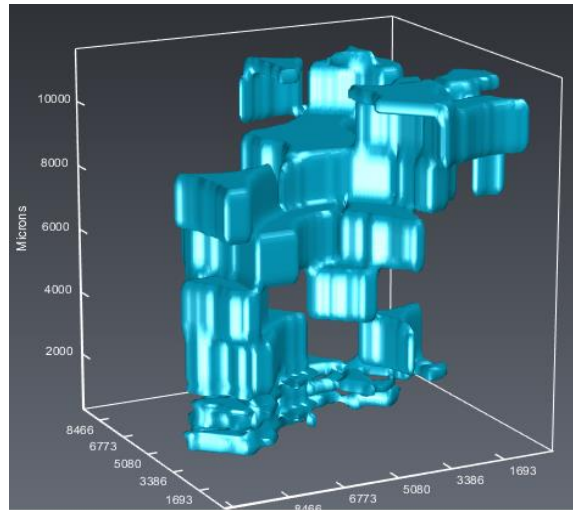


Figure A.1.8. Extracted 3D reconstructed of the inter-connected paths for grain depth, $d = 1.8\text{m}$ with the highest degree of connectivity.

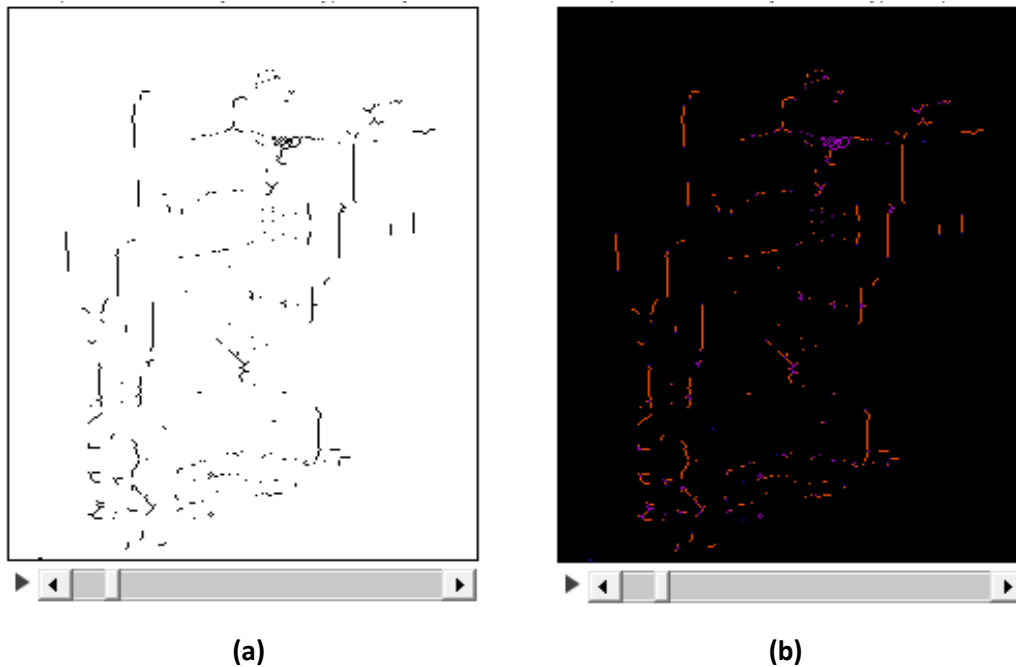


Figure A.1.9. Result of direct skeletonization process from binary image of the inter-connected flow paths with highest degree of connectivity for grain depth, $d = 1.8\text{m}$ and applied Skeleton3D to obtain (a) thin skeletonized image, which was then analyzed by AnalyzedSkeleton3D to formed (b) pruned thin skeletonized image from which different possible paths/branches from the thin skeleton were estimated.

➤ **Compaction test for grain pressure = 2.2 m**

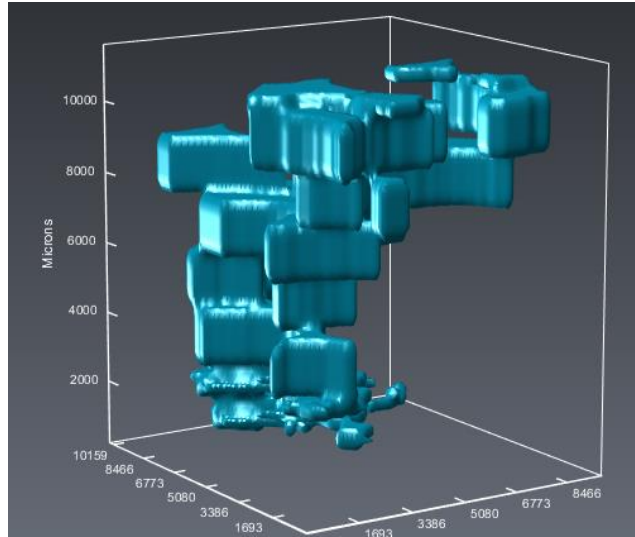


Figure A.1.10. Extracted 3D reconstructed of the inter-connected paths for grain depth, $d=2.2$ m with the highest degree of connectivity.

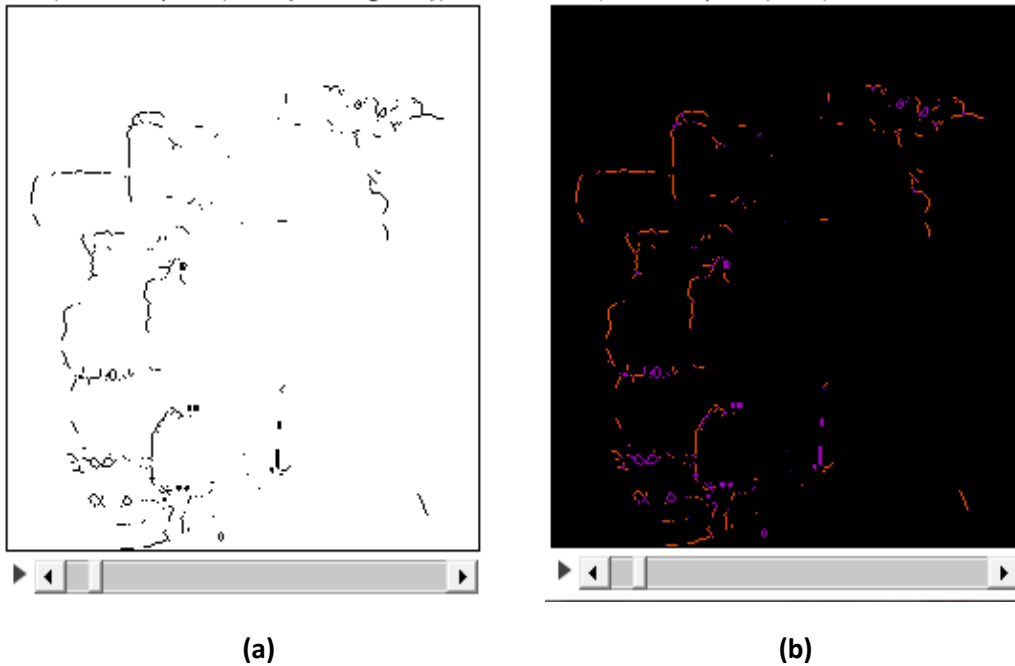


Figure A.1.11. Result of direct skeletonization process from binary image of the inter-connected flow paths with highest degree of connectivity for grain depth, $d = 2.2$ m and applied Skeleton3D to obtain (a) thin skeletonized image, which was then analyzed by AnalyzedSkeleton3D to formed (b) pruned thin skeletonized image from which different possible paths/branches from the thin skeleton were estimated.

A.1.1. 3D visualization and skeletonization of largest inter-connected airflow path during vibration

- **Vibration test for intensity = 0.5G**

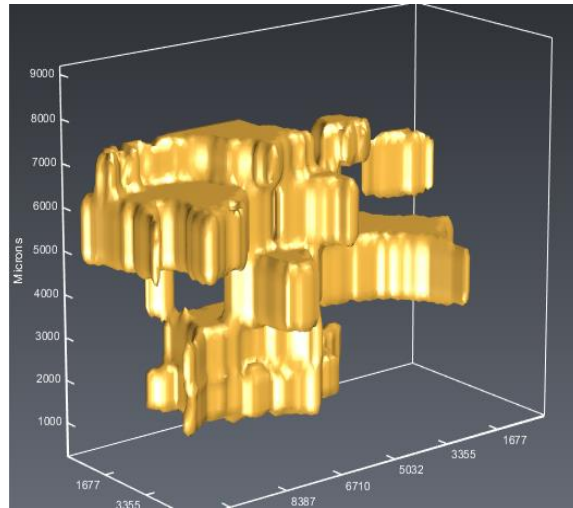


Figure A.1.12. Extracted 3D reconstructed of the inter-connected paths for vibration intensity, $\Gamma = 0.5g$ with the highest degree of connectivity.

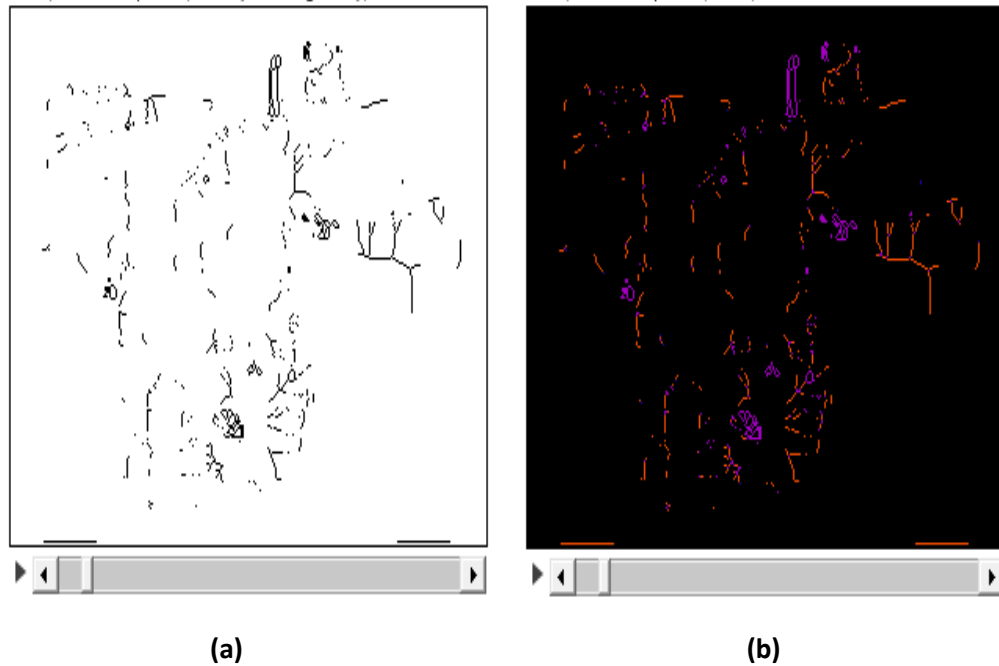


Figure A.1.13. Result of direct skeletonization process from binary image of the inter-connected flow paths with highest degree of connectivity for vibration intensity, $\Gamma = 0.5g$ and applied Skeleton3D to obtain (a) thin skeletonized image, which was then analyzed by AnalyzedSkeleton3D to formed (b) pruned thin skeletonized image from which different possible paths/branches from the thin skeleton were estimated.

➤ For vibration intensity = 1.0G

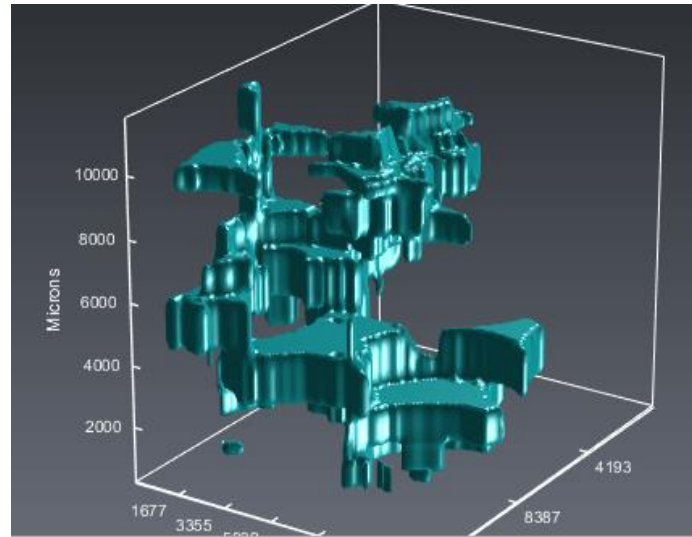


Figure A.1.14. Extracted 3D reconstructed of the inter-connected paths for vibration intensity, $\Gamma=1.0g$ with the highest degree of connectivity.

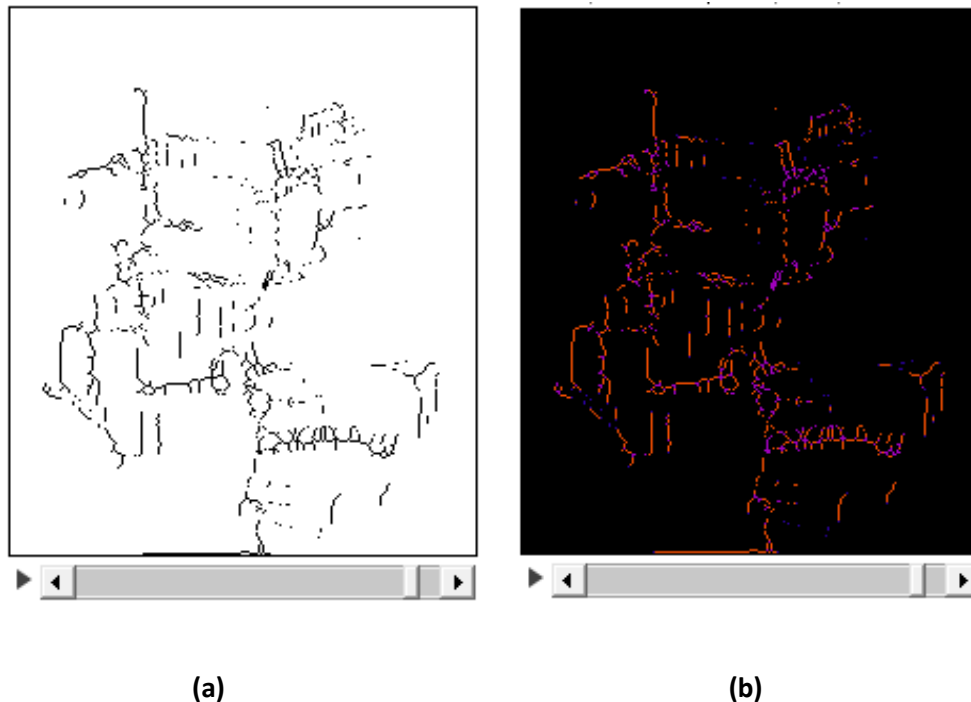


Figure A.1.15. Result of direct skeletonization process from binary image of the inter-connected flow paths with highest degree of connectivity for vibration intensity, $\Gamma=1.0g$ and applied Skeleton3D to obtain (a) thin skeletonized image, which was then analyzed by AnalyzedSkeleton3D to formed (b) pruned thin skeletonized image from which different possible paths/branches from the thin skeleton were estimated.

➤ For vibration intensity = 1.5G

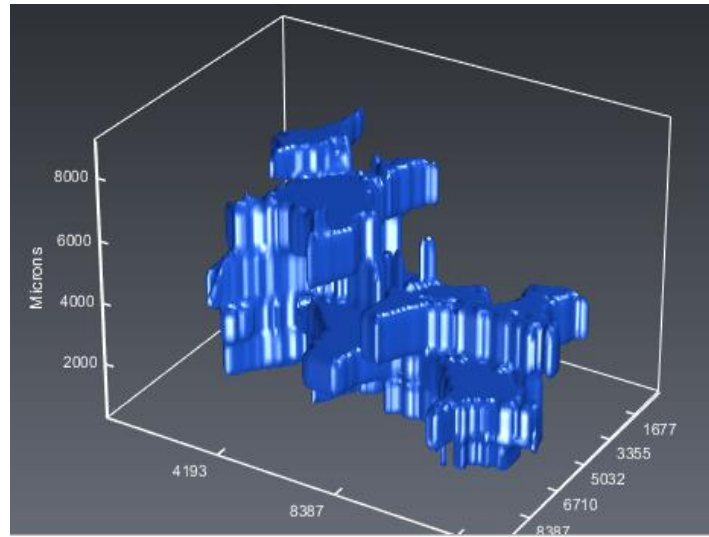


Figure A.1.16. Extracted 3D reconstructed of the inter-connected paths for vibration intensity, $\Gamma = 1.5g$ with the highest degree of connectivity.

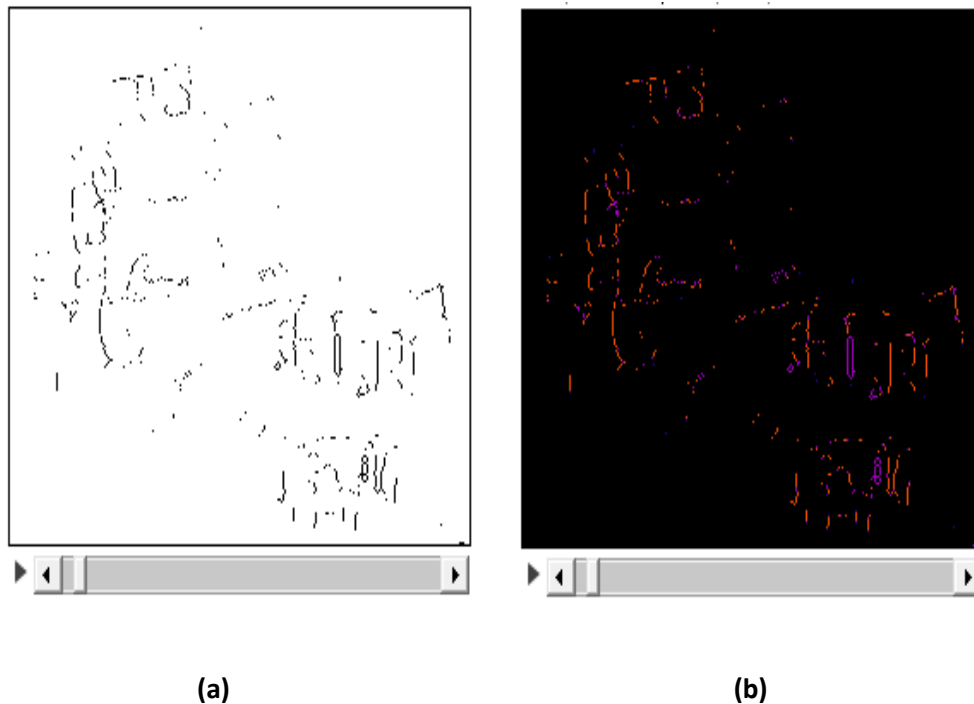


Figure A.1.17. Result of direct skeletonization process from binary image of the inter-connected flow paths with highest degree of connectivity for vibration intensity, $\Gamma = 1.5g$ and applied Skeleton3D to obtain (a) thin skeletonized image, which was then analyzed by AnalyzedSkeleton3D to formed (b) pruned thin skeletonized image from which different possible paths/branches from the thin skeleton were estimated.

➤ For vibration intensity = 2.0G

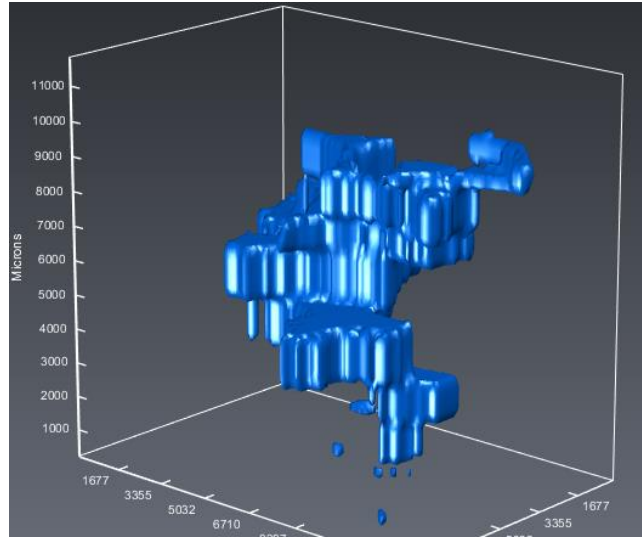
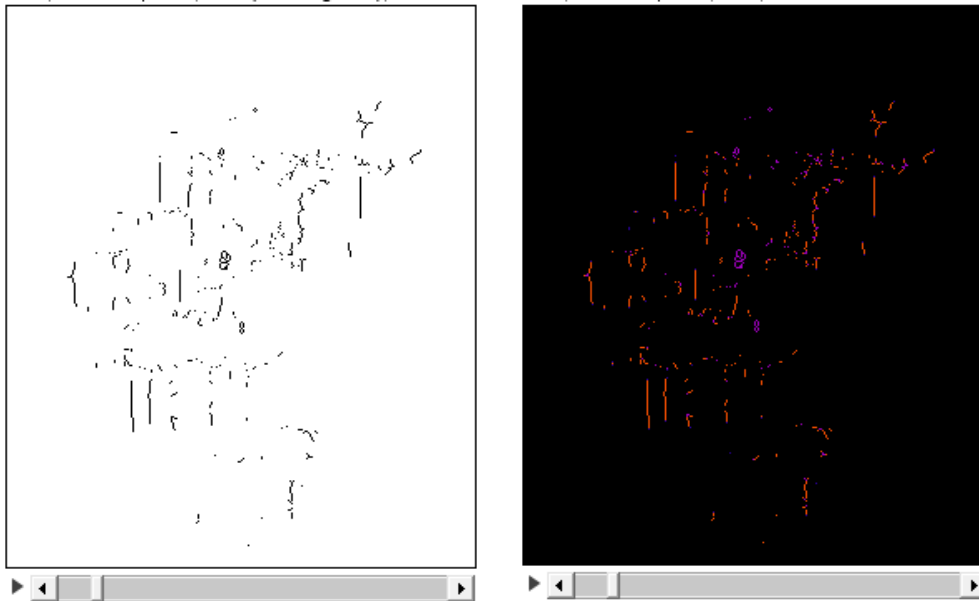


Figure A.1.18. Extracted 3D reconstructed of the inter-connected paths for vibration intensity, $\Gamma = 2.0g$ with the highest degree of connectivity.



(a)

(b)

Figure A.1.19. Result of direct skeletonization process from binary image of the inter-connected flow paths with highest degree of connectivity for vibration intensity, $\Gamma = 2.0g$ and applied Skeleton3D to obtain (a) thin skeletonized image, which was then analyzed by AnalyzedSkeleton3D to formed (b) pruned thin skeletonized image from which different possible paths/branches from the thin skeleton were estimated.

➤ For vibration intensity = 2.5G

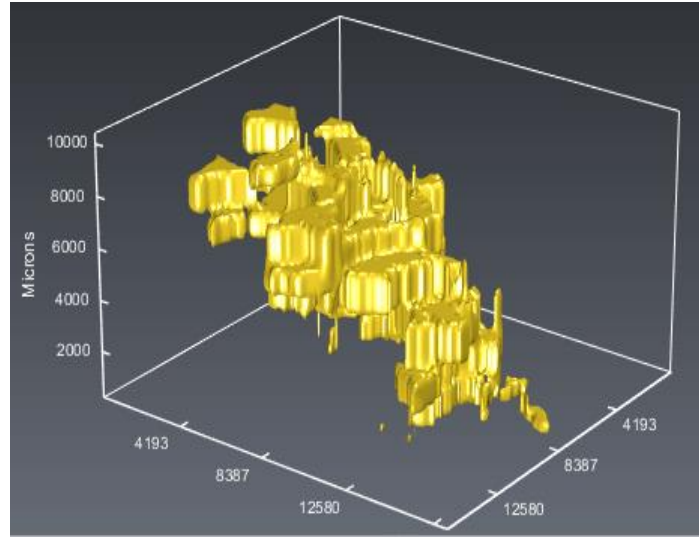


Figure A.1.20. Extracted 3D reconstructed of the inter-connected paths for vibration intensity, $\Gamma = 2.5g$ with the highest degree of connectivity.

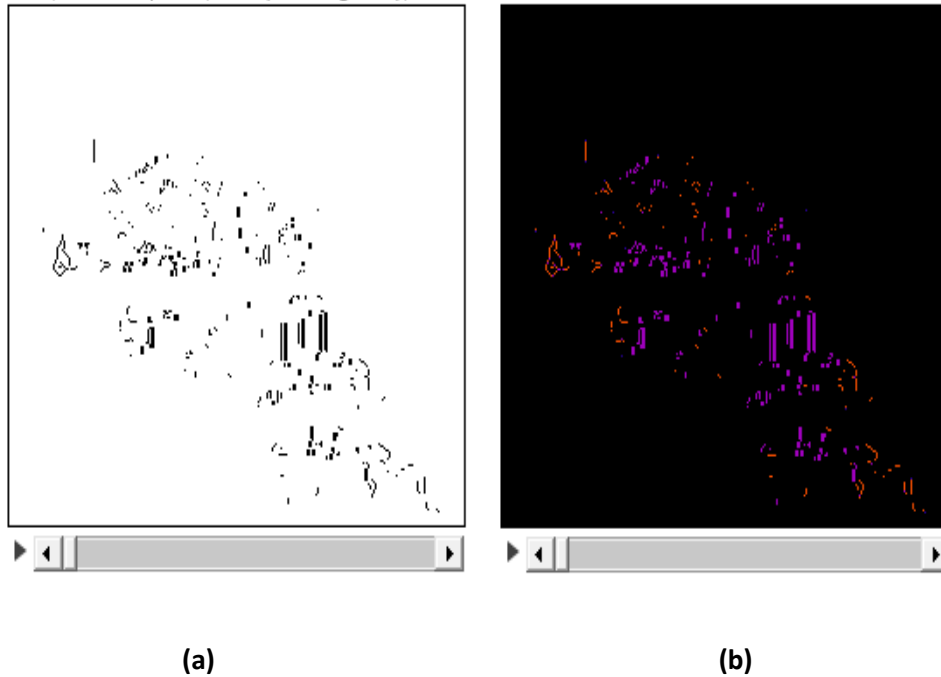


Figure A.1.21. Result of direct skeletonization process from binary image of the inter-connected flow paths with highest degree of connectivity for vibration intensity, $\Gamma = 2.5g$ and applied Skeleton3D to obtain (a) thin skeletonized image, which was then analyzed by AnalyzedSkeleton3D to formed (b) pruned thin skeletonized image from which different possible paths/branches from the thin skeleton were estimated.

➤ For vibration intensity = 3.0G

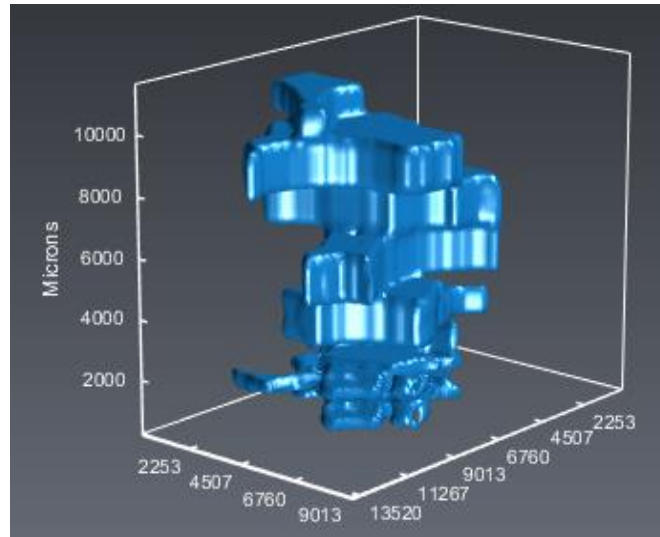


Figure A.1.22. Extracted 3D reconstructed of the inter-connected paths for vibration intensity, $\Gamma=3.0g$ with the highest degree of connectivity.

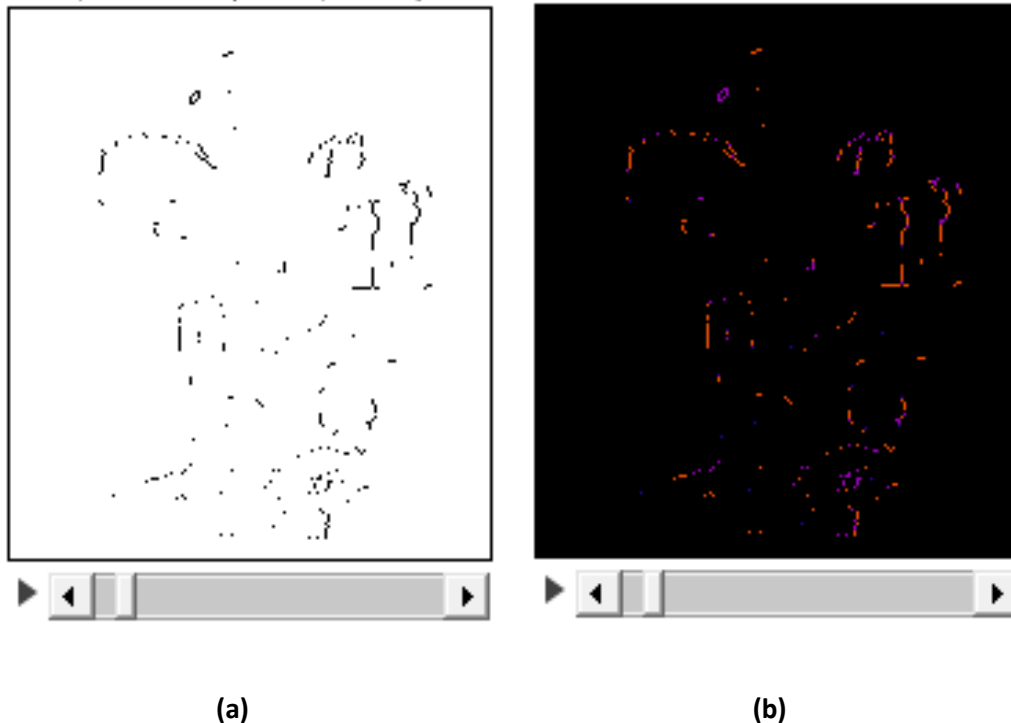


Figure A.1.23. Result of direct skeletonization process from binary image of the inter-connected flow paths with highest degree of connectivity for vibration intensity, $\Gamma=3.0g$ and applied Skeleton3D to obtain (a) thin skeletonized image, which was then analyzed by AnalyzedSkeleton3D to formed (b) pruned thin skeletonized image from which different possible paths/branches from the thin skeleton were estimated.

Appendix B: Statistics Analysis Output and Codes

B. 1.1 SAS output for compaction test

➤ Effect of compaction and cut-section(location) on porosity

Class Level Information		
Class	Levels	Values
Compaction_Depth	7	0 0.2 0.5 1.0 1.5 1.8 2.2
Cuts_section	3	Bottom Middle Top

Number of Observations Read	63
Number of Observations Used	63

Source	DF	Sum of Squares	Mean Square	F Value	Pr > F
Model	8	0.04280317	0.00535040	45.90	<.0001
Error	54	0.00629524	0.00011658		
Corrected Total	62	0.04909841			

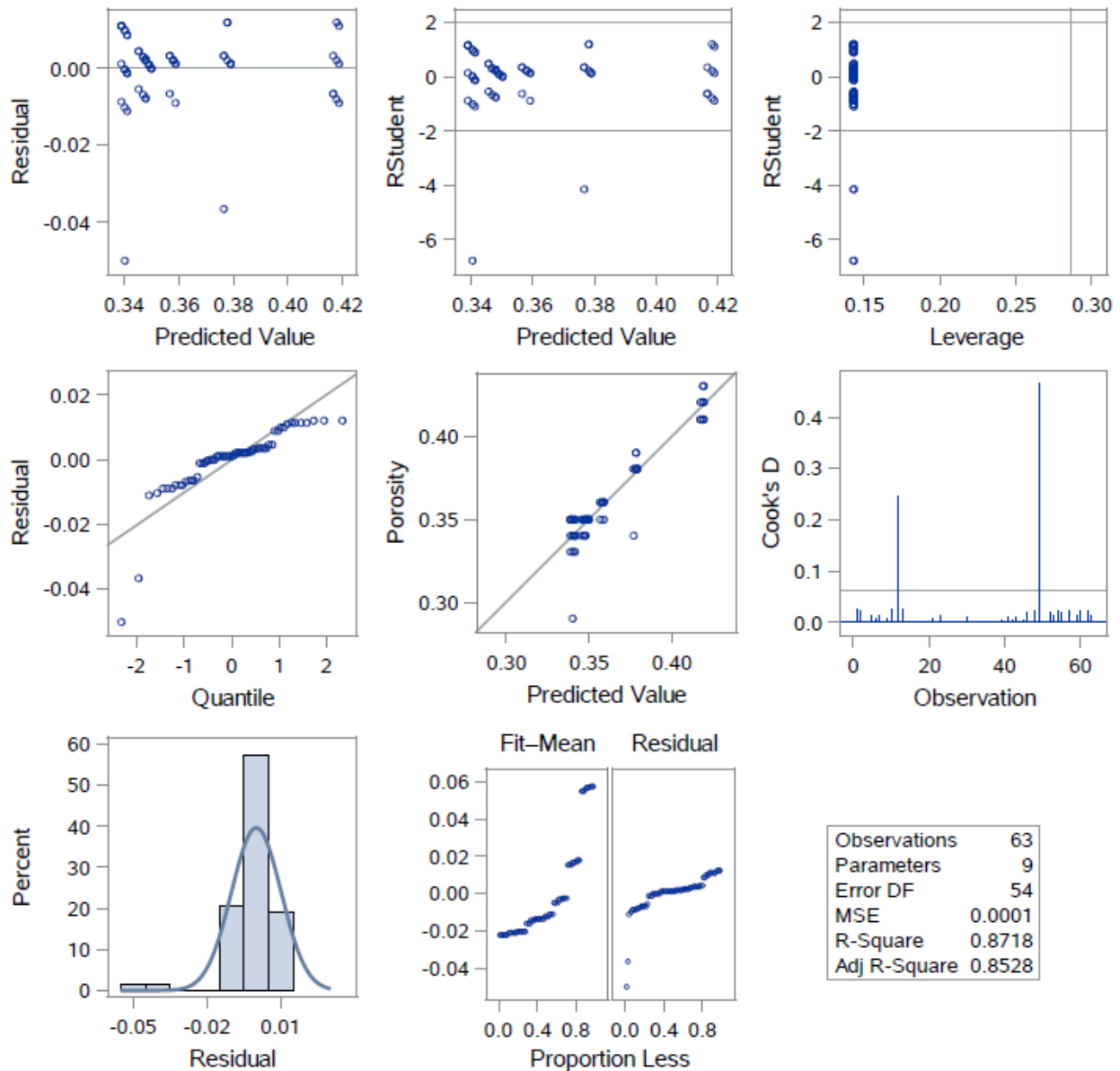
R-Square	Coeff Var	Root MSE	Porosity Mean
0.871783	2.988667	0.010797	0.361270

Source	DF	Type I SS	Mean Square	F Value	Pr > F
Compaction_Depth	6	0.04274286	0.00712381	61.11	<.0001
Cuts_section	2	0.00006032	0.00003016	0.26	0.7730

Source	DF	Type III SS	Mean Square	F Value	Pr > F
Compaction_Depth	6	0.04274286	0.00712381	61.11	<.0001
Cuts_section	2	0.00006032	0.00003016	0.26	0.7730

Dependent Variable: Porosity Porosity

Fit Diagnostics for Porosity

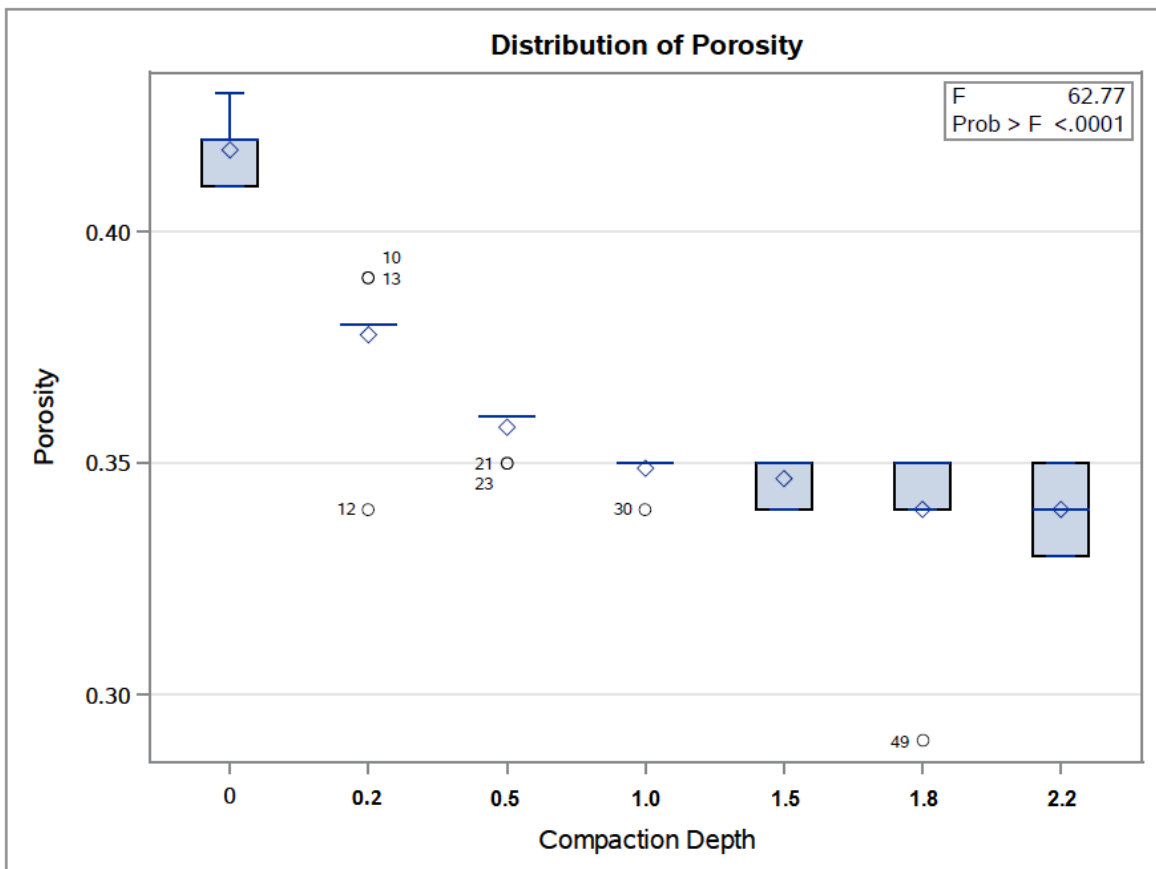


**Least Squares Means
Adjustment for Multiple Comparisons: Tukey**

Compaction_Depth	Porosity LSMEAN	LSMEAN Number
0	0.41777778	1
0.2	0.37777778	2
0.5	0.35777778	3
1.0	0.34888889	4
1.5	0.34666667	5
1.8	0.34000000	6
2.2	0.34000000	7

Least Squares Means for effect Compaction_Depth Pr > t for H0: LSMean(i)=LSMean(j)							
Dependent Variable: Porosity							
i/j	1	2	3	4	5	6	7
1		<.0001	<.0001	<.0001	<.0001	<.0001	<.0001
2	<.0001		0.0043	<.0001	<.0001	<.0001	<.0001
3	<.0001	0.0043		0.5888	0.3216	0.0157	0.0157
4	<.0001	<.0001	0.5888		0.9994	0.5888	0.5888
5	<.0001	<.0001	0.3216	0.9994		0.8444	0.8444
6	<.0001	<.0001	0.0157	0.5888	0.8444		1.0000
7	<.0001	<.0001	0.0157	0.5888	0.8444	1.0000	

Compaction_Depth	Porosity LSMEAN	95% Confidence Limits	
		Lower	Upper
0	0.417778	0.410562	0.424993
0.2	0.377778	0.370562	0.384993
0.5	0.357778	0.350562	0.364993
1.0	0.348889	0.341673	0.356105
1.5	0.346667	0.339451	0.353882
1.8	0.340000	0.332784	0.347216
2.2	0.340000	0.332784	0.347216



**Least Squares Means
Adjustment for Multiple Comparisons: Tukey**

Least Squares Means for Effect Compaction_Depth				
i	j	Difference Between Means	Simultaneous 95% Confidence Limits for LSMean(i)-LSMean(j)	
1	2	0.040000	0.024414	0.055586
1	3	0.060000	0.044414	0.075586
1	4	0.068889	0.053303	0.084475
1	5	0.071111	0.055525	0.086697
1	6	0.077778	0.062192	0.093364
1	7	0.077778	0.062192	0.093364
2	3	0.020000	0.004414	0.035586
2	4	0.028889	0.013303	0.044475
2	5	0.031111	0.015525	0.046697
2	6	0.037778	0.022192	0.053364
2	7	0.037778	0.022192	0.053364
3	4	0.008889	-0.006697	0.024475
3	5	0.011111	-0.004475	0.026697
3	6	0.017778	0.002192	0.033364
3	7	0.017778	0.002192	0.033364
4	5	0.002222	-0.013364	0.017808
4	6	0.008889	-0.006697	0.024475
4	7	0.008889	-0.006697	0.024475
5	6	0.006667	-0.008919	0.022252
5	7	0.006667	-0.008919	0.022252
6	7	0	-0.015586	0.015586

**Least Squares Means
Adjustment for Multiple Comparisons: Tukey**

Cuts_section	Porosity LSMEAN	LSMEAN Number
Bottom	0.36000000	1
Middle	0.36238095	2
Top	0.36142857	3

Least Squares Means for effect Cuts_section Pr > t for H0: LSMean(i)=LSMean(j) Dependent Variable: Porosity			
i/j	1	2	3
1		0.7560	0.9038
2	0.7560		0.9560
3	0.9038	0.9560	

Cuts_section	Porosity LSMEAN	95% Confidence Limits	
Bottom	0.360000	0.355276	0.364724
Middle	0.362381	0.357657	0.367105
Top	0.361429	0.356705	0.366152

Least Squares Means for Effect Cuts_section				
i	j	Difference Between Means	Simultaneous 95% Confidence Limits for LSMean(i)-LSMean(j)	
1	2	-0.002381	-0.010411	0.005649
1	3	-0.001429	-0.009459	0.006602
2	3	0.000952	-0.007078	0.008982

➤ Effect of compaction and cut-section (location) on tortuosity

Class Level Information		
Class	Levels	Values
Compaction_Depth	7	0 0.2 0.5 1.0 1.5 1.8 2.2
Cuts_section	3	Bottom Middle Top

Number of Observations Read	63
Number of Observations Used	63

Dependent Variable: Tortuosity Tortuosity

Source	DF	Sum of Squares	Mean Square	F Value	Pr > F
Model	9	131.9943746	14.6660416	9896.44	<.0001
Error	54	0.0800254	0.0014820		
Uncorrected Total	63	132.0744000			

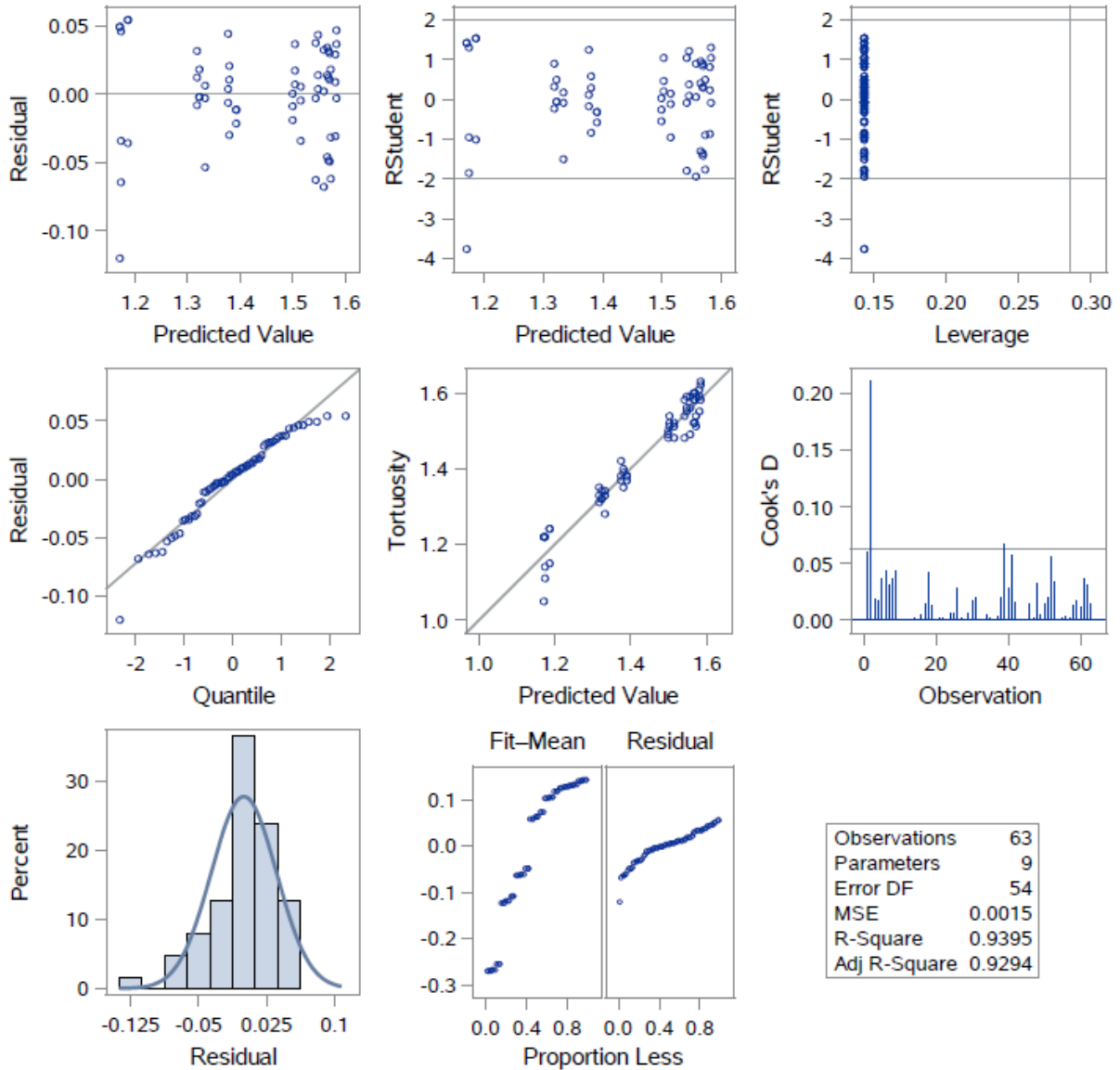
R-Square	Coeff Var	Root MSE	Tortuosity Mean
0.939484	2.672164	0.038496	1.440635

Source	DF	Type I SS	Mean Square	F Value	Pr > F
Comapction_Depth	7	131.9917333	18.8559619	12723.7	<.0001
Cuts_section	2	0.0026413	0.0013206	0.89	0.4161

Source	DF	Type III SS	Mean Square	F Value	Pr > F
Comapction_Depth	6	1.23970794	0.20661799	139.42	<.0001
Cuts_section	2	0.00264127	0.00132063	0.89	0.4161

Dependent Variable: Tortuosity Tortuosity

Fit Diagnostics for Tortuosity



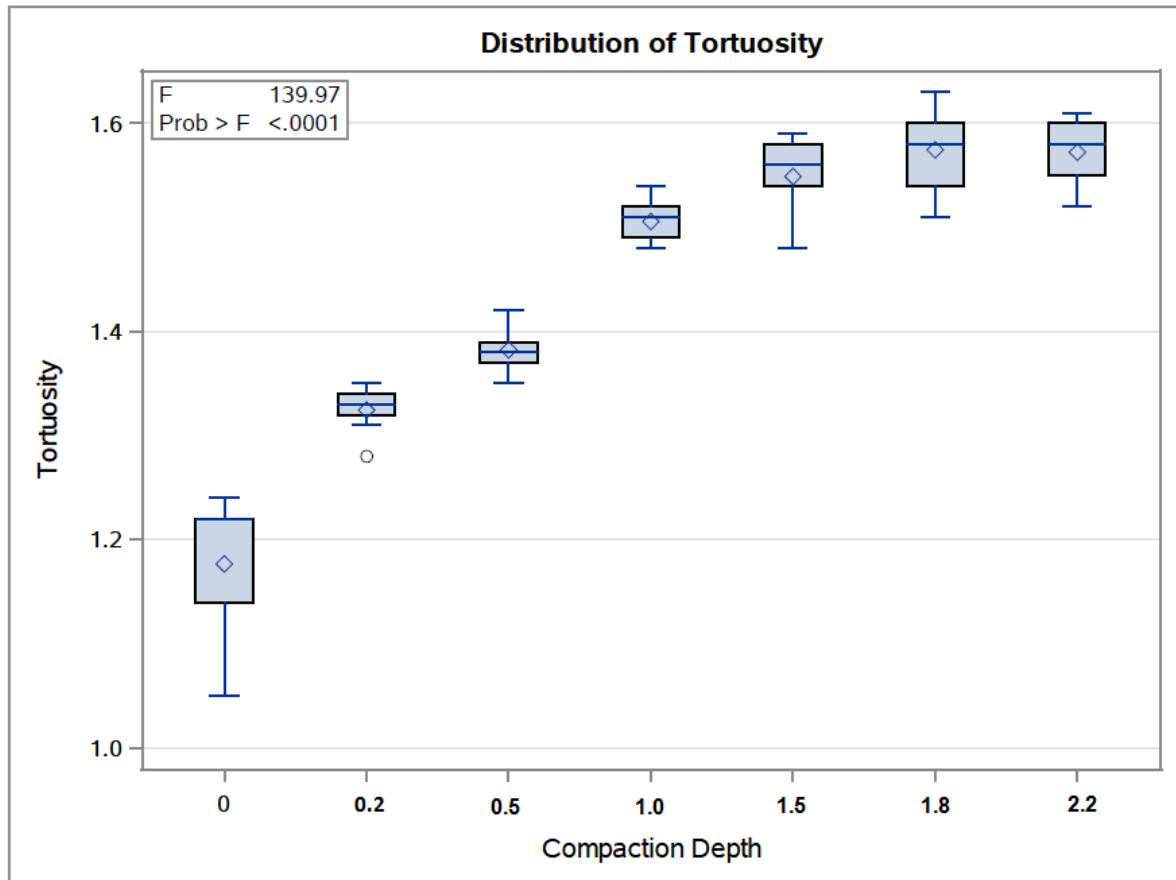
**Least Squares Means
Adjustment for Multiple Comparisons: Tukey**

Comapction_Depth	Tortuosity LSMEAN	LSMEAN Number
0	1.17666667	1
0.2	1.32444444	2
0.5	1.38222222	3
1.0	1.50555556	4
1.5	1.54888889	5
1.8	1.57444444	6
2.2	1.57222222	7

Least Squares Means for effect Comapction_Depth Pr > t for H0: LSMean(i)=LSMean(j) Dependent Variable: Tortuosity							
i/j	1	2	3	4	5	6	7
1		<.0001	<.0001	<.0001	<.0001	<.0001	<.0001
2	<.0001		0.0366	<.0001	<.0001	<.0001	<.0001
3	<.0001	0.0366		<.0001	<.0001	<.0001	<.0001
4	<.0001	<.0001	<.0001		0.2237	0.0065	0.0093
5	<.0001	<.0001	<.0001	0.2237		0.7950	0.8554
6	<.0001	<.0001	<.0001	0.0065	0.7950		1.0000
7	<.0001	<.0001	<.0001	0.0093	0.8554	1.0000	

Comapction_Depth	Tortuosity LSMEAN	95% Confidence Limits	
0	1.176667	1.150940	1.202393
0.2	1.324444	1.298718	1.350171
0.5	1.382222	1.356496	1.407949
1.0	1.505556	1.479829	1.531282
1.5	1.548889	1.523162	1.574616
1.8	1.574444	1.548718	1.600171
2.2	1.572222	1.546496	1.597949

Dependent Variable: Tortuosity Tortuosity



**Least Squares Means
Adjustment for Multiple Comparisons: Tukey**

Least Squares Means for Effect Comapction_Depth				
i	j	Difference Between Means	Simultaneous 95% Confidence Limits for LSMean(i)-LSMean(j)	
1	2	-0.147778	-0.203347	-0.092208
1	3	-0.205556	-0.261125	-0.149986
1	4	-0.328889	-0.384459	-0.273319
1	5	-0.372222	-0.427792	-0.316653
1	6	-0.397778	-0.453347	-0.342208
1	7	-0.395556	-0.451125	-0.339986
2	3	-0.057778	-0.113347	-0.002208
2	4	-0.181111	-0.236681	-0.125541
2	5	-0.224444	-0.280014	-0.168875
2	6	-0.250000	-0.305570	-0.194430
2	7	-0.247778	-0.303347	-0.192208
3	4	-0.123333	-0.178903	-0.067764
3	5	-0.166667	-0.222236	-0.111097
3	6	-0.192222	-0.247792	-0.136653
3	7	-0.190000	-0.245570	-0.134430
4	5	-0.043333	-0.098903	0.012236
4	6	-0.068889	-0.124459	-0.013319
4	7	-0.066667	-0.122236	-0.011097
5	6	-0.025556	-0.081125	0.030014
5	7	-0.023333	-0.078903	0.032236
6	7	0.002222	-0.053347	0.057792

**Least Squares Means
Adjustment for Multiple Comparisons: Tukey**

Cuts_section	Tortuosity LSMEAN	LSMEAN Number
Bottom	1.44952381	1
Middle	1.43428571	2
Top	1.43809524	3

Least Squares Means for effect Cuts_section Pr > t for H0: LSMean(i)=LSMean(j) Dependent Variable: Tortuosity			
i/j	1	2	3
1		0.4110	0.6038
2	0.4110		0.9450
3	0.6038	0.9450	

Cuts_section	Tortuosity LSMEAN	95% Confidence Limits	
Bottom	1.449524	1.432682	1.466366
Middle	1.434286	1.417444	1.451128
Top	1.438095	1.421253	1.454937

Least Squares Means for Effect Cuts_section				
i	j	Difference Between Means	Simultaneous 95% Confidence Limits for LSMean(i)-LSMean(j)	
1	2	0.015238	-0.013392	0.043869
1	3	0.011429	-0.017202	0.040059
2	3	-0.003810	-0.032440	0.024821

➤ Porosity model parameters-SAS output for predicting model parameters

**The NLIN Procedure
Dependent Variable Porosity
Method: Gauss-Newton**

Iterative Phase			
Iter	λ	B	Sum of Squares
0	1.0000	1.0000	4.9846
1	0.0717	0.9150	0.000591
2	0.0718	0.4455	0.000081
3	0.0737	0.3552	0.000042
4	0.0741	0.3544	0.000041
5	0.0742	0.3543	0.000041
6	0.0742	0.3543	0.000041
7	0.0742	0.3543	0.000041

NOTE: Convergence criterion met.

The NLIN Procedure
Dependent Variable Porosity
Method: Gauss-Newton

Iterative Phase			
Iter	X	<i>B</i>	Sum of Squares
0	1.0000	1.0000	4.9846
1	0.0717	0.9150	0.000591
2	0.0718	0.4455	0.000081
3	0.0737	0.3552	0.000042
4	0.0741	0.3544	0.000041
5	0.0742	0.3543	0.000041
6	0.0742	0.3543	0.000041
7	0.0742	0.3543	0.000041

NOTE: Convergence criterion met.

Estimation Summary	
Method	Gauss-Newton
Iterations	7
Subiterations	1
Average Subiterations	0.142857
R	3.208E-6
PPC(b)	6.968E-7
RPC(b)	5.276E-6
Object	6.52E-10
Objective	0.000041
Observations Read	7
Observations Used	7
Observations Missing	0

Note: An intercept was not specified for this model.

Source	DF	Sum of Squares	Mean Square	F Value	Approx Pr > F
Model	2	0.9154	0.4577	55318.6	<.0001
Error	5	0.000041	8.274E-6		
Uncorrected Total	7	0.9155			

The NLIN Procedure

Parameter	Estimate	Approx Std Error	Approximate 95% Confidence Limits	
λ	0.0742	0.00154	0.0702	0.0781
B	0.3543	0.0344	0.2658	0.4427

➤ Tortuosity model parameters-SAS output for predicting model parameters

The NLIN Procedure
Dependent Variable Tortuosity
Method: Gauss-Newton

Iterative Phase			
Iter	a	b	Sum of Squares
0	1.0000	1.0000	6.0375
1	0.9511	0.3638	0.00540

NOTE: Convergence criterion met.

Estimation Summary	
Method	Gauss-Newton
Iterations	1
R	0
PPC	0
RPC(b)	0.636247
Object	0.999105
Objective	0.005402
Observations Read	7
Observations Used	7
Observations Missing	0

Source	DF	Sum of Squares	Mean Square	F Value	Approx Pr > F
Model	1	0.1328	0.1328	122.90	0.0001
Error	5	0.00540	0.00108		
Corrected Total	6	0.1382			

Parameter	Estimate	Approx Std Error	Approximate 95% Confidence Limits	
a	0.9511	0.0454	0.8343	1.0679
b	0.3638	0.0328	0.2794	0.4481

B. 1.2. SAS output for vibration test

- **Effect of vibration intensity and cut-sections (location) on porosity**

Class Level Information		
Class	Levels	Values
Vibration_Intensity	7	0.0 0.5 1.0 1.5 2.0 2.5 3.0
Cuts_section	3	Bottom Middle Top

Number of Observations Read	63
Number of Observations Used	63

Dependent Variable: Porosity Porosity

Source	DF	Sum of Squares	Mean Square	F Value	Pr > F
Model	8	0.06728309	0.00841039	18.31	<.0001
Error	54	0.02480263	0.00045931		
Corrected Total	62	0.09208571			

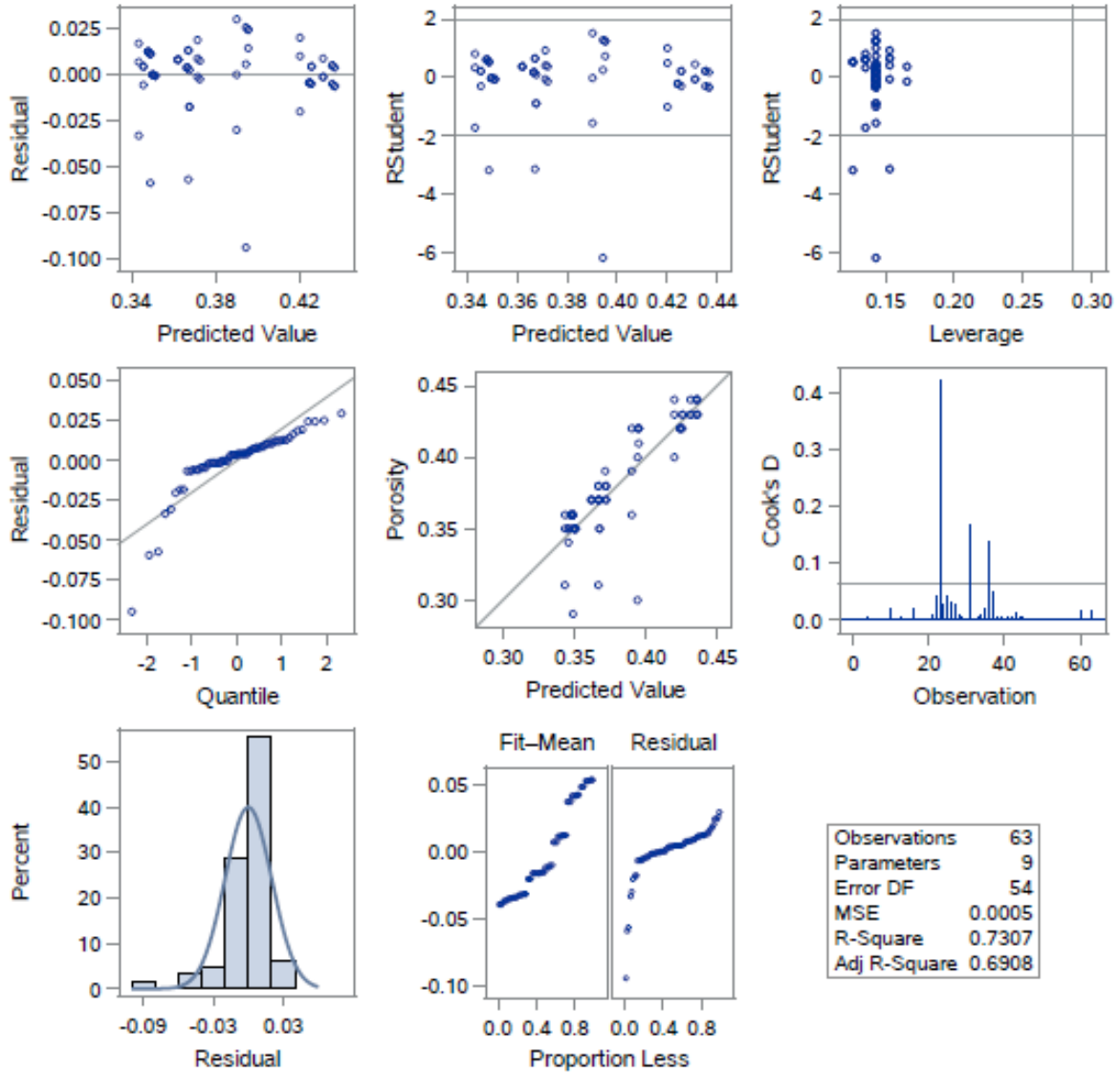
R-Square	Coeff Var	Root MSE	Porosity Mean
0.730657	5.597772	0.021431	0.382857

Source	DF	Type I SS	Mean Square	F Value	Pr > F
Vibration_Intensity	6	0.06694238	0.01115706	24.29	<.0001
Cuts_section	2	0.00034071	0.00017035	0.37	0.6919

Source	DF	Type III SS	Mean Square	F Value	Pr > F
Vibration_Intensity	6	0.06702594	0.01117099	24.32	<.0001
Cuts_section	2	0.00034071	0.00017035	0.37	0.6919

Dependent Variable: Porosity Porosity

Fit Diagnostics for Porosity



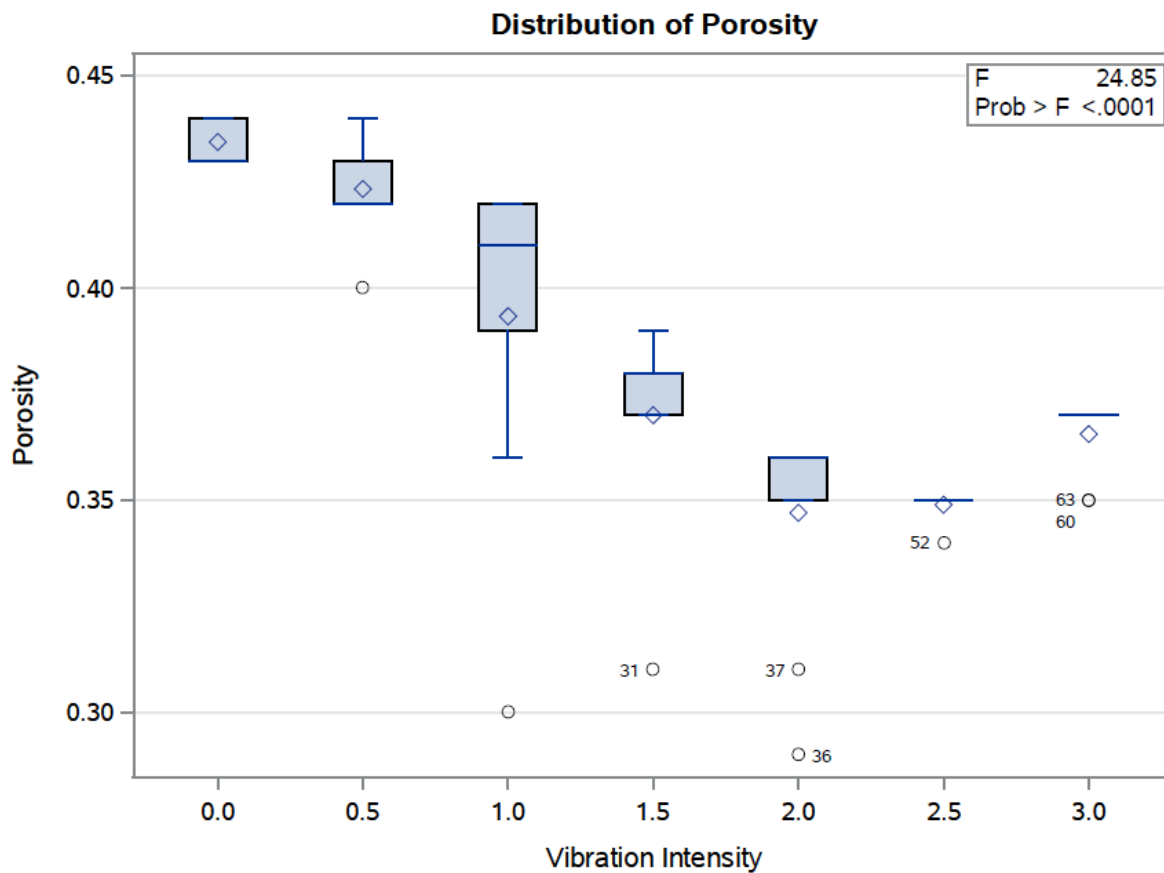
**Least Squares Means
Adjustment for Multiple Comparisons: Tukey-Kramer**

Vibration_Intensity	Porosity LSMEAN	LSMEAN Number
0.0	0.43444444	1
0.5	0.42333333	2
1.0	0.39333333	3
1.5	0.37027178	4
2.0	0.34678257	5
2.5	0.34888889	6
3.0	0.36555556	7

Least Squares Means for effect Vibration_Intensity Pr > t for H0: LSMean(i)=LSMean(j) Dependent Variable: Porosity							
i/j	1	2	3	4	5	6	7
1		0.9255	0.0028	<.0001	<.0001	<.0001	<.0001
2	0.9255		0.0630	<.0001	<.0001	<.0001	<.0001
3	0.0028	0.0630		0.3063	0.0003	0.0010	0.1056
4	<.0001	<.0001	0.3063		0.2618	0.3958	0.9993
5	<.0001	<.0001	0.0003	0.2618		1.0000	0.4860
6	<.0001	<.0001	0.0010	0.3958	1.0000		0.6514
7	<.0001	<.0001	0.1056	0.9993	0.4860	0.6514	

Vibration_Intensity	Porosity LSMEAN	95% Confidence Limits	
0.0	0.434444	0.420122	0.448767
0.5	0.423333	0.409011	0.437656
1.0	0.393333	0.379011	0.407656
1.5	0.370272	0.355050	0.385493
2.0	0.346783	0.333173	0.360392
2.5	0.348889	0.334566	0.363211
3.0	0.365556	0.351233	0.379878

Dependent Variable: Porosity Porosity



**Least Squares Means
Adjustment for Multiple Comparisons: Tukey-Kramer**

Least Squares Means for Effect <i>Vibration_Intensity</i>				
i	j	Difference Between Means	Simultaneous 95% Confidence Limits for LSMean(i)-LSMean(j)	
1	2	0.011111	-0.019825	0.042048
1	3	0.041111	0.010175	0.072048
1	4	0.064173	0.032250	0.096095
1	5	0.087662	0.057486	0.117838
1	6	0.085556	0.054619	0.116492
1	7	0.068889	0.037952	0.099825
2	3	0.030000	-0.000937	0.060937
2	4	0.053062	0.021139	0.084984
2	5	0.076551	0.046375	0.106727
2	6	0.074444	0.043508	0.105381
2	7	0.057778	0.026841	0.088714
3	4	0.023062	-0.008861	0.054984
3	5	0.046551	0.016375	0.076727
3	6	0.044444	0.013508	0.075381
3	7	0.027778	-0.003159	0.058714
4	5	0.023489	-0.007752	0.054730
4	6	0.021383	-0.010540	0.053305
4	7	0.004716	-0.027206	0.036639
5	6	-0.002106	-0.032282	0.028070
5	7	-0.018773	-0.048949	0.011403
6	7	-0.016667	-0.047603	0.014270

**Least Squares Means
Adjustment for Multiple Comparisons: Tukey-Kramer**

Cuts_section	Porosity LSMEAN	LSMEAN Number
Bottom	0.38540425	1
Middle	0.38428571	2
Top	0.38000000	3

Least Squares Means for effect Cuts_section Pr > t for H0: LSMean(i)=LSMean(j) Dependent Variable: Porosity			
i/j	1	2	3
1		0.9844	0.6955
2	0.9844		0.7943
3	0.6955	0.7943	

Cuts_section	Porosity LSMEAN	95% Confidence Limits	
Bottom	0.385404	0.375978	0.394831
Middle	0.384286	0.374909	0.393662
Top	0.380000	0.370624	0.389376

Least Squares Means for Effect Cuts_section				
i	j	Difference Between Means	Simultaneous 95% Confidence Limits for LSMean(i)-LSMean(j)	
1	2	0.001119	-0.014863	0.017101
1	3	0.005404	-0.010578	0.021386
2	3	0.004286	-0.011653	0.020225

➤ Effect of vibration and cut-section (location) on tortuosity

Class Level Information		
Class	Levels	Values
Vibration_Intensity	7	0.0 0.5 1.0 1.5 2.0 2.5 3.0
Cuts_section	3	Bottom Middle Top

Number of Observations Read	63
Number of Observations Used	63

Dependent Variable: Tortuosity Tortuosity

Source	DF	Sum of Squares	Mean Square	F Value	Pr > F
Model	8	1.10249042	0.13781130	145.12	<.0001
Error	54	0.05128101	0.00094965		
Corrected Total	62	1.15377143			

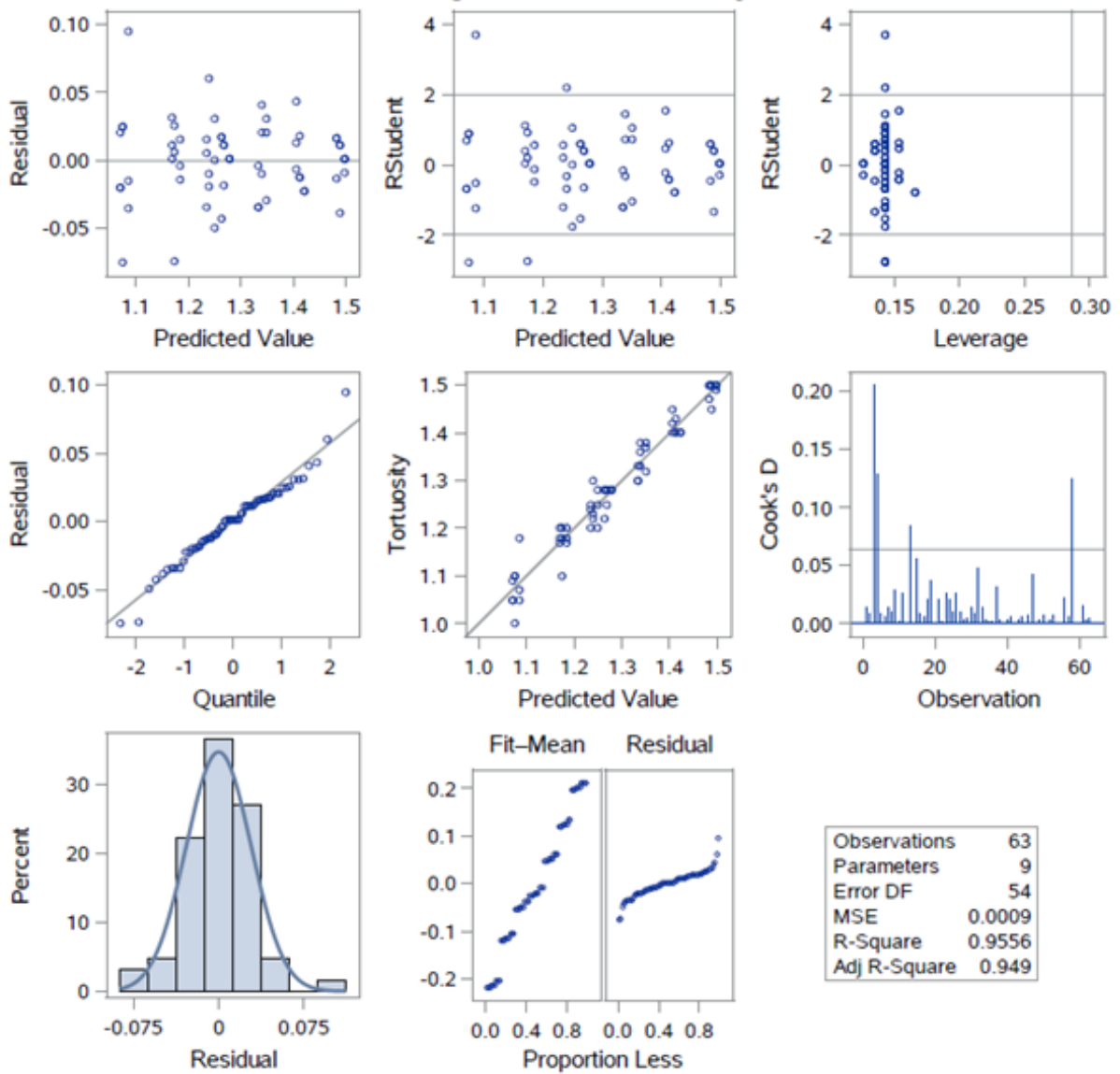
R-Square	Coeff Var	Root MSE	Tortuosity Mean
0.955554	2.392398	0.030816	1.288095

Source	DF	Type I SS	Mean Square	F Value	Pr > F
Vibration_Intensity	6	1.09993143	0.18332190	193.04	<.0001
Cuts_section	2	0.00255899	0.00127950	1.35	0.2685

Source	DF	Type III SS	Mean Square	F Value	Pr > F
Vibration_Intensity	6	1.09842375	0.18307063	192.78	<.0001
Cuts_section	2	0.00255899	0.00127950	1.35	0.2685

Dependent Variable: Tortuosity Tortuosity

Fit Diagnostics for Tortuosity



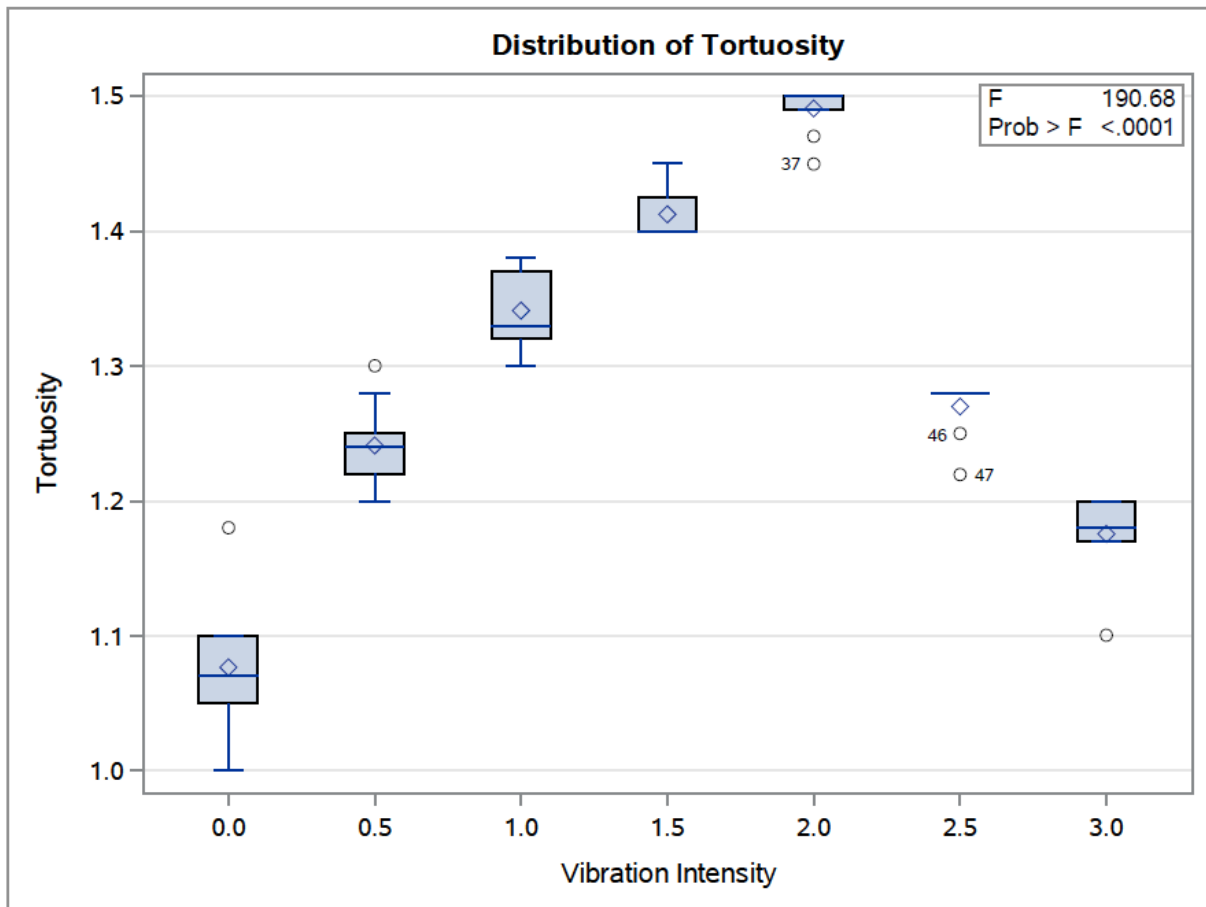
**Least Squares Means
Adjustment for Multiple Comparisons: Tukey-Kramer**

Vibration_Intensity	Tortuosity LSMEAN	LSMEAN Number
0.0	1.07666667	1
0.5	1.24111111	2
1.0	1.34111111	3
1.5	1.41356515	4
2.0	1.49014788	5
2.5	1.27000000	6
3.0	1.17555556	7

Least Squares Means for effect Vibration_Intensity Pr > t for H0: LSMean(i)=LSMean(j) Dependent Variable: Tortuosity							
i/j	1	2	3	4	5	6	7
1		<.0001	<.0001	<.0001	<.0001	<.0001	<.0001
2	<.0001		<.0001	<.0001	<.0001	0.4336	0.0007
3	<.0001	<.0001		0.0002	<.0001	0.0002	<.0001
4	<.0001	<.0001	0.0002		<.0001	<.0001	<.0001
5	<.0001	<.0001	<.0001	<.0001		<.0001	<.0001
6	<.0001	0.4336	0.0002	<.0001	<.0001		<.0001
7	<.0001	0.0007	<.0001	<.0001	<.0001	<.0001	

Vibration_Intensity	Tortuosity LSMEAN	95% Confidence Limits	
0.0	1.076667	1.056072	1.097261
0.5	1.241111	1.220517	1.261705
1.0	1.341111	1.320517	1.361705
1.5	1.413565	1.391678	1.435452
2.0	1.490148	1.470579	1.509717
2.5	1.270000	1.249406	1.290594
3.0	1.175556	1.154961	1.196150

Dependent Variable: Tortuosity Tortuosity



**Least Squares Means
Adjustment for Multiple Comparisons: Tukey-Kramer**

Least Squares Means for Effect Vibration_Intensity				
i	j	Difference Between Means	Simultaneous 95% Confidence Limits for LSMean(i)-LSMean(j)	
1	2	-0.164444	-0.208928	-0.119961
1	3	-0.264444	-0.308928	-0.219961
1	4	-0.336898	-0.382800	-0.290997
1	5	-0.413481	-0.456871	-0.370091
1	6	-0.193333	-0.237817	-0.148850
1	7	-0.098889	-0.143373	-0.054405
2	3	-0.100000	-0.144484	-0.055516
2	4	-0.172454	-0.218355	-0.126553
2	5	-0.249037	-0.292427	-0.205647
2	6	-0.028889	-0.073373	0.015595
2	7	0.065556	0.021072	0.110039
3	4	-0.072454	-0.118355	-0.026553
3	5	-0.149037	-0.192427	-0.105647
3	6	0.071111	0.026627	0.115595
3	7	0.165556	0.121072	0.210039
4	5	-0.076583	-0.121504	-0.031661
4	6	0.143565	0.097664	0.189466
4	7	0.238010	0.192108	0.283911
5	6	0.220148	0.176758	0.263538
5	7	0.314592	0.271202	0.357983
6	7	0.094444	0.049961	0.138928

**Least Squares Means
Adjustment for Multiple Comparisons: Tukey-Kramer**

Cuts_section	Tortuosity LSMEAN	LSMEAN Number
Bottom	1.29540082	1
Middle	1.28000000	2
Top	1.28523810	3

Least Squares Means for effect Cuts_section Pr > t for H0: LSMean(i)=LSMean(j) Dependent Variable: Tortuosity			
i/j	1	2	3
1		0.2481	0.5392
2	0.2481		0.8465
3	0.5392	0.8465	

Cuts_section	Tortuosity LSMEAN	95% Confidence Limits	
Bottom	1.295401	1.281846	1.308956
Middle	1.280000	1.266518	1.293482
Top	1.285238	1.271756	1.298720

Least Squares Means for Effect Cuts_section				
i	j	Difference Between Means	Simultaneous 95% Confidence Limits for LSMean(i)-LSMean(j)	
1	2	0.015401	-0.007580	0.038381
1	3	0.010163	-0.012818	0.033143
2	3	-0.005238	-0.028157	0.017681

➤ Porosity model parameters-SAS output for predicting model parameters

The NLIN Procedure
Dependent Variable Porosity
Method: Gauss-Newton

Iterative Phase			
Iter	<i>A</i>	<i>β</i>	Sum of Squares
0	1.0000	1.0000	2.6772
1	0.0662	0.9780	0.00617
2	0.0674	0.6627	0.00101
3	0.0798	0.6253	0.000410
4	0.0800	0.6312	0.000409
5	0.0800	0.6309	0.000409
6	0.0800	0.6309	0.000409

NOTE: Convergence criterion met.

Estimation Summary	
Method	Gauss-Newton
Iterations	6
R	3.711E-6
PPC(b)	9.112E-7
RPC(b)	0.000021
Object	7.328E-9
Objective	0.000409
Observations Read	7
Observations Used	7
Observations Missing	0

Note: An intercept was not specified for this model.

Source	DF	Sum of Squares	Mean Square	F Value	Approx Pr > F
Model	2	1.0337	0.5168	6311.58	<.0001
Error	5	0.000409	0.000082		
Uncorrected Total	7	1.0341			

Parameter	Estimate	Approx Std Error	Approximate 95% Confidence Limits	
A	0.0800	0.00479	0.0677	0.0923
β	0.6309	0.0693	0.4528	0.8090

➤ Tortuosity model parameters- SAS output for predicting model parameters

**The NLIN Procedure
Dependent Variable Tortuosity
Method: Gauss-Newton**

Iterative Phase				
Iter	<i>a</i>	<i>b</i>	<i>c</i>	Sum of Squares
0	1.0000	1.0000	1.0000	61.8965
1	1.0598	0.4494	0.1381	0.0111

NOTE: Convergence criterion met.

Estimation Summary	
Method	Gauss-Newton
Iterations	1
R	0
PPC	0
RPC(c)	0.861904
Object	0.999821
Objective	0.011067
Observations Read	7
Observations Used	7
Observations Missing	0

Source	DF	Sum of Squares	Mean Square	F Value	Approx Pr > F
Model	2	0.1088	0.0544	19.66	0.0085
Error	4	0.0111	0.00277		
Corrected Total	6	0.1198			

Parameter	Estimate	Approx Std Error	Approximate 95% Confidence Limits	
<i>a</i>	1.0598	0.0459	0.9323	1.1873
<i>b</i>	0.4494	0.0717	0.2504	0.6484
<i>c</i>	0.1381	0.0230	0.0744	0.2018

B.1.3. SAS Codes

➤ **Example of SAS Codes for the 2-way ANOVA and parameters prediction**

```
PROC IMPORT DATAFILE="/folders/myfolders/sasuser.v94/Porosity - Compaction.xlsx"  
            OUT=WORK.MYEXCEL  
            DBMS=XLSX  
            REPLACE;  
  
RUN;  
  
/** Print the results. **/  
  
PROC PRINT DATA=WORK.MYEXCEL; RUN;  
  
proc glm data=WORK.MYEXCEL;  
    class Compaction_Depth Cut_section;  
    model Porosity=Compaction_Depth Cut_section / ss1 ss3;  
    lsmeans Compaction_Depth Cut_section / adjust=tukey pdiff=all alpha=0.05 cl;  
quit;  
  
proc nlin data= WORK.MYEXCEL;  
    parameters a=0.9 B=1;  
    model porosity= 0.42-B(1-EXP(-a*compaction_depth));  
run;
```

Appendix C: UDF Programming codes

C1.1. Mesh process

➤ **Mesh**

Meshes use in this study all consist entirely of tetrahedral elements and were designed to have a very fine mesh near the grain peak, inlet and outlet surfaces to reveal details associated with these locations

➤ **Mesh Independence Study**

Example of fully-perforated floor configuration geometrical model bin:

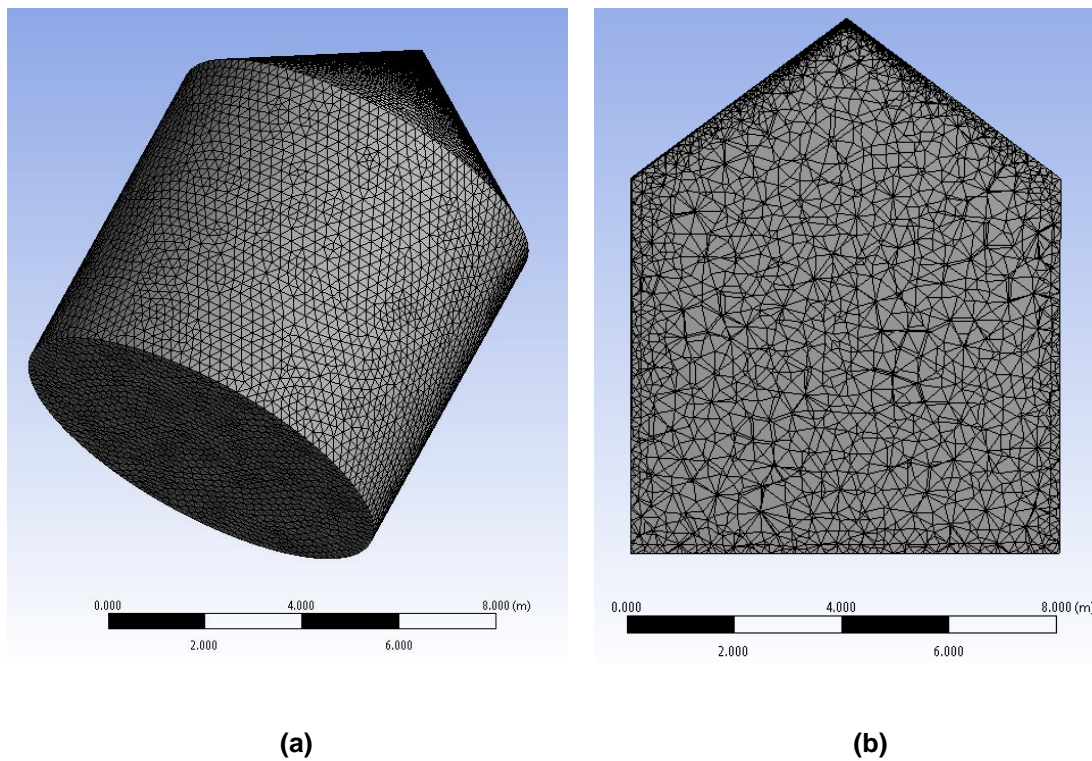


Figure C.1.0. Example of tetrahedral structured mesh for the fully-perforated floor configuration geometrical model showing its (a) 3D schematic and (b) vertical cut-section view.

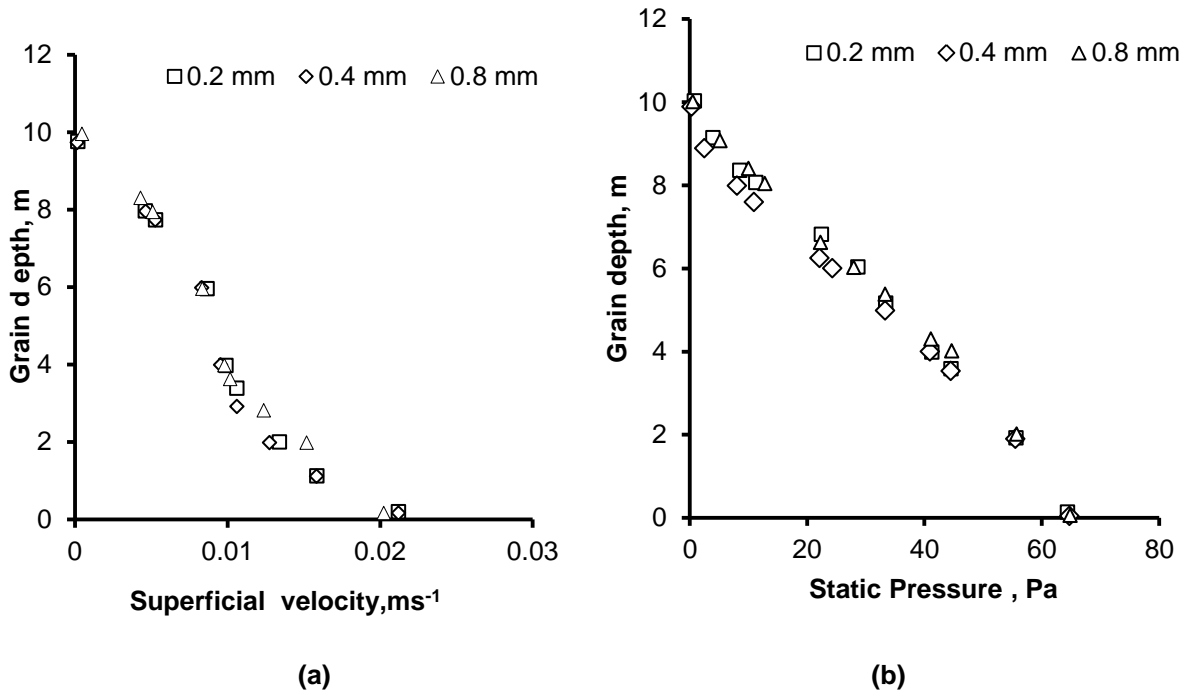


Figure C.1.2. Results of the grid independence studies for fully-perforated floor configuration geometrical model (a) vertical airflow velocity distribution and (b) vertical static pressure distribution.

Example of partially-perforated floor configuration geometrical model bin:

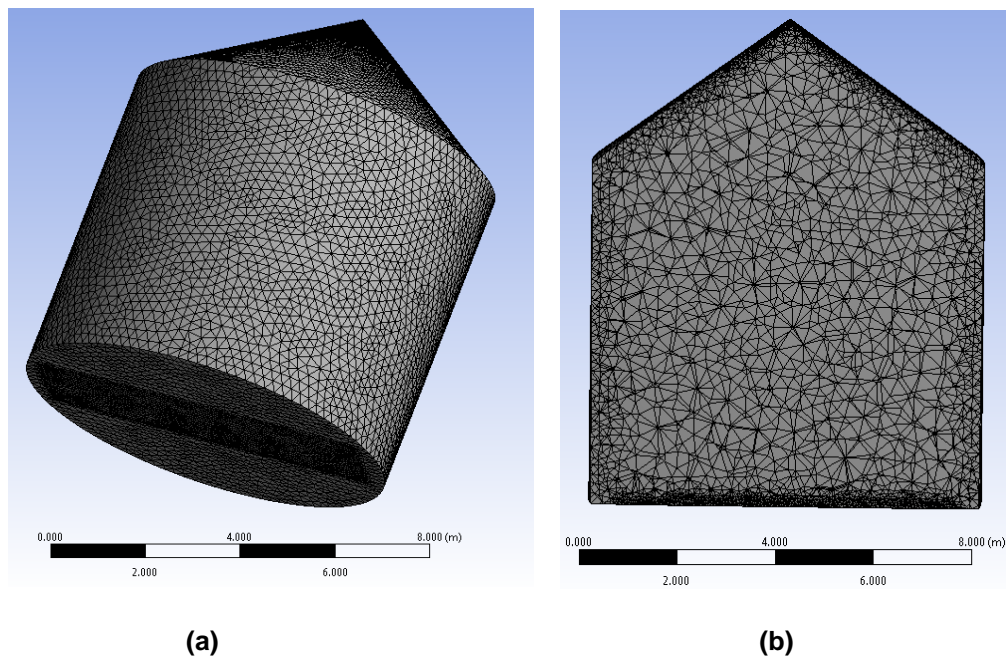


Figure C.1.3. Example of tetrahedral structured mesh for the partially-perforated floor configuration geometrical model showing its (a) 3D schematic and (b) vertical cut-section view.

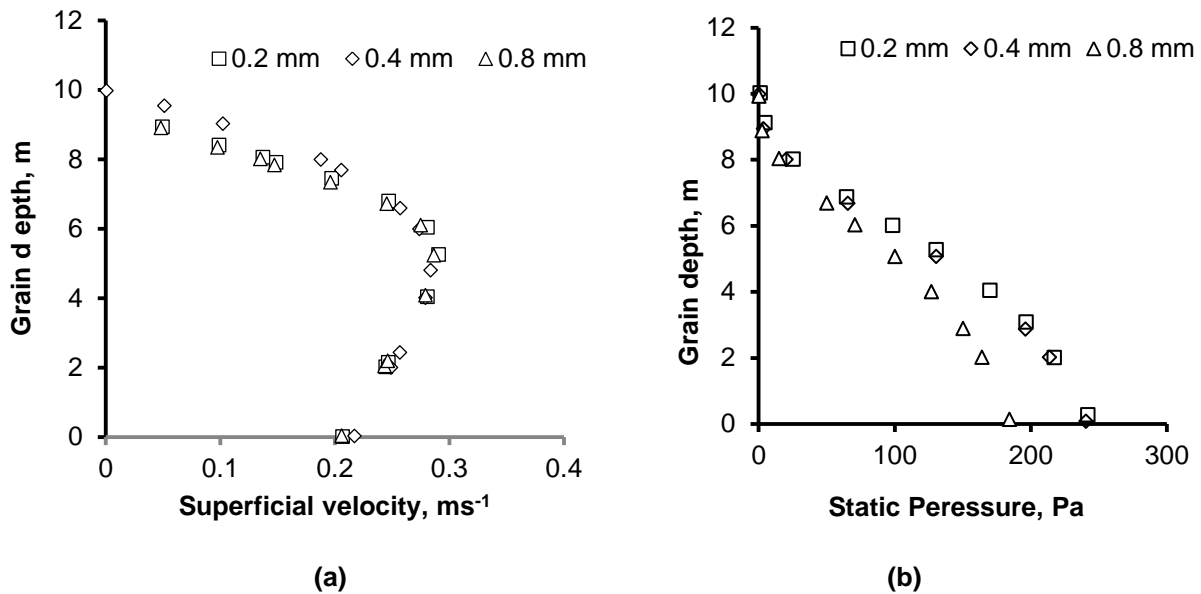


Figure C.1.4. Results of the grid independence studies for partially-perforated floor configuration geometrical model (a) vertical airflow velocity distribution and (b) vertical static pressure distribution.

Example of horizontal airflow configuration geometrical model bin:

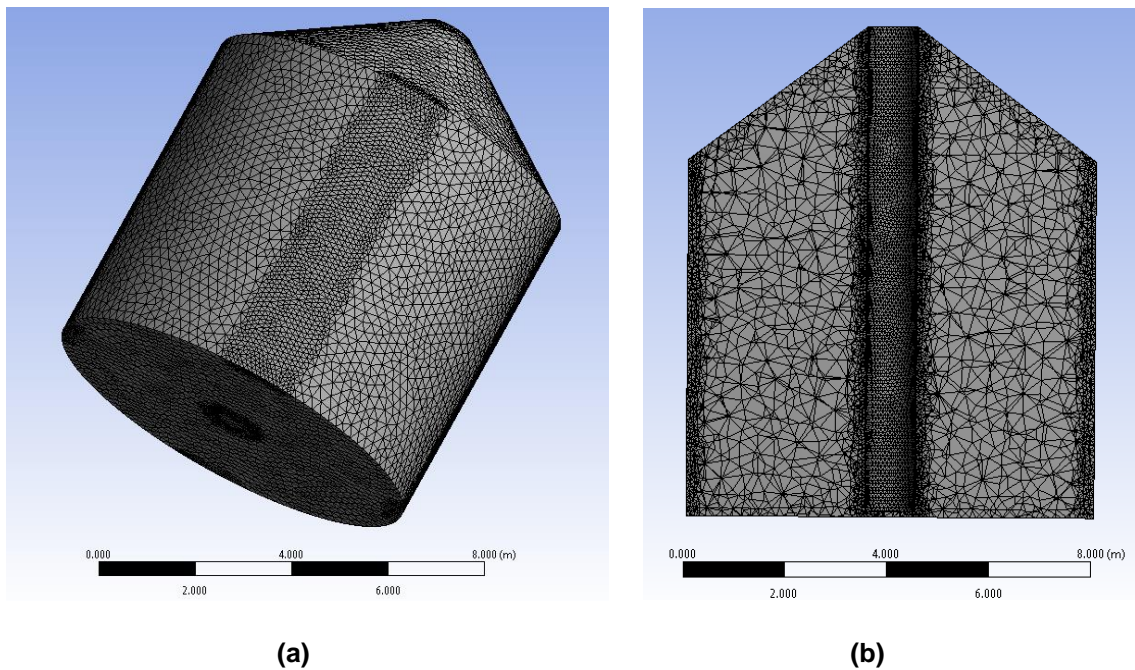
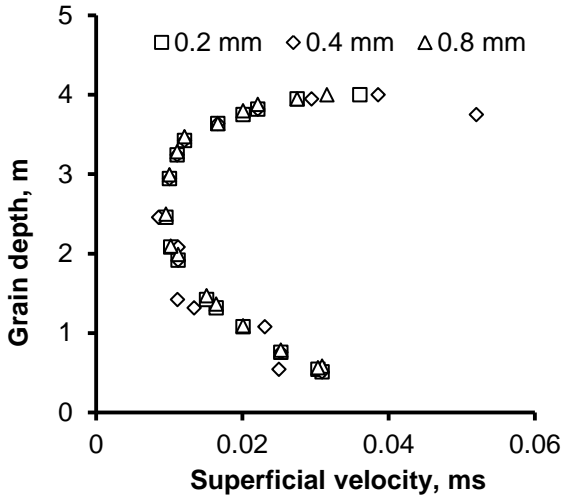
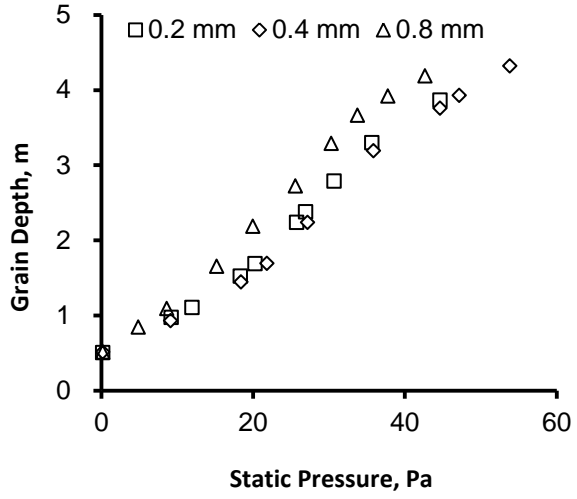


Figure C.1.5. Example of tetrahedral structured mesh for the horizontal-airflow configuration geometrical model showing its (a) 3D schematic and (b) vertical cut-section view.



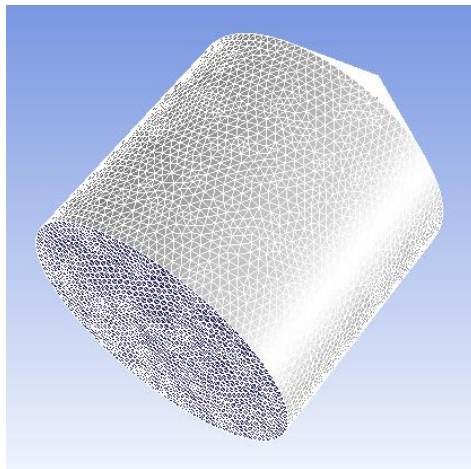
(a)



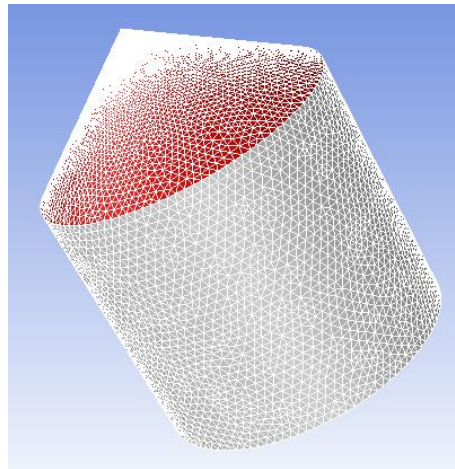
(b)

Figure C.1.6. Results of the grid independence studies for horizontal airflow configuration geometrical model (a) vertical airflow velocity distribution and (b) vertical static pressure distribution.

Example of fully-perforated floor configuration geometrical model boundary locations:



(a)



(b)

Figure C.1.7. Example of boundary location for the fully-perforated floor configuration geometrical model presented with (a) blue colour for inlet location (b) red colour for outlet location.

Example of partially-perforated floor configuration geometrical model bin boundary locations:

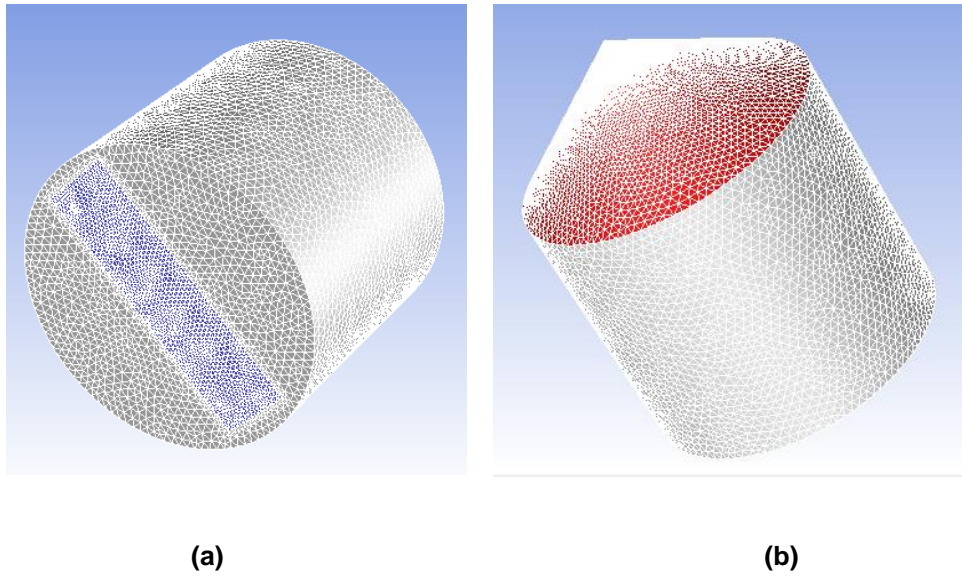


Figure C.1.8. Example of boundary location for the partially-perforated floor configuration geometrical model presented with (a) blue colour for inlet location (b) red colour for outlet location.

Example of horizontal airflow configuration geometrical model boundary locations:

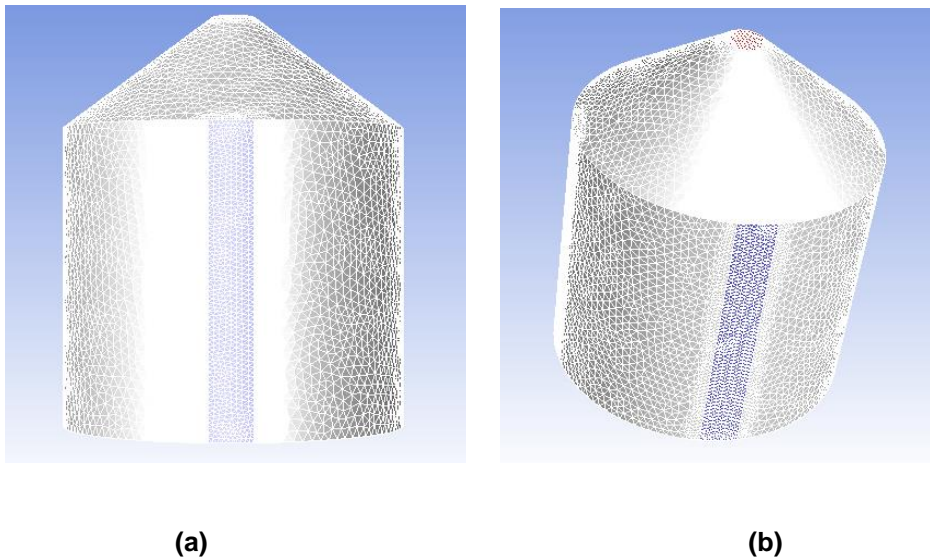


Figure C.1.9. Example of boundary location for the horizontal airflow configuration geometrical model presented with (a) blue colour for inlet location (b) red colour for outlet location.

C1.3. UDF programming codes for variable pore structure characteristics

FLUENT does not have a provision to input spatial-varying porosity and tortuosity required for variable pore structure simulation. A user defined sub routine, shown below, was developed with C programming language to apply the pore structure spatial variation into FLUENT. The user defined functions (UDF) and user defined scalar (UDS) were used to hooked both the porosity and tortuosity variability through the momentum source term and diffusivity UDS respectively.

➤ **UDF for porosity variability as a function of compaction depth**

```
/* ---- These routines implement a porous media model (same as standard
Fluent model) that can vary spatially
by hooking the udf in the source terms
for momentum equations */
#include "udf.h"
* -----
Material Properties
This routine returns the local properties of the material (alpha,C2) for
a given location in the domain (x,y,z).
----- */
void Material_Properties(real x, real y, real z, real *alpha, real *C2)
{
/* --- use this routine to return the variable porosity, alpha and the
co-efficient C2, for each location x,y,z in the domain. */
if MAT_STEP(x,y,z)
{
alpha = 1/(((0.00000017)*pow(0.48-0.32*(1-exp(-0.14*z)),3))/(1-pow(0.48-0.32*(1-exp(-
0.14*z)),2))));
C2 = 700*(1 -(0.48-0.35*(1-exp(-0.07*z))))/(pow(0.48-0.35*(1-exp(-0.07*z)),3));
}
}
```

```

else
{
alpha = 0.0 ;
C2 = 0.0 ;
} }

* -----

X_Momentum_Source

This routine returns the source term for the X-momentum term for each
control volume in the domain. The local properties are obtained by
calling Material_Properties

----- */
DEFINE_SOURCE(SRCE_Xmom,cell,thread,dS,eqn)
{
real x[ND_ND]; /*This will hold the position vectors*/

real alpha, C2, constant1, constant2, Ux, source;

/* --- determine x,y,z co-ordinates of cell */
C_CENTROID(x,cell,thread);

/* --- determine local properties */
Material_Properties(x[0], x[1], x[2], &alpha, &C2);

/* --- determine constants 1,2 */
constant1 = C_MU_L(cell,thread)/alpha;
constant2 = 0.5 * C_R(cell,thread) * C2;

/* --- determine x-velocity */
Ux = C_U(cell,thread);

source = -(constant1*Ux + constant2 * fabs(Ux) * Ux);

dS[eqn] = -(constant1 + 2 * constant2 * fabs(Ux)); /* XXX CHECK */
return source; }

/* -----

Y_Momentum_Source

This routine returns the source term for the Y-momentum term for each
control volume in the domain. The local properties are obtained by

```

calling Material_Properties

```
----- */
DEFINE_SOURCE(SRCE_Ymom, cell, thread, dS, eqn)
{
  real x[ND_ND]; /*This will hold the position vectors*/

  real alpha, C2, constant1, constant2, Uy, source;

  /* --- determine x,y,z co-ordinates of cell */
  C_CENTROID(x,cell,thread);

  /* --- determine local properties */
  Material_Properties(x[0], x[1], x[2], &alpha, &C2);

  /* --- determine constants 1,2 */
  constant1 = C_MU_L(cell,thread)/alpha;
  constant2 = 0.5 * C_R(cell,thread) * C2;

  /* --- determine y-velocity */
  Uy = C_V(cell,thread);

  source = -(constant1*Uy + constant2 * fabs(Uy) * Uy);
  dS[eqn] = -(constant1 + 2 * constant2 * fabs(Uy)); /* XXX CHECK */
  return source; }

```

```
/* -----
Z_Momentum_Source

```

This routine returns the source term for the Z-momentum term for each control volume in the domain. The local properties are obtained by calling Material_Properties

```
----- */
DEFINE_SOURCE(SRCE_Zmom, cell, thread, dS, eqn)
{
  real x[ND_ND]; /*This will hold the position vectors*/

  real alpha, C2, constant1, constant2, Uz, source;

  /* --- determine x,y,z co-ordinates of cell */
  C_CENTROID(x,cell,thread);

  /* --- determine local properties */

```

```

Material_Properties(x[0], x[1], x[2], &alpha, &C2);
/* --- determine constants 1,2 */
constant1 = C_MU_L(cell,thread)/alpha;
constant2 = 0.5 * C_R(cell,thread) * C2;
/* --- determine z-velocity */
Uz = C_W(cell,thread);
source = -(constant1*Uz + constant2 * fabs(Uz) * Uz);
dS[eqn] = -(constant1 + 2 * constant2 * fabs(Uz)); /* XXX CHECK */
return source; }

```

➤ **UDF for the UDS tortuosity variability as a function of compaction depth**

```

#include "udf.h"

DEFINE_PROFILE(porosity_profile,t,i)
{
    real x[ND_ND];
    real z;
    cell_t c;
    begin_c_loop(c,t)
    {
        C_CENTROID(x,c,t);
        z=x[2];
        F_PROFILE(c,t,i)=0.48 - 0.32*(1-exp(-0.14*z));
        C_POR(c,t)=F_PROFILE(c,t,i);
    }
    end_c_loop(c,t)
}

DEFINE_PROFILE(tortuosity_res,t,i)
{
    cell_t c;
    begin_c_loop(c,t)
    {
        F_PROFILE(c,t,i) = 0.95+0.36*log(C_POR(c,t))
        C_UDMI(c,t,0)=F_PROFILE(c,t,i);
    }
    end_c_loop(c,t)
}

DEFINE_DIFFUSIVITY(mean_age_diff,c,t,i)
{
    return C_R(c,t)* C_POR(c,t)/C_UDMI(c,t,0)*2.00x10;
}

```

➤ **UDF for pressure distribution at the inlet of horizontal airflow**

```
#include "udf.h"

DEFINE_PROFILE(pressure_profile,t,i)
{
real x[ND_ND]; /* this will hold the position vector */
real z;
face_t f;
begin_f_loop(f,t)
{
F_CENTROID(x,f,t);
z = x[2];
F_PROFILE(f,t,i) = 254+(z-7)*((0-254)/(0-7));
}
end_f_loop(f,t)
}
```